Capacitive Micromachined Ultrasonic Transducers for Non-destructive Testing Applications

by

Lawrence Lai Pong Wong

A thesis
presented to the University of Waterloo
in fulfillment of the
thesis requirement for the degree of
Doctor of Philosophy
in
Systems Design Engineering

Waterloo, Ontario, Canada, 2014

Author's Declaration

I hereby declare that I am the sole author of this thesis. This is a true copy of the thesis, including any required final revisions, as accepted by my examiners.

I understand that my thesis may be made electronically available to the public.

Abstract

Ultrasound is a popular technique for industrial non-destructive testing (NDT) applications. By sending ultrasonic waves into an object and observing the amplitude and the delay of the reflected or transmitted waves, one can characterize the material, measure the thickness of the object, and detect discontinuities (flaws) as well as the size, location, and orientation of the defects in the object. Traditionally, ultrasonic transducers for NDT are made with piezoelectric crystals. Meanwhile, another class of ultrasonic transducers known as capacitive micromachined ultrasonic transducers (CMUTs) have become popular in medical ultrasound research because of their large bandwidths and other attributes that allow them to be integrated into the tip of a catheter. However, CMUTs have not been widely adopted in ultrasonic NDT applications.

In this thesis, three important CMUTs characteristics that could potentially make them attractive for NDT applications are introduced and demonstrated. First, CMUTs can be beneficial to NDT because the fabrication techniques of CMUTs can easily be used to implement high-frequency, high-density phased arrays, which are essential for high resolution scanning. Surface scanning using a 2-D row-column addressed CMUT array was demonstrated. Secondly, CMUTs can be integrated with supporting microelectronic circuits, thus one can implement a highly integrated transducer system, which can be useful in structural health monitoring NDT applications. Front-end microelectronic circuits that include a transmit pulser and a receive amplifier were designed, tested, and characterized. Thirdly, CMUTs are suitable for air-coupled applications because of their low acoustic impedance at resonance. Air-coupled CMUTs fabricated in a standard RF-MEMS process were characterized and tested.

This thesis concludes with an analysis of the potential usefulness of CMUTs for ultrasonic NDT. While many ultrasonic NDT applications are better off being performed using conventional piezoelectric transducers, CMUTs can and should be used in certain NDT applications that can take advantage of the beneficial characteristics of this exciting transducer technology.

Acknowledgements

I would like to thank all the people who made this thesis possible, and more important, the people who made my experience as a PhD student enjoyable.

First, I would like to thank my supervisor Prof. John T. W. Yeow, for giving me the opportunity to work in his lab, and to work on such an interesting research project. The financial support that John (as I use to call him by his first name) provided was instrumental to my research. During the four-plus years of my study, I have fabricated quite a few designs through CMC, designed countless PCBs, and ordered many components and equipment, and my requests for the purchases were always approved with no question asked. It is a wonderful feeling to know that there is always resource to support my project, and I am grateful for that. I would also like to thank the other members of my committee - Prof. Eihab Abdel-Rahman, Prof. Daniel Stashuk, Prof. Karim Karim, and Prof. Roger Zemp - for being there when I had questions. In addition, I want to thank Prof. Eihab Abdel-Rahman for allowing me to use the vibrometer in his lab. I am also indebted to Prof. Roger Zemp, who agreed to travel from Edmonton to Waterloo to attend my defense in person, given his busy schedule.

Even though PhD study is about doing research individually, life as a PhD student would be so different without lab mates. I would like to thank all the fellow PhD students whom I had the fortune to work with. Special thanks to Andrew Logan who introduced me to the wonderful world of CMUTs, and left behind a bunch of devices for us to play with, and to Albert Chen for being a golf buddy, and more importantly, a good friend, to Shruti Nambiar, Morteza Ahmadi, and Qingshang Kang for the memorable Taiwan trip, and to Zhenghao Li, Shuai Na, Manu Pallapa, and everyone in AMNDL for the help and encouragement.

This work would not be possible without the financial support from the Natural Sciences and Engineering Research Council, the Waterloo Institute for Nanotechnology, CMC Microsystems, and the University of Waterloo. I want to highlight CMC Microsystems for the fabrication services, software licenses, and equipment loan that they provided. Peng Yang of CMC has been especially helpful. He deserves a lot of credit for suggesting me to try the UW-MEMS process when I had trouble getting my PolyMUMPs CMUTs to work.

I also want to thank Alireza Rezvani for his help in wire bonding, and to Sangtak Park and Mahmoud Khater for teaching me how to use the vibrometer.

I want to thank my parents and my sister, Karen, for all the support and encouragement over the past few years. They have been very supportive of my decision to go back to school, and I am thankful for that.

Lastly, and most importantly, I want to thank my lovely wife, Joanne, for being on my side. Joanne went through two pregnancies, and gave birth to Aidan and Kaitlyn, during my PhD study. Thanks for taking care of me, both physically and emotionally, and being patient with me. I would not have been able to make it this far without your support. Thank you!

Table of Contents

List of Tables

List of Figures

Chapter 1

Introduction

1.1 Motivations

Since the introduction of capacitive micromachined ultrasonic transducers (CMUTs) two decades ago [1], CMUT research that includes fabrication [2], modelling [3][4], system integration [5], and applications [6] has garnered a lot of interest from both academia [7] and industry [8]. In particular, using CMUTs for medical imaging applications has been the focus of many research groups [8][9] because several properties of CMUTs, such as large bandwidths and small sizes, make them a much more suitable candidate than conventional piezoelectric transducers for applications that require high performance and highly integrated ultrasonic transducer systems. One example of that is intravascular ultrasound (IVUS) [10], where the transducer has to fit in the tip of a catheter, for ultrasonic imaging of plaques from inside the blood vessels.

On the other hand, while ultrasonic non-destructive testing (NDT) is another application that garners a lot of research interest [11], the use of CMUTs in NDT has not been widely adopted. This is surprising because just like medical imaging, ultrasonic NDT can also benefit from large bandwidth transducers that provide high resolution. For example, inspection of laser weld joints requires the transducers to detect flaws in the sub-mm range [12]. Therefore, the main motivation of this dissertation is to answer the question why

CMUTs have not gained any popularity in ultrasonic NDT. In addition, how can one take advantage of some unique CMUT characteristics for existing and new NDT applications?

The second motivation of this project is to continue the general CMUT research that was started in our lab in 2006. Dr. Andrew Logan, who started the CMUT project as a graduate student, fabricated a number of CMUTs that includes arrays of different shapes, sizes, and configurations [13]. While Dr. Logan's CMUTs and CMUT arrays were intended for medical imaging applications, some of them will likely be useful for NDT and thus worth investigating. Besides, a better understanding of the devices and systems will also benefit CMUT research for medical imaging.

The first item of the Future Work section in Dr. Logan's thesis [13] was the implementation of integrated circuits for CMUT front-end electronics (ASICs). Because highly integrated transducer systems will make CMUTs more attractive for NDT, CMUT front-end electronic circuits that include a pulser and an amplifier were designed and fabricated, with the hope that the development of ASICs will benefit both the NDT and medical imaging projects, and accelerate the CMUT research progress in our lab.

Finally, it is the belief of the author that one of the reasons that make the microelectronics industry so successful is the adoption of a fabless business model. Circuit designers can fabricate their projects through foundries, without going into the cleanroom themselves. If micro-electromechanical systems (MEMS) can follow the same business model, their popularity and the available MEMS applications will grow significantly. Therefore, an attempt was made to fabricate CMUTs with a standard MEMS process, in order to learn the potential of the fabless MEMS approach.

1.2 Contributions and Thesis Outline

The main contribution of this thesis is the development and demonstration of several projects related to CMUT characteristics that are beneficial for NDT. These characteristics include the feasibility of high-density arrays, the possibility of highly integrated systems with electronic circuits, and air-coupled ultrasonic transducers. The secondary contribution is the enhancement of knowledge related to the CMUTs in our lab. Some examples include

the development of an analytical model of the immersion-based CMUTs, identifying the advantages and limitations of row-column addressed arrays, and identifying the design criteria of a transmit pulser.

The thesis is organized as follows. Chapter 2 presents the necessary background information of ultrasonic NDT and CMUTs. Common fabrication methods of CMUTs, as well as the benefits and limitations of CMUTs, are briefly described. Because there is a large body of knowledge related to CMUTs and ultrasound, some of the background materials, such as the basics of phased arrays and CMUT front end circuits, are introduced at the beginning of the respective chapters instead.

In Chapter 3, a 1-D time domain CMUT model that was implemented in Simulink is presented. Chapter 4 re-introduces the row-column addressing scheme. The acoustic modelling of the row-column addressing scheme is presented and the limitations of the row-column addressing scheme are identified. The chapter concludes with a surface scanning experiment that, with a row-column addressed CMUT array, obtains images of a $1mm$ diameter hole on a piece of plastic.

Chapter 5 describes the design, testing, and characterization of front-end circuit elements including a transmit pulser and a receive amplifier. The circuits were fabricated with a high-voltage CMOS process. Experimental results that include generation and detection of ultrasound using CMUTs are presented. The chapter concludes with an characterization experiment of the pulser and an investigation of optimum pulse widths for CMUTs of different resonant frequencies.

In Chapter 6, air-coupled CMUTs fabricated with a multi-user RF-MEMS process are described. Characterization results of the air-coupled CMUTs using a vibrometer and a network analyzer are presented. Experiments showed that the air-coupled CMUTs were able to generate ultrasound in air that was detectable by an off-the-shelf ultrasonic sensor. The chapter concludes with a discussion on the limitations of the air-coupled CMUTs and the corresponding fabrication process.

The final chapter summarizes the results presented in this thesis. An outline of future work that includes the optimization of circuit design and implementation of an improved array addressing scheme is proposed.

Some of the work contained in two of the chapters has been previously published. The paper related to Chapter 4 is

- L. Wong, A. Chen, Z. Li, A. Logan, J. Yeow, "A Row-Column Addressed Micromachined Ultrasonic Transducer Array for Surface Scanning Applications" Ultrasonics, DOI: 10.1016/j.ultras.2014.07.002.

and the publication related to Chapter 5 is

- L. Wong, A. Chen, J. Yeow, "CMUT front-end circuits designed in a high-voltage CMOS process and the phase measurement receiver circuit," 2012 IEEE Ultrasonics Symposium, pp. 1838-1841.

Chapter 2

Background

2.1 Ultrasonic non-destructive testing

Some modern technologies are based on scientific principles that animals, for thousands of years, have been taking advantage of. Ultrasound is a prime example of that. Animals such as bats and dolphins use ultrasound to navigate in the dark or under water. In fact, navigation in the sea, or sonar, was the first ultrasonic application by human beings. As technologies advanced, different ways to use ultrasound were proposed. Nowadays, common ultrasonic applications include range finding, medical imaging, and non-destructive testing.

Ultrasound is defined as sound with frequency greater than the maximum frequency that normal human beings can hear. Frequencies of ultrasound used, depending on the applications, range from 20 kHz (for range finding) to tens of MHz (for medical imaging). In general, higher frequency ultrasonic waves result in higher resolution, but they cannot travel as far. The physics governing audible sound waves also applies to ultrasonic waves. Therefore, in this thesis, ultrasonic waves are sometimes referred to as acoustic waves or simply sound waves.

Non-destructive testing (NDT), also known as non-destructive evaluation (NDE), is a group of techniques to inspect material properties and reveal flaws in objects or structures without damaging the unit under test. Common techniques for NDT include ultrasonic,

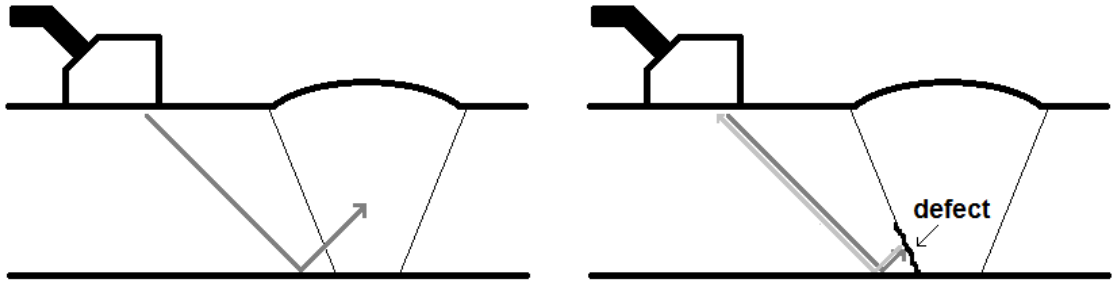

Figure 2.1: Ultrasonic NDT of a weld joint.

magnetic, eddy current and radiographic. Which technique to use depends largely on the type of material, the size of the structure, the type of defect, and the inspection speed. For example, ultrasonic NDT is the most popular technique for weld joint inspection. It is inexpensive and it is the preferred method to inspect materials that cannot be exposed under radiation or electric field. Ultrasonic NDT was first proposed in 1929 by Sokolov to find hidden discontinuities in metal [14].

Ultrasonic NDT systems operate by sending ultrasonic waves into a test object and detecting the reflected waves created by flaws such as cracks or bad solder joints. Figure 2.1 shows how ultrasonic NDT works for weld joint inspections. In this example, ultrasonic waves are sent into the object on an angle. The waves reflect off the bottom boundary before reaching the weld joint. If there is any discontinuity at the joint interface, sound waves will bounce back towards the transducer (right) and a large signal can be detected. But, if the joint is intact, most acoustic energy will go through the interface (left) and the echo that signifies flaws will be absent. This type of ultrasonic inspection is called pulse echo. The advantage of pulse echo inspection is that only one-sided access to the test object is required.

Another ultrasonic inspection technique is through-transmission. Here, the transmission and reception of ultrasonic waves are done with two different transducers. The transmitter and receiver are put on opposite sides of the test object. Through-transmission

is often used for material characterization or thickness measurement when the time-of-flight and signal attenuation are the parameters to be monitored. Moreover, through-transmission also allows the use of continuous waves that can cause an object to vibrate. Vibration occurs when the test piece thickness is a multiple of one half of the sound wavelength, resulting in a standing wave being produced. One example of test object vibration induced by through-transmission is the thickness measurement of aluminum plates [15].

In addition, another ultrasonic NDT technique that is worth mentioning is the use of surface and plate waves. In gas and liquid, sound waves are longitudinal as they propagate by molecule vibration along the direction of the waves. On the other hand, sound waves can be either longitudinal or transverse in solids. When a sound beam enters the test object surface on an angle greater than the critical angle of incidence, surface waves can be generated. Transverse waves that travel along the surface of a solid or along a plate, such as Rayleigh waves or Lamb waves, can travel a longer distance and provide a better test coverage. However, surface waves are not the focus of this thesis.

2.2 Capacitive micromachined ultrasonic transducers (CMUTs)

Traditionally, ultrasonic waves are generated using the piezoelectric principle. Piezoelectric crystals vibrate when an AC voltage is applied to it, and the vibration will in turn produce pressure waves that propagate out at an ultrasonic frequency. Conversely, the reflected ultrasonic waves deform the crystal and cause an AC voltage to be developed across the crystal, thus forming the basis of ultrasound detection. Currently, most commercially available ultrasonic transducers are piezoelectric. However, piezoelectric ultrasonic transducers have their limitations. For example, when transmitting ultrasound into air, piezoelectric transducers are not efficient because of a large acoustic impedance. Moreover, manufacturing piezoelectric transducer arrays is difficult because the process requires a lot of manual labour.

It was the first limitation that prompted researchers to look into a new type of ultrasonic transducers. In order to transmit ultrasonic waves into the air more efficiently, transducers

Figure 2.2: Schematic of a CMUT cell.

with a structure similar to that of condenser microphones were developed by researchers at Stanford University [1]. Condenser microphones detect sound by sensing the change in capacitance of a parallel plate capacitor, thus they can be considered a type of capacitive transducers. However, in order to generate enough power for ultrasonic applications, the electric field inside the capacitive transducer has to be very large, so large that the air inside the capacitor will break down and start conducting electricity . Fortunately, when the gap between the two plates reduces to a microscopic level, the electric field that the gap can withstand increases significantly [16]. To fabricate such a thin gap, researchers used micromachining techniques to fabricate capacitive transducers with gap height in the micrometer or sub-micron range. They called the new devices capacitive micromachined ultrasonic transducers (CMUTs) [17].

Figure 2.2 shows the basic structure of a CMUT. A CMUT consists of a pair of (top and bottom) electrodes. The bottom electrode is typically not movable and situated on top of a substrate. The top electrode, on the other hand, sits on top of a movable membrane. In some cases when the membrane is electrically conductive, the membrane can also act as the top electrode. The two electrodes are separated by a gap, or cavity, of air or vacuum, allowing room for the membrane to vibrate. In normal operation, a bias voltage, of typically several tens of volts, is applied across the electrodes. The developed electrostatic force pulls the top electrode down and reduces the gap height.

To generate ultrasound, a voltage pulse is applied across the biased device. The pulse causes the top electrode to vibrate at the resonant frequency of the structure, resulting in acoustic waves. The same CMUT can also be used to detect ultrasonic waves. Incoming sound waves cause the top electrode to move, producing a change in capacitance between the electrodes. With the bias voltage fixed, a current corresponding to the incoming acoustic pressure can then be measured. An ultrasonic transducer consists of many CMUT

cells connected in parallel in order to generate enough power. In addition, for imaging applications, an array of transducer elements is typically required. Ultrasonic transducer arrays are discussed in detail in Chapter 4.

The CMUT bias voltage is needed because of two reasons. Firstly, a bias voltage increases the output acoustic power and the receive sensitivity of a CMUT because of the spring softening effect: when the top electrode deflects down because of a electrostatic force, it becomes more sensitive to any additional forces, either electrostatic or external force due to pressure. Secondly, as the electrostatic force is proportional to the square of the input voltage, adding a DC bias will help to linearize the AC voltage:

$$F_e \propto V^2 = (V_{DC} + V_{ac})^2 = {V_{DC}}^2 + 2V_{DC}V_{ac} + {V_{ac}}^2 \tag{2.1}$$

If the DC bias voltage is significantly larger than the AC voltage, the electrostatic force will vary with the AC input voltage linearly.

2.2.1 Fabrication

Early CMUTs were fabricated using surface micromachining techniques [1][17]. Each layer, from bottom to top, is deposited on the silicon wafer sequentially. A simple surface micromachining process is illustrated in Figure 2.3. The process starts with a substrate. After the sacrificial layer deposition, anchor holes are etched on the sacrificial layer to allow the structural layer access to the substrate. Next, the structural layer is deposited on top of the sacrificial layer. Finally, the sacrificial layer is removed, or the structure is released as it is now free to move.

For CMUTs fabrication, the bottom electrode is first deposited, followed by a sacrificial layer, a dielectric layer for the membrane, and finally the top electrode. The cavity between the two electrodes is then created by etching away the sacrificial layer. However, if a sealed cavity is required, an additional step is required to seal the etch holes, because they must be present to allow the etchant access to the sacrificial layer.

Since the report of the first CMUT, various CMUT fabrication techniques were proposed. Huang et. al. [18] were the first to demonstrate wafer bonded CMUTs. A sample

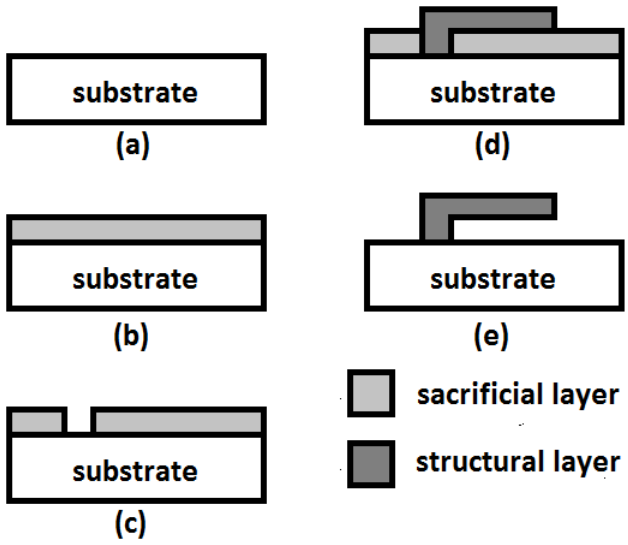

Figure 2.3: Fabrication steps of a surface micromachining process: (a) start with a substrate, (b) deposit sacrificial layer, (c) etch anchor holes on sacrificial layer, (d) deposit structural, and (e) remove the sacrificial layer.

wafer bonding process is illustrated in Figure 2.4. A wafer bonding process involves two silicon wafers, one for the top electrode and one for the bottom electrode (Figure 2.4(a)). The two wafers undergo photolithography steps separately (Figure 2.4(b)), before combining, or bonding, to form the device, as shown in Figure 2.4(c). After that, the substrate of the top wafer is removed (Figure 2.4(d)).

For CMUTs, the bonding is typically done in a vacuum to avoid squeeze film damping [19] that will affect the membrane vibration. Wafer bonded CMUT design is more flexible because the area and the depth of the cavities are not limited by processing steps of other layers. Silicon-on-insulator (SOI) wafers were required in [18], but the use of normal, and cheaper, silicon wafers were demonstrated by Logan and Yeow [20]. Other ways to fabricate CMUTs include post-processing of a standard integrated circuit CMOS process [21] and a low temperature fabrication method that allows CMUTs to be fabricated on the same wafer as electronic circuits [22]. Finally, the use of commercially available multi-user MEMS processes, such as PolyMUMPs, was also explored [23][24].

2.2.2 Advantages and Limitations

As mentioned in the beginning of this section, CMUTs, compared with conventional piezoelectric transducers, are more efficient for air-coupled ultrasound applications. But when CMUTs are operated in immersion, they have another advantage, which is a larger bandwidth that can lead to an improved scanning resolution. Because CMUT membranes are very thin, any vibration is damped heavily by the medium. As a result, short pulses are produced. A shorter pulse in the time domain corresponds to a larger bandwidth in the frequency domain, leading to a better scanning resolution. Another way to understand the benefit of a short pulse is by recognizing the fact that when measuring distance using a pulse echo setup, a longer pulse will introduce more uncertainty, thus shorter pulses are preferred.

Another advantage of CMUTs stems from the fact that they are made using similar technologies as that of integrated circuits. As a result, integration of CMUTs with microelectronic circuits is straightforward. Microelectronic circuits are implemented as application specific integrated circuits (ASICs) and they need to be situated close to the

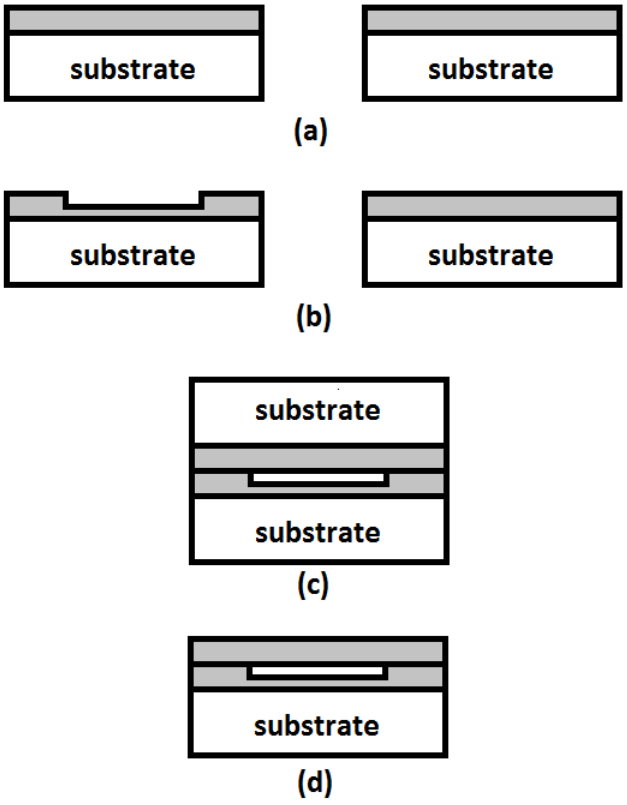

Figure 2.4: Fabrication steps of a wafer bonding process: (a) start with two substrates and deposit dielectric layers on top, (b) etch the cavity on one of the wafers, (c) bond the two wafers, (d) remove the substrate from the top wafer.

CMUTs to avoid any unnecessary parasitic capacitance and resistance, which affect the device performance. As mentioned in the previous sub-section, researchers have demonstrated fabrication of CMUTs and electronic circuits on the same silicon wafer [22]. Other integration methods include flip chip bonding of the CMUTs on top of the ASICs [5] and connecting the CMUTs and the ASICs with flexible printed circuit boards (PCBs) [10]. It will be difficult to connect piezoelectric transducers to the ASICs using these methods.

Finally, CMUT fabrication processes allow the manufacturing of high frequency and high density ultrasonic arrays, which improve the device flexibility and the resulting image resolution. All these advantages are considered in this thesis to look into the feasibility of CMUTs for non-destructive testing applications.

This promising technology also has its limitations. For one, CMUT membranes cannot make contact with solids, thus generating ultrasonic waves in a solid must be done through a medium. Other limitations of CMUTs include dielectric charging [25] and acoustic crosstalk [26]. Dielectric charging refers to the trapping of charges within the dielectric layer of a CMUT, affecting the consistency and reliability of the device. Acoustic crosstalk means the coupling of energy to neighbouring CMUT elements when a CMUT element is transmitting, causing unwanted signals to be generated. Fortunately, researchers have spent significant effort on understanding these two effects, and have come up with solutions to mitigate the problems [27][26].

2.2.3 Modes of Operation

The normal operation of CMUTs requires a bias voltage to deflect the membrane slightly. Ultrasound generation is then achieved by applying voltage pulses to the CMUT, causing the membrane to vibrate. Throughout the entire operation, the CMUT membrane never touches the bottom of the cavity. On the other hand, there is another CMUT mode of operation called the collapse mode [28]. To get into collapse mode, the bias voltage is first increased beyond the pull-in voltage, causing the membrane to collapse. Then, the bias voltage is slightly reduced but is still high enough to keep the membrane in the collapsed position. From that point on, transmission and reception of ultrasound work exactly the

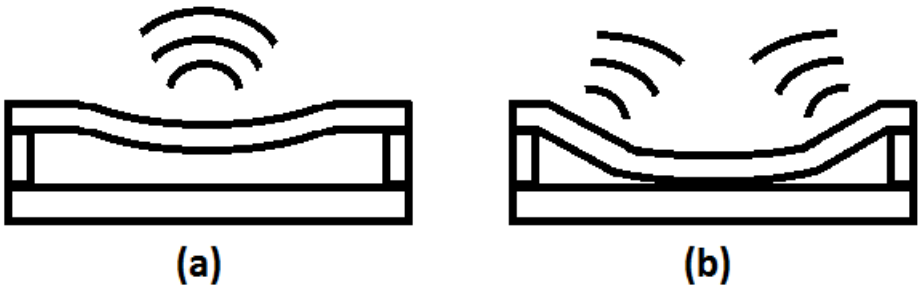

Figure 2.5: Different operating modes of a CMUT: (a) conventional mode, (b) collapse mode.

same as the normal, or conventional mode. The conventional mode and the collapse mode of CMUT are illustrated in Figure 2.5.

During collapse mode, the membrane is always in contact with the bottom of the cavity. The ultrasound, then, is generated by the vibration of membrane areas that are not in contact with the cavity bottom, typically along the circumference of the membrane. Because the capacitance against voltage curve has a steeper slope at the region of collapse, collapse mode CMUTs are more efficient: they generate a higher pressure and have a higher sensitivity. However collapse mode CMUTs are more susceptible to dielectric charging effect because the top electrode is always in contact with the dielectric layer.

Although certain theories or ideas described in this thesis can be applied to collapse mode CMUTs, the focus of this work is still on normal, or conventional mode, CMUTs.

2.2.4 Applications

The first application of CMUTs was air-coupled NDT because of their high efficiency in coupling ultrasound in air. However, it did not take long for the researchers at Stanford University to realize that CMUTs offer superior bandwidth, compared to conventional piezoelectric transducers, when operating in immersion. Added to the fact that CMUT fabrication technologies allow small transducers and highly integrated systems to be made,

it became clear that CMUTs offer the most benefits in medical imaging applications. In particular, putting CMUTs in the tip of a catheter for *in vivo* imaging, also known as Intravascular Ultrasound (IVUS), has become the main research goal of several groups [10][29]. In both systems ([10] and [29]), the CMUT arrays and the front end electronic circuits are located at the tip of the catheter. The arrays are in a ring, or an annular, configuration, providing a lumen in the centre of the catheter tip that allows other applications such as ablation and the use of other imaging modalities.

CMUTs can also be used to generate high-intensity focused ultrasound (HIFU) for cancer treatments [30][31], to mix fluids in micro-fluidic channels for lab-on-a-chip applications [32], and as sensors for fluid properties [33] and chemicals [34].

At the time of writing, the first commercialized CMUT device is already in production [35]. While [35] is an external probe for ultrasonic mammography and is not for IVUS, the device shows that the CMUT technology has matured enough to be used in real life applications.

Chapter 3

CMUT Modelling

3.1 A 1-D CMUT Model

The most basic performance parameter of a ultrasonic transducer is its output pressure. A higher output pressure is desirable because the emitted sound can travel further, and the signal-to-noise ratio (SNR) of the received waveforms will be higher. Calculating the output pressure that results from a voltage input requires the consideration of three domains: electrical, mechanical, and acoustic. Fortunately, a couple of assumptions can simplify the calculation substantially. If the dimensions of the vibrating membrane are smaller than the radiated wavelength, which should be true for most CMUTs, the generated pressure amplitude will depend mainly on the volume velocity, or the rate of change of air/fluid volume that the membrane displaces when vibrating [36]. In addition, if the pressure is measured directly in front of and far away from the transducer, diffraction of sound and the directivity of the transducer can be ignored, and the transducer can be considered as a point source. In that case, the measured pressure will be directly related to the membrane velocity. Therefore, a 1-D model of membrane displacement can be used to predict the output power of a CMUT.

The CMUT being modelled is based on the devices that were fabricated by our lab. These CMUTs were fabricated with a micromachining process that involves fusion bonding

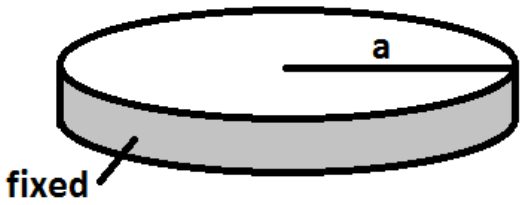

Figure 3.1: The basic shape of a circular CMUT membrane.

in a vacuum and uses silicon nitride as the dielectric membrane and insulation layers. The fabrication process of these CMUTs was described in [20] and [13]. Each CMUT cell has a circular membrane, as illustrated in Figure 3.1. The circumference of the membrane is fixed, while the centre is free to vibrate. The membrane vibrating motion can be greatly simplified by modelling a piston-like motion. In other words, every point on the entire membrane is assumed to have the same displacement.

On the other hand, assuming that the piston has the same area as the membrane will lead to inaccurate results because the CMUT membrane is clamped and the volume displacements in the two cases are quite different. Therefore, an adjustment factor must be applied to the piston area. Making the two cases comparable requires both structures to displace the same volume under the same condition. First, we use a shape function based on basic plate theory that was purposed in [37] to describe the membrane deflection:

$$w(r) = w_{pk}(1 - \frac{r^2}{a^2})^2 \tag{3.1}$$

where w_{pk} is the peak deflection at the centre of the membrane, and a is the radius of the membrane. The same paper also proved that when pull-in occurs, the peak deflection equals 46% of the gap height, assuming that the deflection is small compared to the membrane thickness [37]. Therefore, just before pull-in occurs, the volume displaced by the membrane is

$$\int_0^a 2\pi r w_{pk}(1 - \frac{r^2}{a^2})^2 dr = \frac{w_{pk}}{3}\pi a^2 = \frac{0.46d}{3}\pi a^2 \tag{3.2}$$

where d is the un-deflected gap height between the two electrodes.

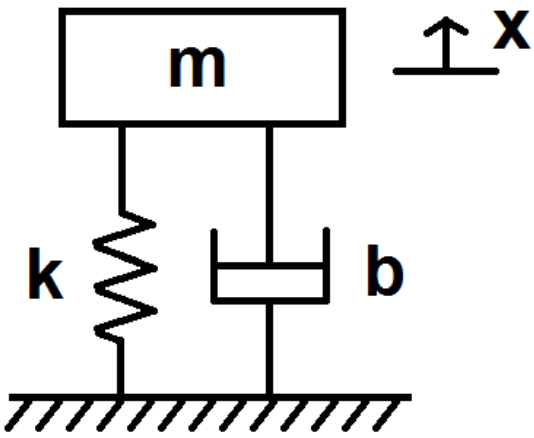

Figure 3.2: A mass-spring-damper system.

For a piston, pull-in occurs when the deflection is one third of the gap height, and the volume displaced is $Sd/3$ where S is the area of the piston. Equating that with (3.2), we obtain

$$\begin{aligned} S &= 0.46\pi a^2 \\ a_{eff} &= 0.68a \end{aligned} \tag{3.3}$$

where a_{eff} is the effective radius or the radius of the piston in the model. Thus a membrane of radius a, with a maximum deflection w_{pk}, can be modelled as a piston of radius $0.68a$ that has the same volume displacement right before pull-in.

A piston vibrating motion can be modelled as lumped elements consisting of a mass, a spring, and a damper [38], as shown in Figure 3.2. Assuming no external load, the equation of motion can be written as

$$m\frac{d^2x}{dt^2} + b\frac{dx}{dt} + kx + f_e = 0 \tag{3.4}$$

Where x is the displacement of the piston (negative x means movement towards the bottom electrode), m is the equivalent mass of the piston, b is the damping coefficient, k is the spring constant, and f_e is the electrostatic force acting on the piston. The symbol b is

used for the damping coefficient instead of the conventional c to avoid confusion with capacitance and the speed of sound.

The electrodes form a parallel plate capacitor, which stores an electric energy

$$W = \frac{CV^2}{2} = \frac{\varepsilon S V^2}{2(d+x)} \tag{3.5}$$

Where ε is the permittivity of the medium between the two electrodes, V is the voltage across the capacitor or the input voltage of the CMUT. The electrostatic force can then be written as

$$f_e = -\frac{dW}{dx} = \frac{\varepsilon S V^2}{2(d+x)^2} \tag{3.6}$$

From equations (3.4) and (3.6), a model can be constructed to convert the input voltage into the displacement of the CMUT membrane. A transient model, implemented in Simulink (The MathWorks Inc., Natick, MA), is shown in Figure 3.3. A similar model was reported in [39], but the parameters of this model are devised differently. The model is included in this thesis to provide insights into the operation of CMUTs fabricated in our lab.

The input of the model is the CMUT input voltage. It is summed with the CMUT bias voltage before feeding into the section that implements equation (3.6). The feedback loop with the two integrators models the differential equation (3.4), and the outputs of the two integrators represent the velocity and the displacement of the membrane.

In order to use the model, the parameters k, b, and m must be first determined. Because the CMUT has already been characterized [13], the measured collapse voltage and resonant frequency are used to calculate the required modelling parameters. If these measurable results are not known, they will need to be calculated numerically, for example, by finite element method (FEM) modelling. In addition, more information of the fabrication process, for example the material properties and the membrane residual stress, will need to be considered. In this chapter, both the collapse voltage and the resonant frequency are assumed to be available for this 1-D model.

Substituting (3.6) into (3.4), and considering only the steady state, (3.4) can be reduced to

$$kx + \frac{\varepsilon S V^2}{2(d+x)^2} = 0 \tag{3.7}$$

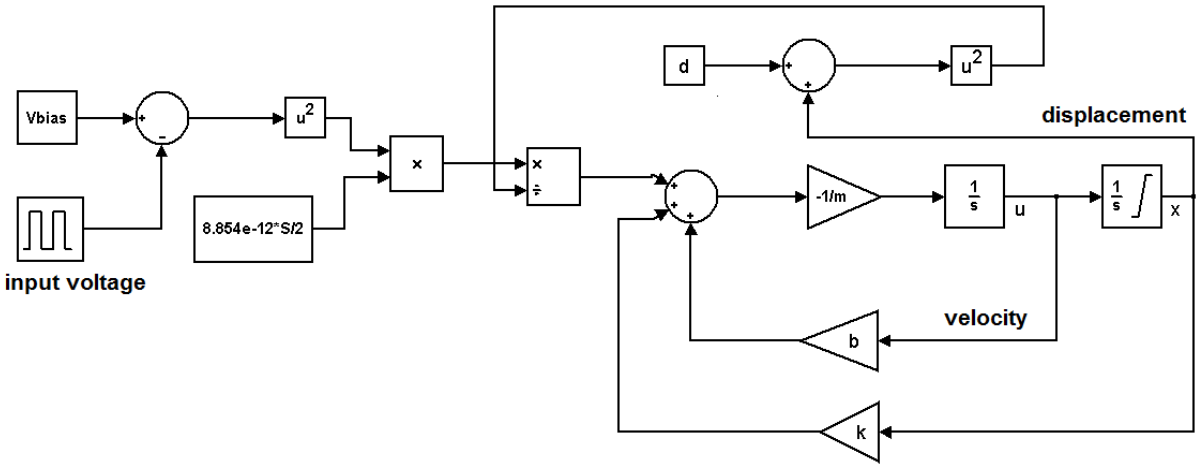

Figure 3.3: The transient 1-D CMUT model implemented in Simulink.

Considering only the range of physically realizable displacement, $-d \leq x \leq 0$, the maximum voltage V can be found to occur at $x = -d/3$. That voltage is known as the pull-in voltage or the collapse voltage. Rearranging (3.6) with $x = -d/3$, the spring constant can be expressed as

$$k = \frac{27\varepsilon S V_{collapse}^2}{8d^3} \tag{3.8}$$

With a measured collapse voltage, $V_{collapse}$, of $75V$, a membrane diameter of $25\mu m$, and a distance of $260nm$ (a cavity depth of $160nm$ and two layers of silicon nitride with a total thickness of $760nm$), the spring constant k is estimated to be $2160N/m$.

When a CMUT is operated in immersion, the damping of the membrane is dominated by the radiation impedance, which arises due to the loading of the medium. The radiation impedance is a complex value that is also a function of frequency. Kinsler et al [36] provided an expression for the radiation impedance of a circular piston in a infinite rigid baffle:

$$Z_r = \rho_0 c S[1 - \frac{J_1(\frac{2wa_{eff}}{c})}{\frac{wa_{eff}}{c}} + j\frac{H_1(\frac{2wa_{eff}}{c})}{\frac{wa_{eff}}{c}}] \tag{3.9}$$

where J_1 is the first order Bessel function, H_1 is the first order Struve function, ρ_0 is

the equilibrium density of the medium, c is the speed of sound in the medium, and w is the angular ultrasound frequency. The expression for the radiation impedance of a clamped circular membrane can also be used, but because the results are used in the spring mass model, the expression of a piston is used instead. If the ultrasound frequency is low ($\frac{wa_{eff}}{c} \ll 1$), which is true for the CMUT in question as the ultrasound frequency is $5.3MHz$ and the membrane radius (a) is $12.5\mu m$, the radiation resistance, or the real part of Z_r can be estimated to the first order as [36]

$$R_r \approx \frac{w^2}{2c}\rho_0 \pi {a_{eff}}^4 \tag{3.10}$$

and the radiation reactance (imaginary part of Z_r) is [36]

$$X_r \approx \frac{8}{3}\rho_0 w {a_{eff}}^3 \tag{3.11}$$

When a CMUT is immersed in a liquid, the radiation impedance dominates the damping, and b can be estimated as the magnitude of Z_r. Given that the density of the medium is $1000kg/m^3$, the speed of sound in the medium is $1500m/s$, and the measured ultrasound frequency is $5.3MHz$ [13], the damping factor b is equal to 5.49×10^{-5}Ns/m. Note that connecting and operating multiple CMUT cells in parallel will increase the radiation impedance because of mutual radiation impedances [40][41]. However, this effect is not modelled here.

The radiation reactance also contributes to the vibration as an added mass and changes the resonant frequency. At low frequency, the mass caused by the radiation reactance is [36]

$$m_r = \frac{X_r}{w} = \frac{8}{3}\rho_0 {a_{eff}}^3 \tag{3.12}$$

which is equal to $1.64\times10^{-12}kg$. The CMUT membrane has a non-zero mass, but it should be much less than the radiation mass, so the radiation mass is a good estimation of the total mass. The value of the mass can be verified by comparing the measured resonant frequency with the calculated one:

$$f = \frac{1}{2\pi}\sqrt{\frac{k_{soft}}{m}} \tag{3.13}$$

where k_{soft} is the weakened spring constant due to the spring softening effect when a bias voltage is applied across the electrodes. The spring softening effect needs to be taken into account because the resonant frequency ($5.3MHz$) was measured with a $60V$ bias voltage. An expression of k_{soft} can be found in [42]:

$$k_{soft} = k - \frac{\varepsilon S V^2}{d^3} \tag{3.14}$$

Here, k_{soft} is $1750N/m$, and the resonant frequency works out to be $5.2MHz$, which matches well with the measured resonant frequency of $5.3MHz$. In fact, the calculated values can be affected by several factors. For example, the membrane shape function is slightly different than the one that the plate theory predicted because the electrostatic force acting on the membrane is not uniform. The measured pull-in voltage is probably lower than the theoretical value because the membrane becomes unstable quickly as it approaches pull-in. Also, the dielectric layer thickness and the cavity depth are not exact.

3.2 Simulation results

Studying the simulation results of the transient model will provide insights on CMUT operation. A bias voltage was connected to the bottom electrode, while a unipolar square voltage pulse was fed to the CMUT top electrode, thus the overall voltage applied across the CMUT is the difference of the two. A unipolar square pulse was used because it is the most common, and the simplest, pulse shape for CMUT pulsers (the electronic circuits that generate the transmit signals). Other pulse shapes such as bipolar, sinusoidal, or multi-cycle pulses can also be used in the model, but they are not investigated here. The typical pulse width of the square pulse is roughly half of the period corresponding to the CMUT resonant frequency, such that the Fourier transform of the input pulse has its main tone at the resonant frequency.

Figures 3.4 and 3.5 show the simulation results with the voltage bias set at $+60V$ and $-60V$ respectively. For both, the plot at the top is the input voltage pulse, and the plots at the middle and bottom are the displacement and velocity of the CMUT membrane

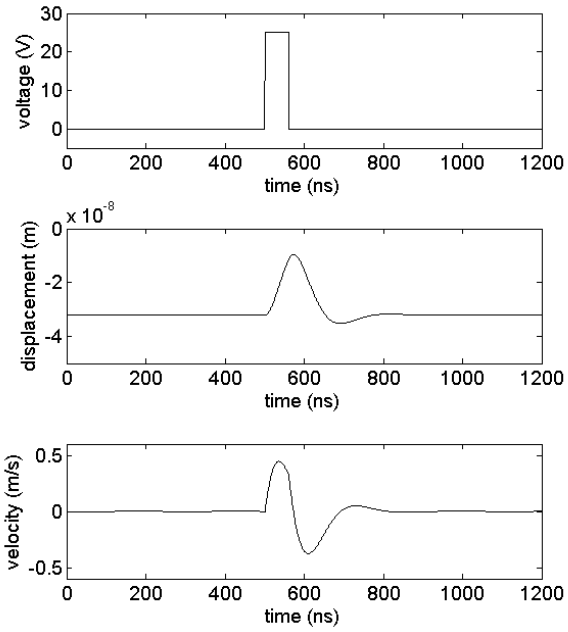

Figure 3.4: Transient model simulation results with bias at +60V.

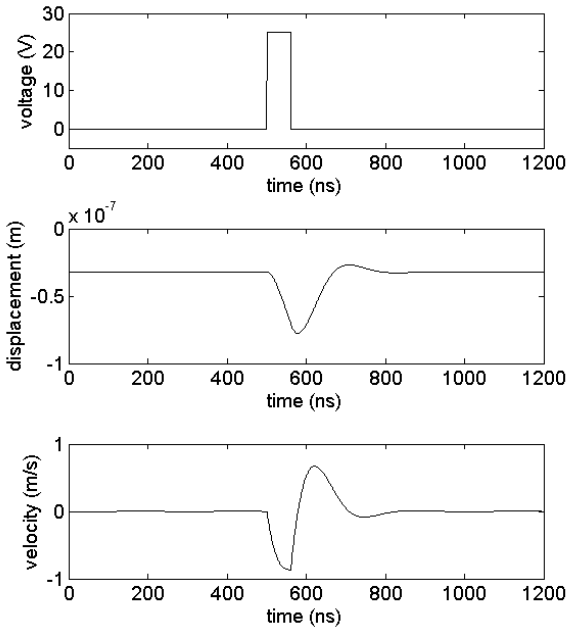

Figure 3.5: Transient model simulation results with bias at -60V.

respectively. For each case, a square pulse with an amplitude of $25V$ was applied at $500ns$, lasting for $60ns$.

Several observations can be made from the simulation results. First, because of the damping provided by the medium, the vibration dies down very quickly. In other words, the second order system has a low quality (Q) factor. Short acoustic pulses are beneficial for imaging applications because shorter pulses in the time domain correspond to wider bandwidths in the frequency domain, resulting in better resolution. As mentioned in the previous chapter, this is one of the reasons that makes CMUTs so attractive compared to conventional piezoelectric transducers.

Secondly, during non-collapse mode operation, the membrane displacement never reaches the cavity depth. Even though the overall voltage across the CMUT at one point ($60+25V$) is greater than the pull-in voltage ($75V$), the pulse is too short and the membrane never has the time to collapse. This fact was mentioned in the previous chapter and it is now shown through modelling. This observation is important because it means that a dielectric layer between the two electrodes is not essential for non-collapse mode CMUTs. Of course, a dielectric layer for non-collapse mode CMUTs can still be useful as it prevents shorting of the two electrodes when a large voltage is applied by mistake.

Finally, when the bias voltage changes sign, the polarities of both the membrane displacement and velocity also change. A $+60V$ bias results in an initial positive membrane velocity, while an initial negative velocity is observed for a $-60V$ bias. In addition, the amplitude of the membrane velocity is greater for a $-60V$ bias because the overall voltage across the CMUT is larger. This CMUT behaviour is unique and can be exploited for interesting imaging techniques. For example, a CMUT can be turned "off" by a $0V$ bias (not completely off but its output is much smaller) so that one or more elements in an array can be selected, as reported in [13] and [43].

3.3 Comparison of simulation to experimental results

The 1-D CMUT model requires a few assumptions and simplifications to be made. The validity of those assumptions can be verified by comparing simulation to experimental

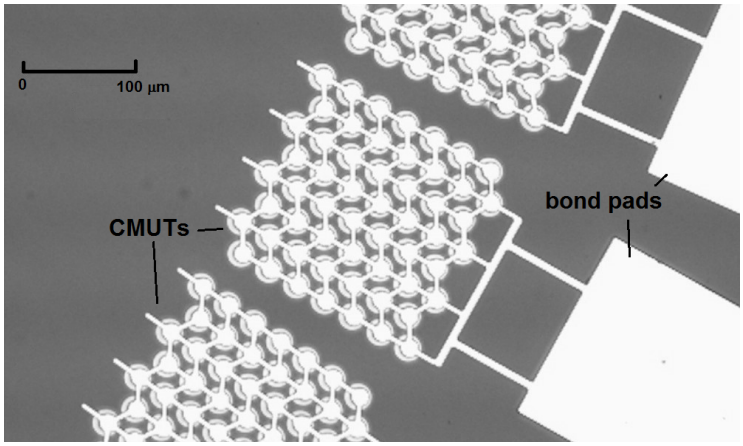

Figure 3.6: Micrograph of the CMUT element used in the experiment.

results.

One element of a CMUT array was used for the measurement. The element consists of 56 CMUT cells, and has a dimension of approximately $200\mu m$ by $200\mu m$. An optical image of the CMUT element is shown in Figure 3.6. The CMUTs were immersed in vegetable oil, and a hydrophone (Onda Corp., Sunnyvale, CA) was positioned directly in front of the CMUT element and $5mm$ away, well in the far field of the aperture, so that the measurement is easier to be characterized, because the pressure is monotonically decreasing as the distance increases in the far field.

The CMUT element was driven by a $25V$ square voltage pulse with a pulse width of $60ns$. The hydrophone system (HGL-0200 hydrophone and AG-2010 pre-amplifier, Onda Corp.) combined to provide a sensitivity of $450nV/Pa$. The pressure can be obtained by dividing the measured voltage by the sensitivity, or in this case $450nV/Pa$. The measured results are shown as the solid lines in Figures 3.7 (a) and (b) for $+60V$ and $-60V$ bias respectively.

It is straightforward to calculate the pressure from the output of the model. The amplitude of the pressure generated by a vibrating circular piston, when measured in the far field, is given in [36]:

$$P_{piston} = \frac{\rho_0 c \pi {a_{eff}}^2 U}{2\lambda r} \tag{3.15}$$

where U is the velocity of the vibrating surface, λ is the wavelength of the acoustic wave, and r is the distance that sound travels. The CMUT element contains 56 cells, which can be considered as point sources because their diameters are much smaller than the wavelength ($a_{eff} \ll \lambda$). In addition, because the dimension of the CMUT element ($200\mu m$) is much smaller than r ($5mm$), the distance r can be considered the same for all cells. Therefore, the total pressure generated by the CMUT element, measured in the far field, is

$$P_{element} = 56\frac{\rho_0 c \pi {a_{eff}}^2 U}{2\lambda r} \tag{3.16}$$

The calculated pressure waveforms are time-shifted to match the measured results, and are shown as dashed lines in Figures 3.7 (a) and (b) for $+60V$ and $-60V$ bias respectively. The simulated and measured pressure amplitudes have the same order of magnitude: they all have peak-to-peak pressure in the range of $5kPa$ to $10kPa$. Given sources of error such as the loss in the medium and the frequency dependence of the hydrophone sensitivity, the amplitude of the membrane velocity calculated by the model can be considered accurate.

However, as evidenced by the quicker settling of the simulated waveforms in Figure 3.7, the model over-estimated the damping factor. Moreover, the measured pressure displays a second pulse with a higher amplitude than the first pulse. For example, in the $+60V$ case, the first (up) pulse did not get above $3kPa$ but the second (down) pulse got to $4kPa$. This asymmetry is not captured by the model. These two discrepancies, damping factor and waveform asymmetry, can be attributed to the fact that the model is a small-signal linear model, thus large-signal and non-linear effects caused by vibration of large amplitude cannot be estimated accurately. Another factor that is not considered in this model is the mutual acoustic interaction between CMUT cells that changes the radiation impedance [40][41]. Nevertheless, a linear 1-D CMUT model is still useful in illustrating CMUT operation and providing engineers with a simple method to estimate CMUT performance parameters.

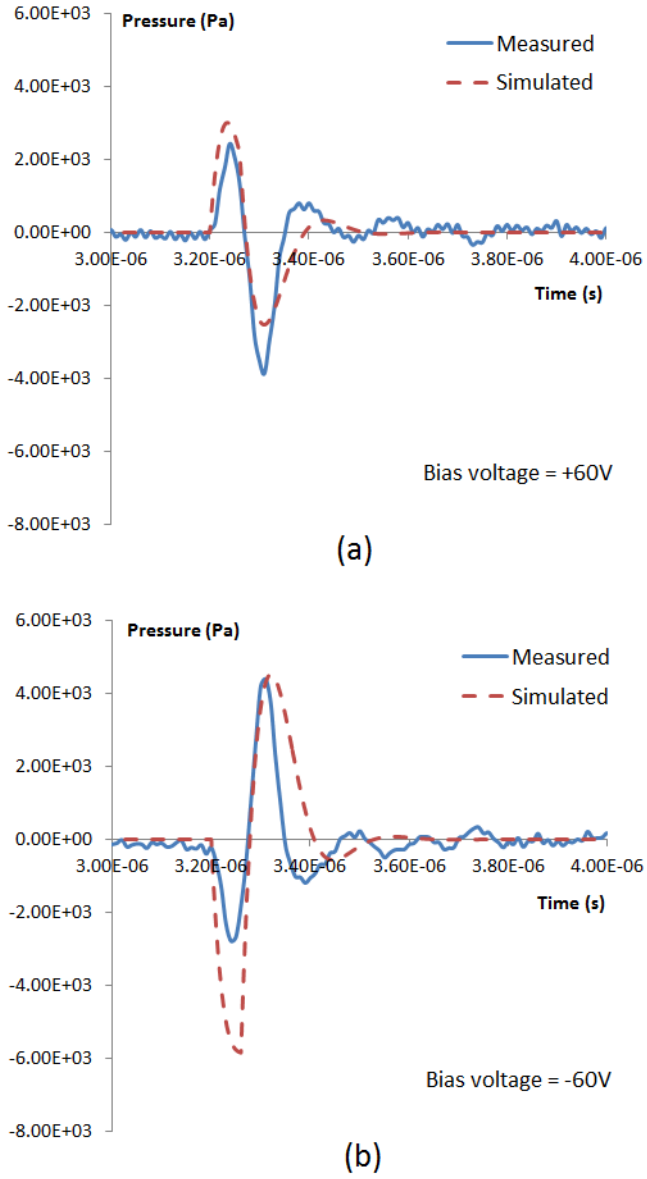

Figure 3.7: Comparison of modelled and measured pressure from the CMUT element, when the bias voltage is (a) +60V and (b) -60V.

Chapter 4

High Density Ultrasonic Arrays

Besides a larger bandwidth, another reason why the CMUT technology is useful for NDT is its potential in the manufacturing of high density ultrasonic arrays. Manufacturing of piezoelectric transducer arrays requires manual dicing of the crystal. Not only is the process tedious and expensive, there is also a limitation on the minimum element size that one can achieve. This chapter begins with an overview of ultrasonic phased arrays, explaining why high density arrays are beneficial. Next, the row-column addressing scheme will be introduced, followed by a detailed analysis of its operation, advantages, and limitations. The chapter concludes by demonstrating NDT surface scanning with a row-column addressed CMUT array.[1]

4.1 Ultrasonic phased arrays

Generating ultrasound images involves getting most of the acoustic energy to, and detecting sound waves reflected from, different points in an area or a volume. Doing so requires two things to happen: focusing and steering of ultrasound beams.

The most basic arrangement of an ultrasonic transducer is the single element transducer. When the entire transducer transmits and receives at the same time, it relies on its geometry

[1]Part of this chapter was submitted for publication in Ultrasonics.

to determine a fixed focal point. Because a transducer has a finite size, the acoustic waves emitted by a transducer behave like plane waves propagating through an opening that has the same size as the transducer, resulting in diffraction. Diffraction causes the acoustic beam to exhibit pressure variation in the volume near the transducer, or the near field, because of constructive and destructive interference. As the distance increases, the transducer behaves more like a point source, thus the sound intensity begins to obey the inverse square law. This region is called the far field. The beam width in the far field increases with the distance. The point where the near field ends is the near field to far field transition, and it is given in [44] for a rectangular transducer:

$$Z_t = 0.339\frac{{L_y}^2}{\lambda} \tag{4.1}$$

where L_y is the width of the transducer in the same direction with respect to the diffraction, and λ is the wavelength of the acoustic wave. At Z_t, the beam width becomes minimum, approximately $0.5L_y$, and the pressure reaches a maximum to twice the pressure at the transducer surface [45]. This point is known as the natural focal spot. Natural focusing of a transducer is illustrated in Figure 4.1(a), with the arrow pointing to the focal spot.

Focusing of the sound beam from a single element transducer is typically achieved by attaching an acoustic lens to the transducer (Figure 4.1(b)) or by changing the curvature of the transducer (Figure 4.1(c)). Both ideas change the direction of the sound waves from different locations of the transducer surface so that the waves interfere with each other constructively at a certain point. However, the sound beam can't be steered unless some kind of mechanical movement, of either the transducer or the test object, is involved. Not only is mechanical movement slow, it also could introduce errors that affect image quality.

The curved transducer can be emulated by a flat transducer if the latter is divided into small segments, or elements (Figure 4.1(d)), and time delays are applied to the elements to match the change in distance due to the curvature. This is the basic idea of phased array focusing and it is illustrated in Figure 4.2. More importantly, the sound beam can be steered, and the focal depth can be adjusted, by changing the time delays. The same principle can be applied to sound reception, when time delays are added to the received signals to make the transducer "listen" to a focused location. This process of applying time delays to steer and focus sound beams is also known as beam-forming.

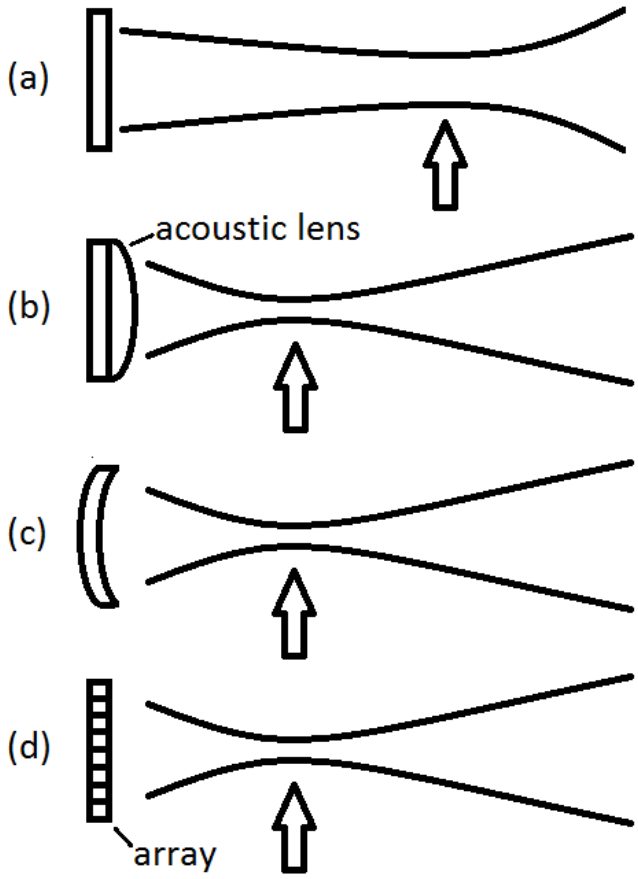

Figure 4.1: Different ways of focusing sound from a transducer: (a) natural focusing, (b) acoustic lens, (c) a curved transducer, and (d) a phased array transducer.

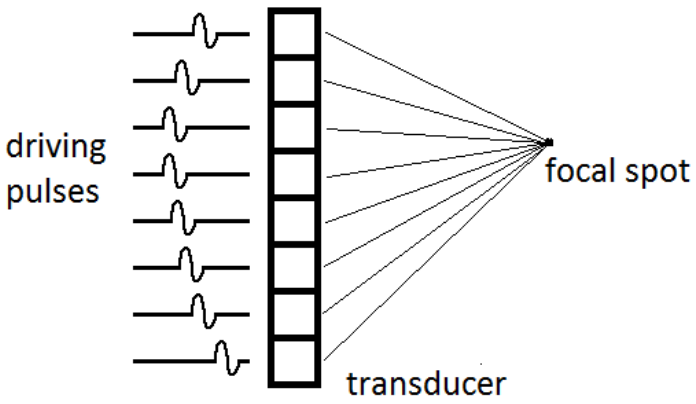

Figure 4.2: Steering and focusing of a sound beam using a 1-D phased array.

It is possible to have other locations that satisfy the constructive interference requirement, resulting in other focal spots. For example, if the acoustic pulse generated by each element is longer than one cycle, constructive interference of waves can still occur at another point because the distance from some of the elements can now be off by one period and still ending up with the same phase at a different location. These unwanted focal spots are called grating lobes. To completely avoid grating lobes, the distance between elements, or the element pitch, needs to be less than or equal to one-half of the wavelength [44]. Therefore, as the ultrasound frequency of an array increases, the element size needs to be reduced and the array density has to go up. And this is why CMUTs, which are manufactured using micromachining processes that have feature size in the *mum* range, are perfect for transducer arrays.

Figure 4.2 shows a 1-D array that consists of elements arranged on a straight line. A 1-D array can focus and steer sound on a plane perpendicular to the transducer surface. But, if scanning is required for a volume or for a plane parallel to the transducer surface, a 2-D array is needed.

4.2 2-D phased arrays for NDT

Many NDT applications use 1-D arrays to reduce the need of transducer movement [11]; examples include the contact testing of steel [46] and the inspection of aircraft [47]. In [47], a 64-element 1-D array was employed to increase the inspection speed of surfaces on aircraft. The array was immersed in a fluid-filled probe, and surface scans were performed with the probe moving in one direction. It was concluded that the scan speed was limited by the time it took to maintain good contact between the probe and the scanned surface. For this example, employing 2-D arrays can be beneficial because 2-D arrays reduce the frequency of transducer movement by providing an additional dimension where the sound beam can be steered and focused. However, while 1-D ultrasonic array NDT transducers have gained popularity in recent years [11], the adoption of 2-D arrays has been slow.

The main obstacle faced by NDT 2-D arrays is the complexity of the imaging, or scanning, systems. For a system using a fully-populated N by N array, the best performance and flexibility can be achieved if each element in the array can be controlled individually. However, such a transducer requires the number of elements, as well as the number of connections to the array, to increase quadratically as the size of the array goes up. For example, a modestly sized 32 by 32 array requires over 1,000 array controller channels, resulting in a complex design and making the control difficult. As a result, different 2-D array configurations and driving strategies have been proposed [11]. For example, the Mills cross configuration (elements arranged in the shape of a cross) and the circular array (elements arranged in a circle) were investigated and compared with the fully-populated array by Mondal et al. [48]. Furthermore, a sparse array (one that does not use all elements for transmit and/or receive) for NDT was presented in [49].

The main difference between an NDT ultrasonic scanning system and a medical imaging system is that the test objects are usually not moving for NDT systems. Therefore, a fast scan rate is usually not required. In addition, noise in the signals can be reduced by making multiple scans and applying averaging on the acquired signals.

4.3 Row-column addressing scheme

Scanning system complexity needs to be reduced before 2-D arrays can find their way into commercial NDT solutions. One way to reduce the number of interconnects significantly is the use of row-column addressed arrays. It was first proposed by Morton and Lockwood [50], who called the configuration a cross-electrode array. In 2009, an implementation of a row-column addressed 2-D array for rectilinear imaging was reported in [51]. Designing row-column addressed arrays using the CMUT technology was proposed in [52], but an actual implementation was not reported. The first row-column addressed CMUT array was reported in [53]. More recently, Top Orthogonal to Bottom Electrode (TOBE) arrays, which is another name for row-column addressed arrays, were proposed for photoacoustic imaging [54][55]. The same group from University of Alberta also made several contributions to row-column addressed array research such as synthetic aperture transmit focusing [43] to improve the image resolution when the object is out of the transmit focal plane, S-Sequence encoding schemes [56] to improve the image SNR, and modulation encoding that can potentially enabling readout of signals from all elements of a 2D array simultaneously [57]. Finally, an open-grid support structure was used to fabricate row-column addressed arrays in [58].

Row-column addressed arrays look similar to regular individually addressed 2-D arrays. The main difference, however, is that instead of having two dedicated connections for each element, elements on the same row/column share the same row/column connection, or pad. For example, if all the top electrodes are connected in rows, and the bottom electrodes are connected in columns, sending a pulse from the element in row 1 and column 1 requires applying a voltage signal between the first row pad and the first column pad, as shown in Figure 4.3(a). Similarly, a signal across the third row pad and the third column pad will activate the element in row 3 and column 3 (Figure 4.3(b)). However, if both elements are activated, two other elements are then forced to be turned on (Figure 4.3(c)). Thus, flexibility is sacrificed in favour of fewer connections. Figure 4.4 shows a CMUT row-column addressed array.

The most basic way of controlling a row-column addressed array is the row-column addressing scheme, as discussed in [50], [51], and [59], and it is illustrated in Figure 4.5. In

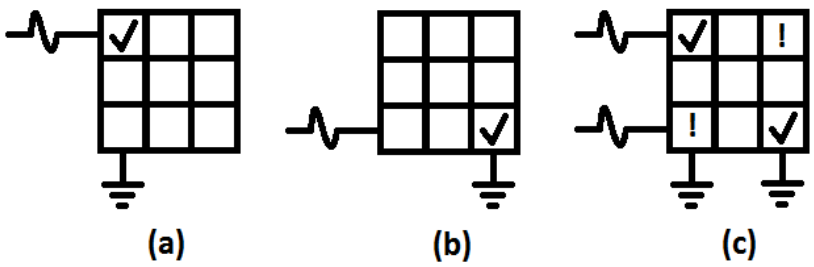

Figure 4.3: Operation of a row-column addressed array: (a) element (1,1) is activated, (b) element (3,3) is activated, (c) when both elements are activated, elements (1,3) and (3,1) are forced to be turned on.

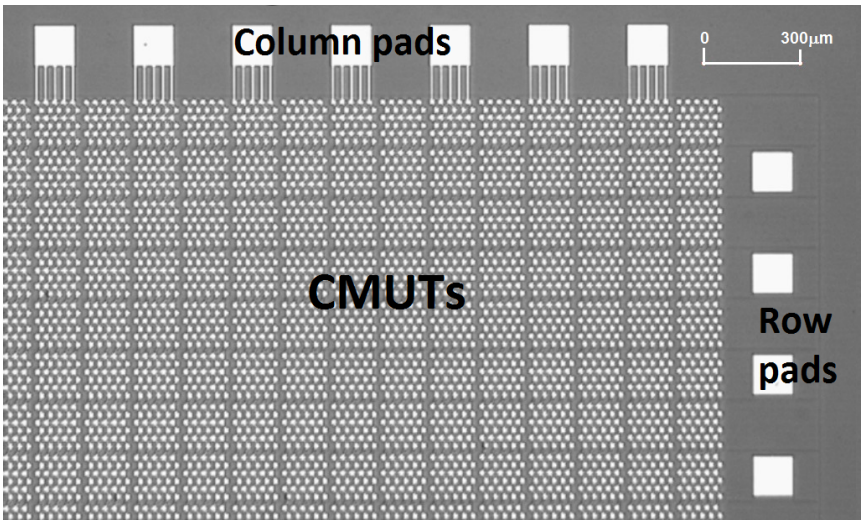

Figure 4.4: Micrograph of a row-column addressed CMUT array.

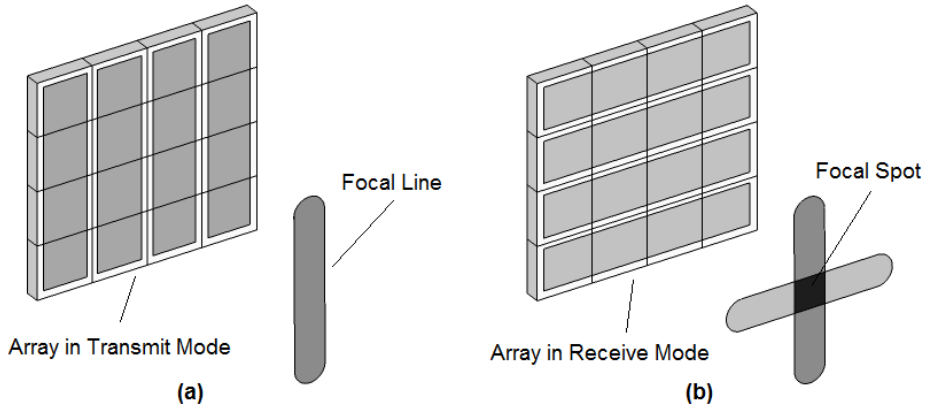

Figure 4.5: Operating principle of row-column addressing scheme. (a) Transmit mode, (b) Receive mode.

this example, all the elements in the same column are connected through the top electrodes, and the bottom electrodes are connected in rows. If electrical pulses are applied to the columns when all the rows are connected to a constant bias voltage, the array becomes a 1-D array that generates a vertical line of focus, as shown in Figure 4.5(a). On the other hand, if all the columns are connected together and each row is addressed individually, a rotated 1-D array that generates a horizontal focal line, as shown in Figure 4.5(b), is produced. Instead of transmitting, the rotated array is in receiving mode; however, due to the principle of reciprocity, the effects on the beam profile can be considered the same regardless of whether the aperture is transmitting or receiving. As a result, if a row-column addressed array is configured such that a 1-D array is used to transmit and a rotated 1-D array is used to receive, the response is the convolution of two focal lines, resulting in a focal spot. Changing the location of the focal spot can then be achieved by adjusting the focal line locations of both the transmitting and the receiving operations. In summary, the row-column addressing scheme involves transmit beam-forming on one direction, for example the azimuth, and receive beam-forming on the other direction, for example the elevation.

4.4 Modelling of the row-column addressing scheme

To gain a better understanding of the row-column addressing scheme, one needs to model the sound field generated by the array. In Chapter 3, the CMUT model was created with the assumption that the output pressure was measured in the far field, because diffraction makes the pressure in the near field difficult to predict analytically. Fortunately, simulation tools are available to model the acoustic domain, including the near field, numerically. Field-II [60] [61], a program that calculates the ultrasound field based on the spatial impulse response of a transducer, is used in this section.

The active area of the array that generates ultrasound, or the aperture, must first be defined. Based on the CMUT array described in [59], the transmit aperture was defined as a 1-D array of 32 elements, with element height, element width and kerf set to $4.8mm(19.8\lambda)$, $0.13mm(0.54\lambda)$, and $0.02mm(0.08\lambda)$ respectively. The receive aperture was defined similarly as the transmit aperture but with a 90-degree rotation. A $5.9MHz$ sinusoidal pulse in a Hanning window was used as the impulse response for each element.

The operating principle of row-column addressing scheme deserves to be revisited through modelling because the exercise will also provide insights on picking a suitable distance, or depth, between the transducer and the test object. The near-field to far-field transition of the $4.8mm$ by $4.8mm$ transducer is $32.2mm$ in both the azimuth and the elevation directions. It is essential to place the test object in the near-field (a distance of less than $32.2mm$) so that focusing can be done.

Figure 4.6(a) shows the transmit beam pressure profile $20mm(82.5\lambda)$ away from the transducer when the row-column addressed array is focused at that distance. The focal line is at the center of the plot. Therefore, the center point, when both azimuth and elevation are at $0mm$, represents maximum pressure and has a value of $0dB$. Each line in the contour represents a $6dB$ step. The $6dB$ beam width and height are $1.6mm$ and $4.7mm$ respectively. The receive beam profile in Figure 4.6(b) is just a 90-degree rotation of the Figure 4.6(a) because of the principle of acoustic reciprocity; it was obtained from the transpose of the transmit data matrix. Combining the transmit and receive beam profiles results in a focal spot, as illustrated in Figure 4.6(c). This third contour plot is the product, or the sum in dB, of the first two plots. The focal spot in Figure 4.6(c) has a

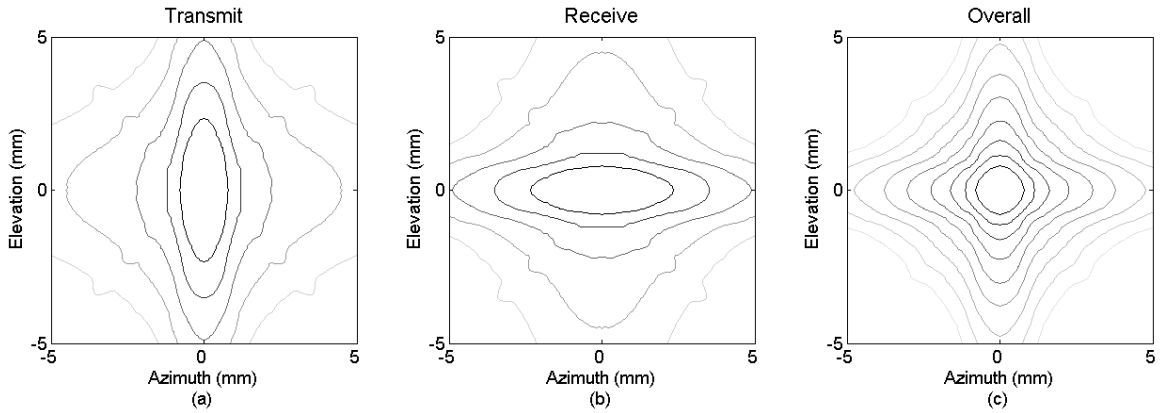

Figure 4.6: Simulated beam pressure profile at depth = 20mm due to (a) transmit beam-forming, (b) receive beam-forming, and (c) a combination of transmit and receive beam-forming; each line represents a 6dB step.

$-6dB$ beam width of $1.6mm$, consistent with the beam width in the transmit beam profile.

The same simulation was repeated but with the focal depth set at $10mm(41.2\lambda)$. The results are shown in Figure 4.7. The transmit $6dB$ beam width and height are $0.8mm$ and $4.9mm$ respectively. A smaller depth results in a smaller f-number, thus better focusing. The smaller beam width translates into a smaller overall focal spot size. In addition, a larger beam height means that the focal spot can be created further away from the centre. As a result, a smaller depth gives rise to a larger field of view for the array. While it is beneficial to use a smaller focal depth, configuration of the test system and the shape of the test object often dictate the minimum distance between the transducer and the test object. Moreover, as will be shown later in this section, image quality can be affected by a focal depth that is too small relative to the aperture. A focal depth of $10mm$ is chosen as a reasonable distance to demonstrate the row-column addressed CMUT array.

Next, instead of simulating the pressure profile away from the transducer, objects are placed at the focal depth and the transducer is used for both transmitting and receiving. The most common way of characterizing the resolution of an array is to find out its point spread function (PSF), by scanning a point object and finding the size of the point object

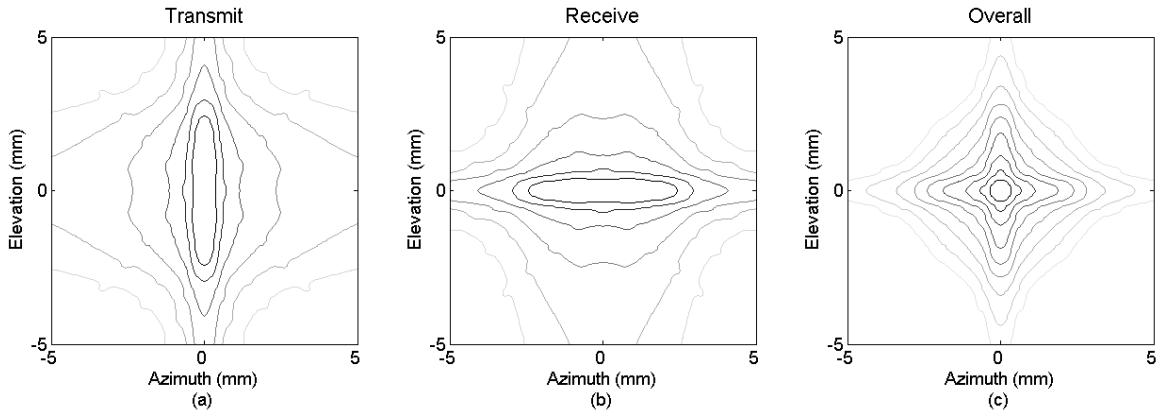

Figure 4.7: Simulated beam pressure profile at depth = 10mm due to (a) transmit beam-forming, (b) receive beam-forming, and (c) a combination of transmit and receive beam-forming; each line represents a 6dB step.

in the resulting image. Figure 4.8 shows the PSF of the array when the point object was placed $10mm$ from the centre of the array. With the point reflector fixed, the array was set to focus at different locations. The maximum amplitudes of the received waveforms were then recorded, normalized, and plotted in a logarithmic scale. The $6dB$ width of the PSF is $0.7mm$. The figure has a dynamic range of $60dB$.

The same PSF simulation was repeated for a regular 2D array with individual element addressing, and the result is shown in Figure 4.9. The PSF of the regular array has a narrower $6dB$ width ($0.5mm$) under the same setting, it also shows less artifact around the object.

Because the application that will be demonstrated later in this chapter is surface scanning, where the object of interest is a flaw, or a void, on a surface, it is more intuitive to consider the reflected acoustic power from different locations for a single focal spot. If an array focuses at a void, the received signal amplitude would be significantly reduced because a large portion of acoustic energy is not reflected back. Therefore, one can quantify the resolution of an array by looking at how much energy is reflected from the focal spot compared to other locations.

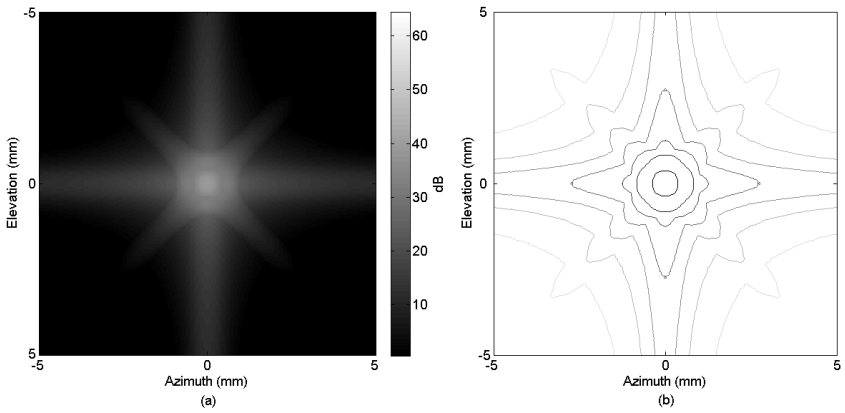

Figure 4.8: Point spread function of a transducer array using the row-column addressing scheme: (a) an image of a point object 10mm from the array, (b) the image in a contour plot; each line represents a 6dB step.

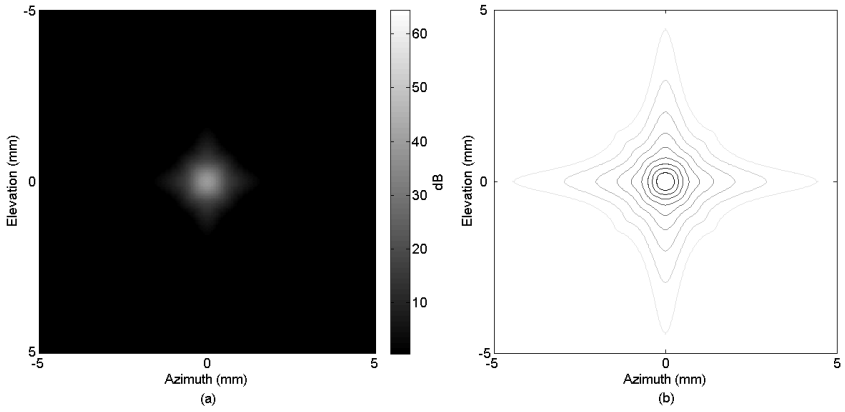

Figure 4.9: Point spread function of a regular 2-D array when elements are individually addresed: (a) an image of a point object 10mm from the array, (b) the image in a contour plot; each line represents a 6dB step.

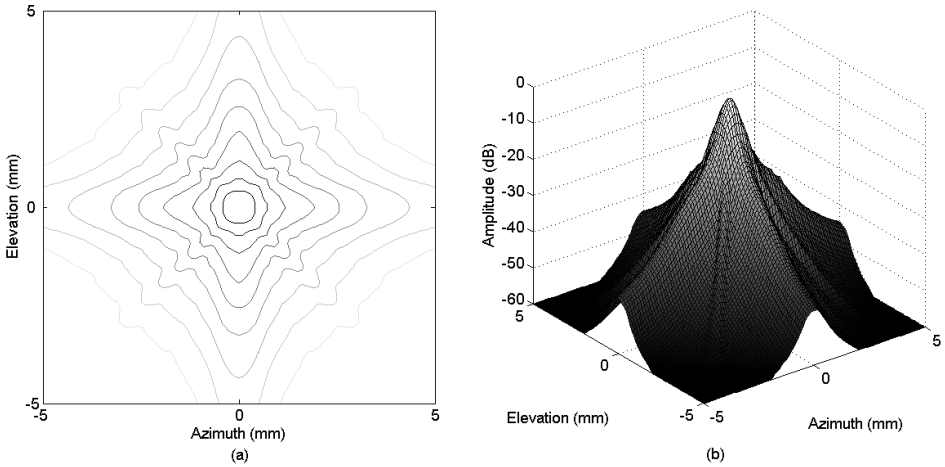

Figure 4.10: Simulated maximum amplitudes of received signals from scatterers on a plane 10mm from the array, the focal spot is set at (0,0); (a) a contour plot with lines representing 6dB steps, and (b) a 3-D plot.

For the next set of simulations, two-way scans were performed with both the transmit and receive apertures focused at centre and $10mm$ away, or at (x, y, z) = $(0, 0, 10)mm$. The process was repeated with the point scatterer set at different points on the $z = 10mm$ plane. The maximum amplitudes of the received envelopes are plotted in Figure 4.10. The received signals have higher amplitudes near the focal spot as shown in Figure 4.10(a). When a surface scan, or a C-scan, is performed on a plate, the resulting signal will be the sum of all points in the plot, and the contribution from each point is determined by the amplitude at that location. Therefore, a peak, as shown in Figure 4.10(b), with a smaller top area and a steeper roll-off will result in a better lateral resolution. The $-6dB$ width of the peak in Figure 4.10 is $0.8mm$.

Imaging of point and wire targets using the row-column addressing scheme was reported in [13], and the $-6dB$ lateral width of the target $15mm$ away was found to be between $650\mu m$ and $900\mu m$. Therefore, the $-6dB$ lateral width at $10mm$ away is between $400\mu m$ and $600\mu m$. Thus, the point and wire targets measurement results are consistent with the simulated $-6dB$ lateral width of $0.8mm$ for a distance of $10mm$.

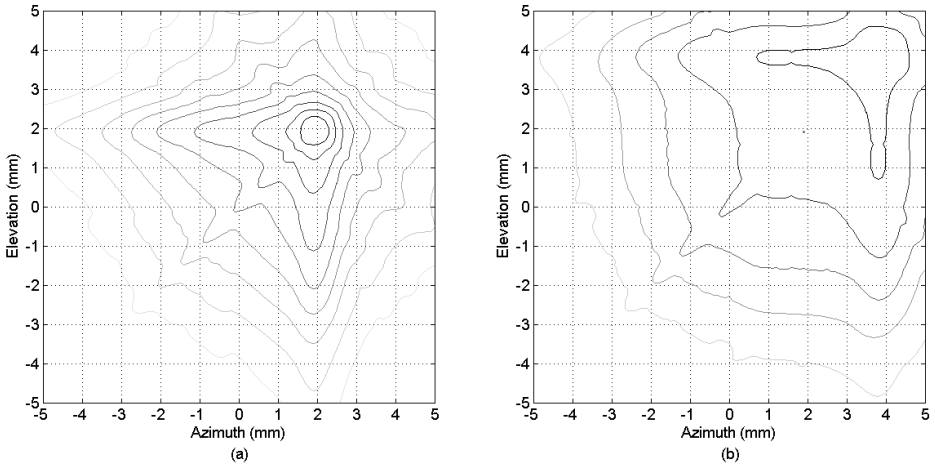

Figure 4.11: Contour plots of simulated maximum received signals from scatterers on a plane at depth=10mm, the focal spot is set at (a) (2, 2) and (b) (4, 4); each line represents a 6dB step.

The simulation of a moving point scatterer was repeated with the row-column addressed array focusing at other locations. Figure 4.11(a) shows a contour plot with the focal spot at (x,y,z) = $(2, 2, 10)mm$. The focal spot or the peak, as expected, is at the correct location. The $-6dB$ width, $0.8mm$, is comparable with the case when the focal spot is at the centre. The array was then set to focus at (x,y,z) = $(4, 4, 10)mm$, as shown in Figure 4.11(b). The focal spot is again at the correct location, but the $-6dB$ width is much larger and the peak is not as sharp, as evidenced by the large distance between contour lines. What happens here is that the focal spot is outside the field of view of the aperture, which is about the same size as the aperture, thus the focusing power of the array gets worse.

The small field of view is a significant limitation of the row column address scheme, compared with regular 2-D arrays. Figure 4.12(a) and (b) are contour plots when a regular 2-D array is used to focus at (x,y,z) = $(0, 0, 10)mm$ and $(4, 4, 10)mm$ respectively. The $-6dB$ width in the centre-focused case is $0.6mm$, which is a slight improvement over the $0.8mm$ achieved by the row-column addressing scheme. In addition, comparing Figure 4.11(b) with Figure 4.12(b), the regular array shows perfect focusing in the area outside

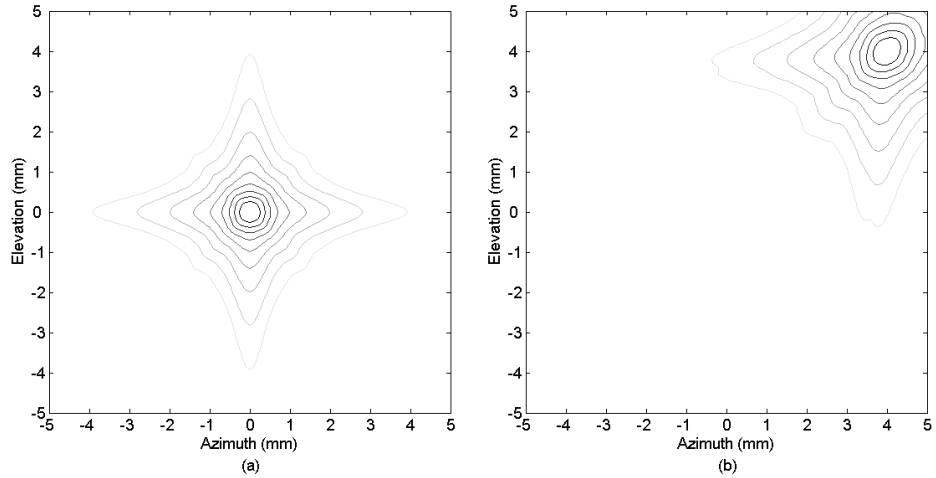

Figure 4.12: Similar contour plots using a regular individual-element addressed 2-D array, the focal spot is set at (a) (0, 0) and (b) (4, 4); each line represents a 6dB step.

the size of the aperture. Thus, the bigger determining factor of whether a row-column addressed array should be used is the required field of view of the applications.

Because the field of view of a row-column addressed array is about the same size as the aperture, using a larger array seems to be a logical solution to overcome the limited field of view problem. However, an aperture that is too large compared to the focal depth could affect the image quality. Figure 4.13 shows 3-D amplitude plots when row-column addressed arrays of various sizes are used to focus at (x,y,z) = $(0, 0, 10)mm$. When the aperture size is $10mm$ by $10mm$, a single peak is still visible at the correct location. However, when the aperture size is increased to $20mm$ by $20mm$ and $40mm$ by $40mm$, unwanted peaks, which will result in image artifacts, appear. These peaks are caused by diffraction because focusing is only done in one direction (azimuth for transmit and elevation for receive), and as a result the focal point is well within the near field in the other direction. This problem can be avoided by increasing the focal depth and the object distance, or by applying defocusing to the array as suggested by [62].

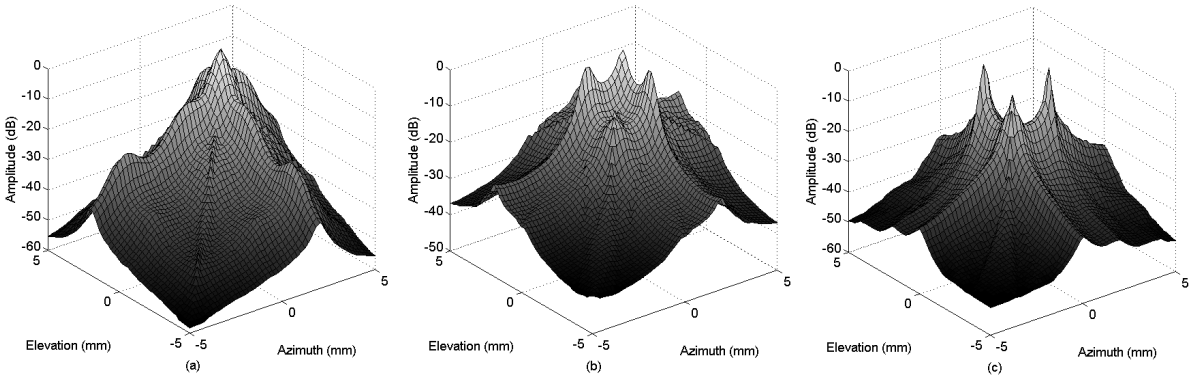

Figure 4.13: Simulated 3-D plots of maximum received amplitudes when a row-column addressed array is focused at (x, y, z)=(2, 2, 10)mm, size of the aperture is (a) 10x10, (b) 20x20, and (c) 40x40.

4.5 Experiments

Surface scanning experiments were performed using the 2-D CMUT array and the row column addressing scheme. The test objects for the experiments are made of polymethyl methacrylate (PMMA), which is also known as acrylic glass. The defect on each test object is mimicked by a hole with a diameter d, which was formed using a laser cutter. A diagram of the test object is illustrated in Figure 4.14(a). Figure 4.14(b) shows a piece of PMMA with a $1mm$-diameter hole ($d = 1mm$). The larger hole on the right is for attaching the test object to a translation stage and it is outside the field of view of the array. The piece of acrylic glass has a thickness of $3mm$.

The experimental setup is shown in Figure 4.15. The 32 by 32 CMUT array was placed on a custom designed printed circuit board (PCB), along with the required front-end electronic circuits. A vegetable oil container was built on the PCB. Vegetable oil was used to prevent damaging the transducer, because the conductive top electrodes of the CMUT array are exposed. This problem can be avoided in the future when an insulating protective layer is put on top of the CMUT array. The PMMA test object, supported by a translation stage, was placed in the vegetable oil, $10mm$ away from the transducer.

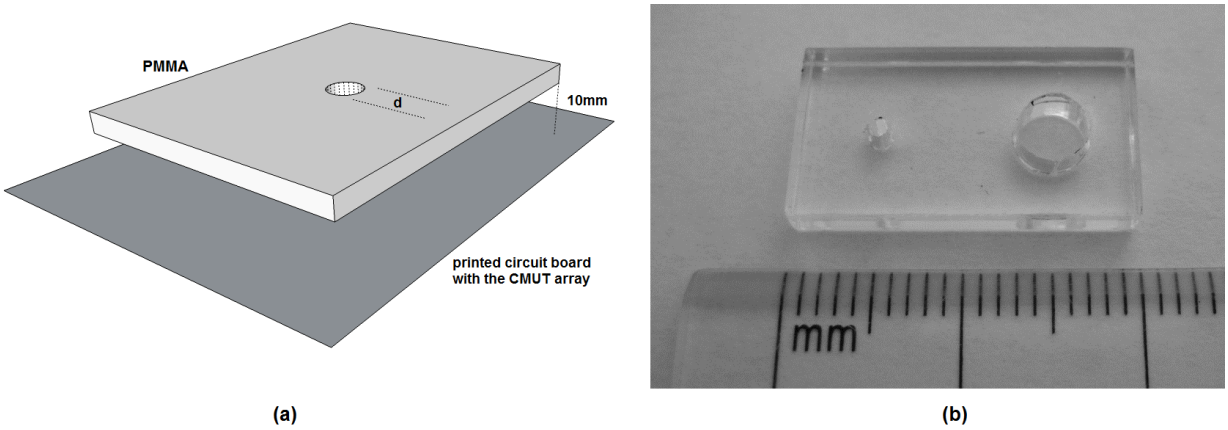

Figure 4.14: (a) A 3-D illustration and (b) an image of the test object. The hole diameter, d, is 1mm in the image; the larger hole on the right is for fastening purpose.

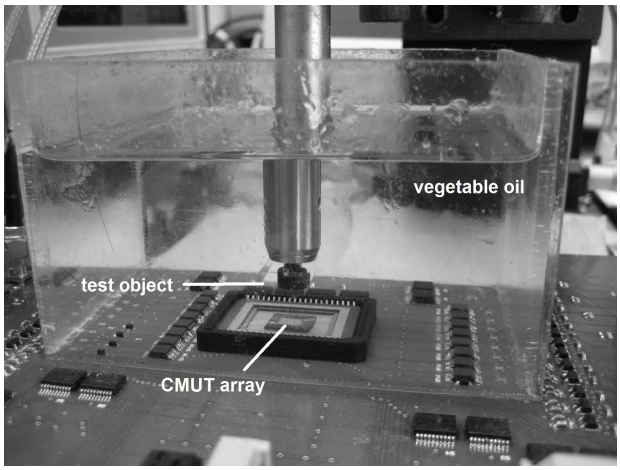

Figure 4.15: A photograph of the surface scanning experimental setup.

The schematic of the PCB is illustrated in Figure 4.16. The transmit beamformer was implemented with a Spartan-3 FPGA (Xilinx Inc., San Jose, CA) that ran on a synthesized clock frequency of $250MHz$. The array was programmed to focus on a plane $10mm$ away. The focal line was set to $-2.0mm$ to $2.0mm$ in the azimuth direction, in $0.1mm$ steps. The FPGA outputs were connected to high-voltage switches (ADG-333, Analog Devices Inc.), which sent $30V$ unipolar square pulses to the column pads. The CMUT array outputs, from the row pads, were connected to transimpedance amplifiers (based on OPA 657, Texas Instruments, Dallas TX) with a gain of $10k\Omega$, and the output voltages were recorded using a digital oscilloscope (DSO7104B, Agilent Technologies, Santa Clara CA). Detailed explanation of the CMUT front-end circuits is provided in the next chapter.

Each waveform was averaged 32 times and was stored with a time-step of $5ns$. Receive beam-forming that involves delaying and summing and the subsequent steps were done in Matlab (The Mathworks Inc., Natick, MA). The receive focus was also set to $-2.0mm$ to $2.0mm$ in $0.1mm$ steps, but in the elevation direction. Hilbert transform was then applied to the resulting waveforms. Finally, the maximum amplitudes of the envelopes were plotted in a logarithmic scale. No apodization was applied to either transmit or receive beam-forming.

Figure 4.17 shows a scanned image of the PMMA with a $1mm$ hole, $10mm$ from the transducer. Again, transmit beam-forming was done in the azimuth direction (left to right), and receive beam-forming was done in the elevation direction (bottom to top). The dark circle, pointed to by the arrow, is clearly visible in the middle, centring at around azimuth = $0.25mm$ and elevation = $-0.5mm$, but there are some dark areas along the sides of the image. These dark areas appear for two reasons. First, because points in the beam pressure profile do not have constant amplitudes, the maximum received signal will be different as the scan angle changes. Focusing at the center will result in a larger signal compared to focusing at the corners, because the beam focal line has a maximum pressure at the center. However, given the chosen scan area of $2mm$ by $2mm$, this effect only accounts for a maximum difference of less than $10dB$. A second factor that makes a bigger contribution to the dark areas is the acoustic reflectivity of the test object. When the sound waves hit the test object on an angle, a large portion of the wave reflects away from the source. The further away the focal spot is from the center, the more likely that

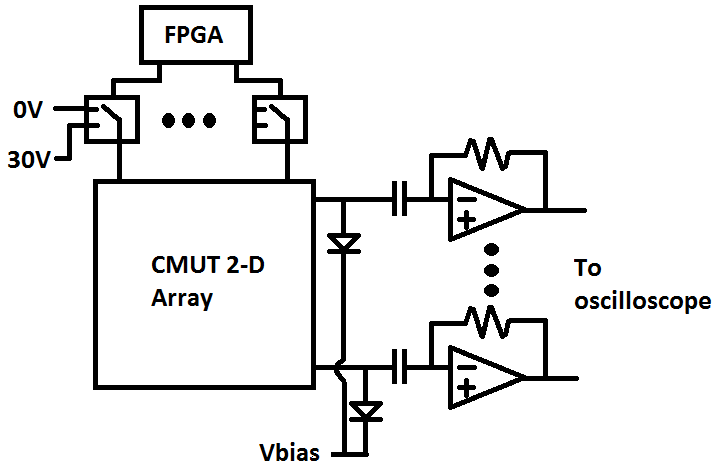

Figure 4.16: Block diagram illustrating schematic of the PCB for row-column array experiments.

the reflected wave cannot get back to the transducer surface, thus resulting in a smaller received signal. This effect is more pronounced in the azimuth direction, which is the direction of the transmit beam steering.

The dark areas do not affect flaw detection accuracy if the hole is at the centre of the aperture. However, if the hole is located close to the edge of the aperture, as shown in Figure 4.18(a), identification of the hole becomes difficult. Fortunately, it is possible to remove the dark areas on the edges by applying compensations to the images. Because the reflectivity of the test object is highly dependent on the surface roughness, which cannot be predicted accurately and consistently for different materials, the simplest solution to compensate for the uneven received signal amplitudes is to use a reference object. While the use of a reference may not be feasible in medical imaging, it is reasonable to assume that reference objects are available in NDT applications. A perfect piece of PMMA, with no holes, was imaged and the received signals were stored as the reference levels, as shown in Figure 4.18(b). Figure 4.18(c) shows the result of subtracting the raw data by the reference levels. The adjusted data were linearly shifted such that the maximum value stayed at $0dB$. The compensated image shows a better defined hole shape, thus proving

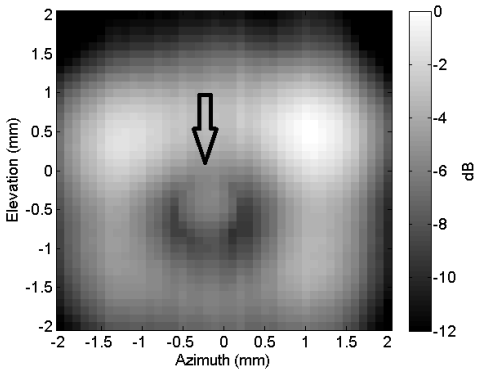

Figure 4.17: Measured image of a 1mm hole on a piece of PMMA 10mm away from the transducer.

that the CMUT array can capture holes that are off-centred.

The experiment was repeated with another piece of PMMA with a smaller hole. The hole has a diameter of $0.5mm$, which is smaller than beam width ($0.8mm$) shown in Figure 4.10. Figures 4.19(a) and (b) show the raw data and compensated images of the $0.5mm$ hole respectively. The hole location can still be identified (centring at around azimuth = $0.5mm$ and elevation = $1.0mm$), but the circular shape of the hole is not as well defined compared to Figure 4.18(c). When the hole diameter is smaller than the beam width, a significant amount of acoustic energy still gets reflected even if the focal spot is near the hole, thus the contrast between the hole and normal region is reduced. The $6dB$ beam width can be a good rule of thumb in determining the minimum hole size that the array can detect. In this case, the resolution of the C-scan image, which was confirmed by experiments as between $0.5mm$ and $1mm$, can be estimated as the $6dB$ beam width, or $0.8mm$.

4.6 Discussion

In this chapter, the row column addressing scheme was introduced and modelled, and a row column addressed CMUT array was demonstrated for surface scanning, showing potential

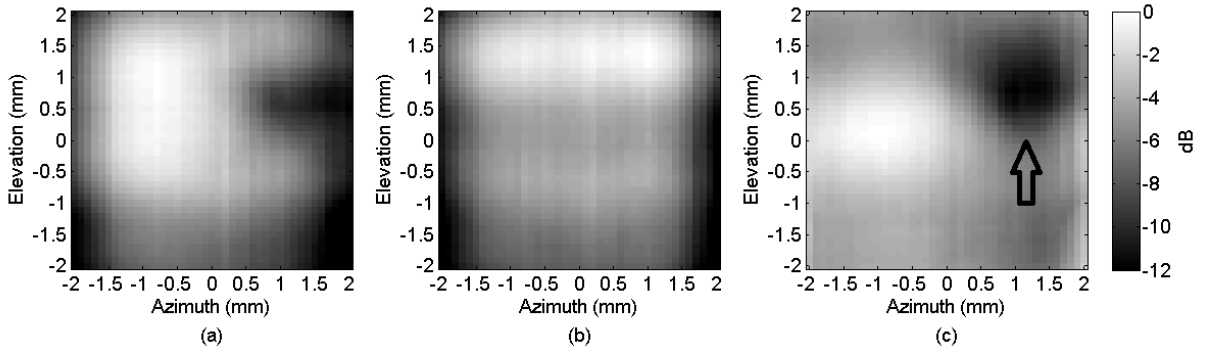

Figure 4.18: Compensation of the image: (a) raw date showing a 1mm hole on a piece of PMMA, (b) captured image of a piece of PMMA with no hole, (c) compensated image: difference of (a) and (b).

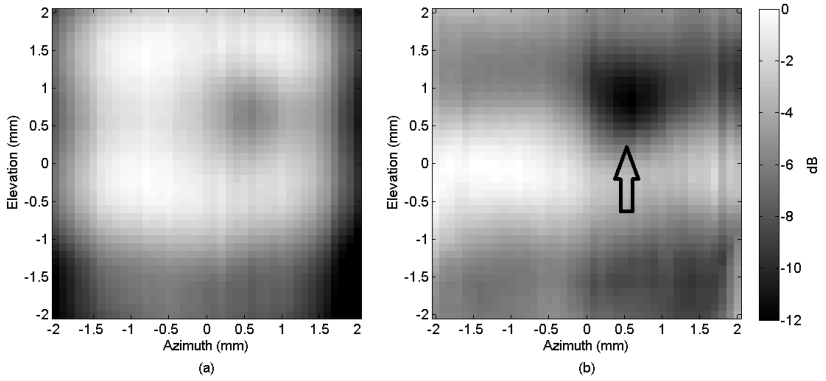

Figure 4.19: Measured images of a 0.5mm hole on a piece of PMMA 10mm away from the transducer: (a) raw data, (b) compensated.

for NDT applications. Two major limitations of the row column addressing scheme are a worse resolution, or a wider beam width, and a smaller field of view compared to regular individual element addressing. To mitigate those two limitations, one can increase the ultrasound frequency and the element count for a higher resolution, and increase the array aperture for a larger field of view. All of these improvements point to the implementation of large-area high-density arrays. While the row column addressing scheme was used as an example in this chapter, other addressing schemes, including individual element addressing, can also be benefited from higher ultrasound frequencies, smaller element pitch, and a larger element count.

CMUT is the technology of choice for the manufacturing of large-area high-density ultrasonic arrays because unlike conventional piezoelectric transducers that require manual dicing of elements, CMUTs are manufactured using micromachining processes that can achieve feature size in μms. Micromachining processes also help ensure element uniformity in large area arrays. In addition, as mentioned in the previous chapter, CMUT elements can be turned off by removing the bias voltage, thus new scanning methods can be made possible by CMUT arrays as demnstrated in [43].

The main obstacle of wide spread adaptation of CMUT array for NDT remains the fact that CMUTs require a coupling medium; as a result, direct contact with test objects is not possible. Nevertheless, there are still many NDT applications that require the transducer to be immersed. As ultrasonic NDT techniques advance and the demand of high performance 2-D transducer arrays increases, CMUT will emerge as a technology that can revolutionize NDT transducer arrays design.

Chapter 5

Integrated electronic circuits

Another advantage that CMUTs have over conventional piezoelectric transducers is their ease of integration with microelectronic circuits. Because CMUTs are fabricated with micromachining processes, which use similar techniques as integrated circuits fabrication, the transducers can be fabricated on the same chip as the supporting electronic circuits by means of post-processing. In this case, CMUTs can be fabricated on top of the electronic circuits [63][64] or on a separate section, but on the same die, away from the circuits [21][65]. Alternatively, CMUTs can be attached on to the electronic circuit IC by flip-chip bonding [5].

For medical imaging, this high level of integration is obviously beneficial for applications such as IVUS where both the transducer and the supporting electronic circuits need to be situated near the tip of a catheter. For NDT, a highly integrated transducer system is not usually required. However, it is still useful when the point of inspection is not easily accessible, thus a small probe is required to perform the testing. In addition, small transducer systems are also useful for structural health monitoring (SHM) applications where transducers are permanently attached on structures so that ultrasonic scanning is performed periodically to monitor structural damage or fatigue, as a damaged structure will emit acoustic waves when it is under stress. Finally, having the supporting electronic circuits closer to the transducer is always beneficial because it reduces the parasitic capacitance and resistance between the two components, which affects system performance.

Because the front-end circuits are located in integrated circuits specifically designed for CMUTs, they are often referred to as application specific integrated circuits (ASICs). The next section will provide a brief introduction and some examples of CMUT front-end circuits. The front-end circuits that were designed, fabricated, and tested for the CMUTs in our lab will be presented after that.[1]

5.1 Front-end circuits

The front-end circuits for an ultrasonic transducer consist mainly of two components: the receive amplifier and the transmit pulser. The primary function of the receive amplifier is to provide gain to the signal, as close to the transducers as possible, before the signal is corrupted by noise. It also provides the capability to drive low impedance loads. For CMUTs, an additional, and probably most important, function of receive amplifiers is to convert the CMUTs output current into voltage. A transmit pulser is the circuit that generates a pulse to drive the transducer during transmission. The pulse can be of any shape and size (common ones are sinusoid or square pulses) but for CMUTs, especially for IVUS CMUTs, the pulser outputs typically have shapes of unipolar square pulse because it is easy to be generated. The challenge of CMUT pulser design is to provide a high-voltage pulse with pulse width that matches the resonant frequency of the CMUT. Because pulsers are mainly used for MEMS (especially for CMUTs) while receive amplifiers can be found in other analog systems, the focus of this chapter is on pulsers. Nevertheless, the design of receive amplifiers will be discussed briefly.

5.1.1 Receive amplifiers for CMUTs

The main function of a receive amplifier for CMUTs is to convert output current into voltage, and the most straight forward way to achieve that is through a transimpedance amplifier. A transimpedance amplifier, consisting of an operational amplifier (opamp) and

[1]Part of this chapter appeared in the conference proceeding: L. Wong et al., "CMUT Front-End Circuits Designed in a High-Voltage CMOS Process and the Phase Measurement Receiver Circuit", IUS 2012.

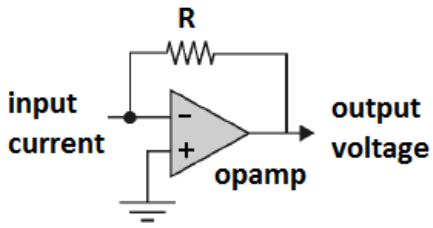

Figure 5.1: A transimpedance amplifier.

a resistor, is shown in Figure 5.1. The basic idea of a transimpedance amplifier is to have a current flowing through a resistor, creating a potential difference. However, using just a resistor at the CMUT terminal will not work because the voltage at the CMUT output will change with the current. The primary function of the opamp, then, is to fixed the voltage at the CMUT output with the virtual short at the opamp input. In Figure 5.1, the voltage at the opamp inverting input (minus) is held to ground (voltage at non-inverting input) because of negative feedback. Because either opamp input terminal has a high impedance, the input current has no where to go but through the resistor. The voltage output is then simply

$$V = -IR \tag{5.1}$$

The negative sign in the equation denote the fact that when current comes out of the CMUT, the voltage at the amplifier output is negative. But when one specifies the gain of a transimpedance amplifier, the negative sign is often omitted.

Because of the simplicity of the circuit, the transimpedance amplifier is often used in CMUT ASICs [5][65]. The circuit described in [65] is slightly different as a metal-oxide semiconductor (MOS) transistor in the triode region was used instead of a resistor, as illustrated in Figure 5.2. Using a MOS transistor in that way reduces parasitic capacitance and provides an option of adjusting the resistance by changing the transistor gate voltage. However, the output voltage is limited to the drain-source saturation voltage of the transistor; otherwise the transistor will go into saturation and the resistance will not stay constant.

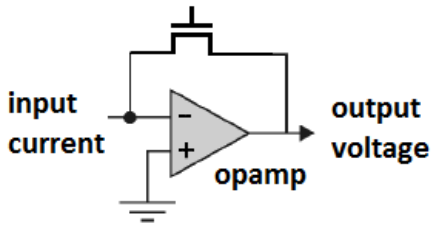

Figure 5.2: A transimpedance amplifier using a MOS transistor as the feedback element.

One potential limitation of transimpedance amplifiers is that the amplifier can become unstable if the output capacitive load is too high or the feedback resistor is too large. One way to combat the instability problem is to add a feedback capacitor in parallel with the feedback resistor. This way the bandwidth of the amplifier is limited by the feedback components, but the feedback factor at high frequency is also reduced so the circuit becomes more stable. Nevertheless, a carefully designed opamp can eliminate the need of the feedback capacitor [66]. Another circuit topology that can convert CMUT output current into voltage is the charge amplifier [67]. However, the theory behind charge amplifiers is not described here.

5.1.2 Transmit pulsers for CMUTs

The pulsers output can be of different shapes, but for CMUT ASICs, square pulse shapes are usually used because other pulse shapes will require on-chip digital-to-analog converters (DACs) or high-voltage amplifiers, and either option will take up a lot of chip space. Some common pulse shapes are illustrated in Figure 5.3. The rising and falling edges are not drawn as vertical lines because of the finite output current of the pulsers. The unipolar pulse (Figure 5.3(a)) is the simplest and most common pulse shape. It consists of two transitions (one rising and one falling) with two voltage levels. The bipolar pulse (Figure 5.3(b)) is an extension of the unipolar pulse. It resembles a sinusoid shape; therefore, the width of the bipolar pulse should match the period of the CMUT resonant frequency. From there, one can also deduce the optimal pulse width of unipolar pulses to be half the

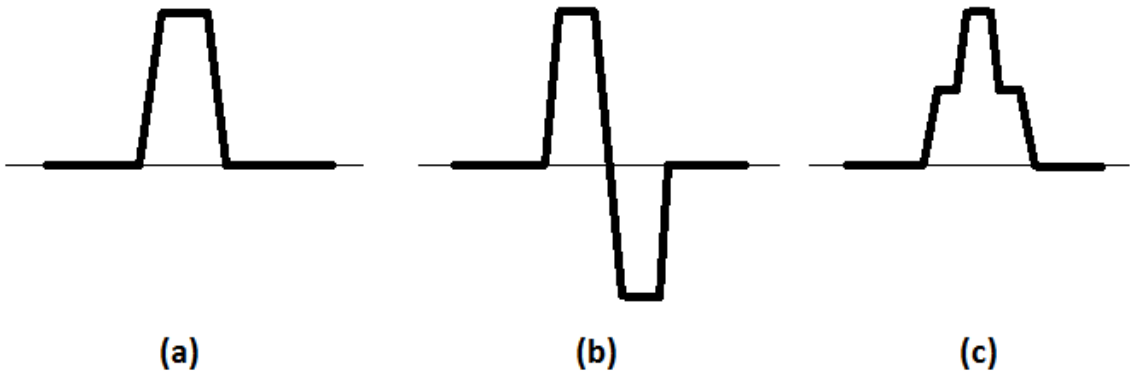

Figure 5.3: Examples of different square pulse shapes: (a) unipolar, (b) bipolar, (c) 3-level unipolar.

period of the CMUT resonant frequency. The 3-level unipolar pulse, as proposed by [68], adds another voltage level in the middle of both the rising and falling edges of the unipolar pulse to improve the efficiency of the CMUT.

Most of the circuit examples in the literature deal with the unipolar pulse shape because of its simplicity. Pulsers that generate unipolar pulses work just like digital buffers, except that pulsers generate signals of much higher amplitude ($20V$ or $30V$ pulses are not uncommon). Several examples of pulser design are illustrated in Figure 5.4. The simplest form, consisting of one N-channel MOS transistor (NMOS) and one resistor, is shown in Figure 5.4(a). Because this design involves so few components, it works really well as long as the output capacitive load is small. If the capacitive load is large, the rising edge is limited by the RC time constant created by the resistor and the load. The rising edge can be sped up by using a smaller resistance, but that will in turn affect the falling edge by taking current away from the MOS transistor when it is turned on.

The second example in 5.4(b) was used in [69]. This design used a push-pull output stage to drive the CMUT, so that the rising and falling edges can be optimized independently. The left side of the circuit served as a level shifter that biases the P-channel MOS

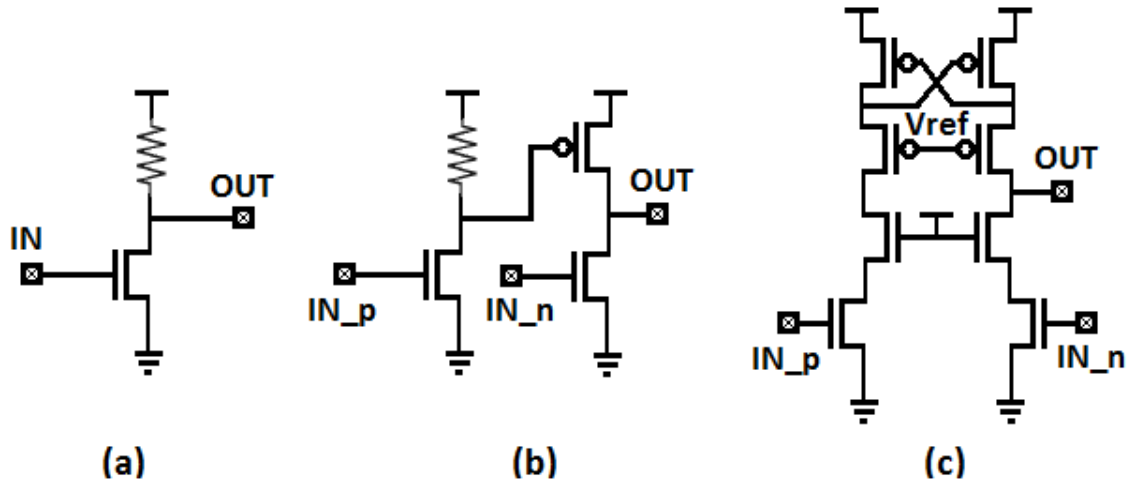

Figure 5.4: Examples of different pulser circuits square pulse shapes: (a) unipolar, (b) bipolar, (c) 3-level unipolar.

(PMOS) transistor in the output stage. The problem with this approach is that the gate voltage of the PMOS transistor depends mainly on the resistance and does not track well with the threshold voltage of the PMOS transistor.

The third and last example, proposed by [5], employed a cascode setup and used high-voltage transistors as the cascode devices to protection the low-voltage devices at the top and bottom. The top two transistors were connected in a latch configuration to speed up the switching. The limitation of this design is that the reference voltage (V_{ref}) needs to track with the transistor. A biasing circuit could have been implemented with the pulser, but it was not described in [5].

Because the pulsers are required to generate high-voltage output, high-voltage fabrication processes are typically required to avoid break downs of transistors. A high-voltage CMOS process is described in the next section.

5.2 High voltage CMOS process

Because of the high-voltage requirement of the pulser, a high-voltage microelectronic process is necessary. A $0.8\mu m$ high-voltage CMOS process developed by Teledyne DALSA was used to fabricated ASICs for our CMUTs. This process offers both low- and high-voltage devices. The low-voltage transistors were used to build receive amplifiers while both types of transistors are required for the pulsers. The high-voltage devices, known as lateral double diffused MOS (LDMOS) transistors, have breakdown voltages as high as $300V$. Note that normal transistors in this process only have a drain-to-source breakdown voltage of $5V$, which is also the typical supply voltage of this process. The high breakdown voltage only applies to the drain-to-source voltage, as the gate-to-source voltage has to be kept below $5V$. This poses a challenge to the circuit design because the gates must be biased properly to prevent gate oxide breakdown.

Models and layouts of predefined high-voltage transistors are provided by the foundry. Therefore, dimensions of high-voltage transistors in the design must be multiple of some predefined values. The standard cell approach reduces the design flexibility but increases the accuracy of the models and the reliability of the devices. The layout of a P-channel LDMOS is shown in Figure 5.5. The gate of this transistor has a width of $134\mu m$ and a length $3\mu m$. Because of a large N-well (a doped region on the silicon substrate) and a guard ring, the dimension of the device layout is $121\mu m$ by $121\mu m$. At maximum gate voltage, this transistor provides a drain current of $7.4mA$ in saturation. Therefore, a pulser that drives large capacitive load will easily have its area dominated by high-voltage transistors.

The Teledyna DALSA process also offers on-chip resistors and capacitors. Capacitors were not used in the ASIC design but polysilicon resistors with a resistivity of $5k\Omega/square$ were used in the biasing circuit and as the feedback resistor of the receive amplifier.

5.3 Circuit design

The schematic capture and circuit layout were done in the Cadence Virtuoso Design Environment, and circuit simulations were performed using Spectre, a SPICE-class simulator

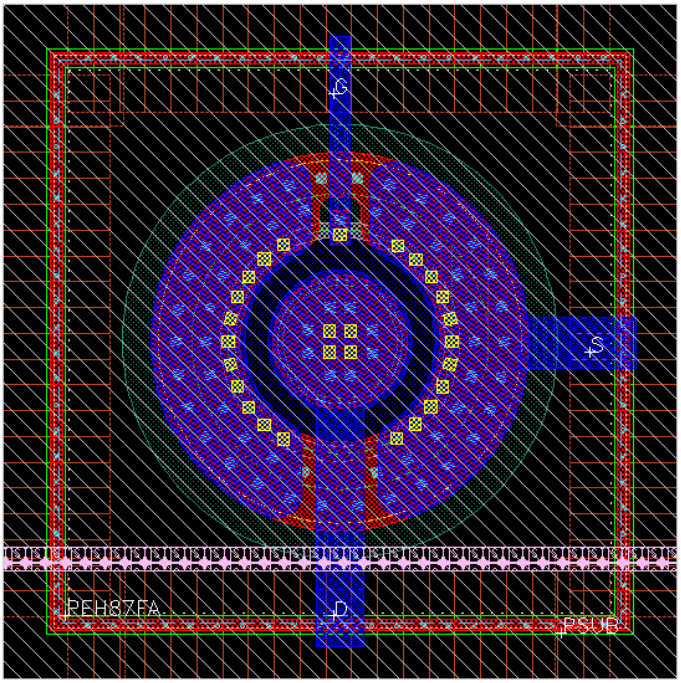

Figure 5.5: Layout of P-channel high voltage transistor.

that was also developed by Cadence Design Systems.

5.3.1 Receive amplifier

The schematic of the receive amplifier is shown in Figure 5.6. The topology chosen for the receive amplifier is the transimpedance amplifier. Comparing Figure 5.6 with Figure 5.1, R1 is the feedback resistor, while the remaining components constitute the opamp. The nodes I_{in} and V_{out} correspond to the points "input current" and "output voltage" in Figure 5.1 respectively. The point labelled "ref" denotes a reference voltage. It is the non-inverting input terminal of the opamp, where the ground is in Figure 5.1. In the actual receive amplifier, ground was not used as the reference voltage because the substrate, with the lowest potential of the circuit, was connected to ground. Instead, a voltage half-way between the supply voltage(VDD) and the ground was used as a reference, which can still be considered as an AC ground.

In order to minimize the chip area, a single-stage opamp design was used. A single-stage opamp in a transimpedance amplifier configuration creates a feedback path with only one dominant pole, thus the circuit is guaranteed to be stable. On the other hand, using multiple gain stages in the opamp requires a compensation capacitor, which takes up chip area and draws more current. However, having only one gain stage means a lower DC gain. The implication of a lower DC gain is that the final transimpedance gain is less accurate.

The parameters of components in the receive amplifier schematic are listed in Table 5.1. PMOS transistors were used as the input pair to reduce the 1/f noise of the opamp. Because the minimum transistor length of this process is $0.8\mu m$, all the transistors in the signal path were assigned lengths of $1\mu m$. M5 and M6 serve as a current mirror, so their length were doubled to improve the output resistance of the current source. Given that the CMUT resonant frequency and bandwidth, one can optimize the circuit to provide just enough bandwidth, so that current consumption and/or circuit area are minimized. However, because this circuit was implemented in a test chip (so neither current consumption nor circuit area was important) and it was expected to work with CMUTs of different resonant frequencies and bandwidths, circuit optimization was not attempted.

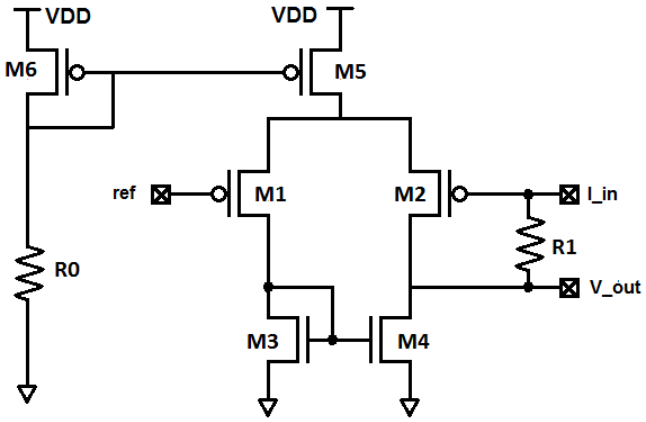

Figure 5.6: Schematic of the receive amplifier. R1 is the feedback resistor while the rest of the components make up of a single-stage opamp.

Component name	Type	Width/Length or Resistance
M1	PMOS	$240\mu m/1\mu m$
M2	PMOS	$240\mu m/1\mu m$
M3	NMOS	$40\mu m/1\mu m$
M4	NMOS	$40\mu m/1\mu m$
M5	PMOS	$40\mu m/2\mu m$
M6	PMOS	$40\mu m/2\mu m$
R0	resistor	$15k\Omega$
R1	resistor	$20k\Omega$

Table 5.1: List of components in the receive amplifier schematic.

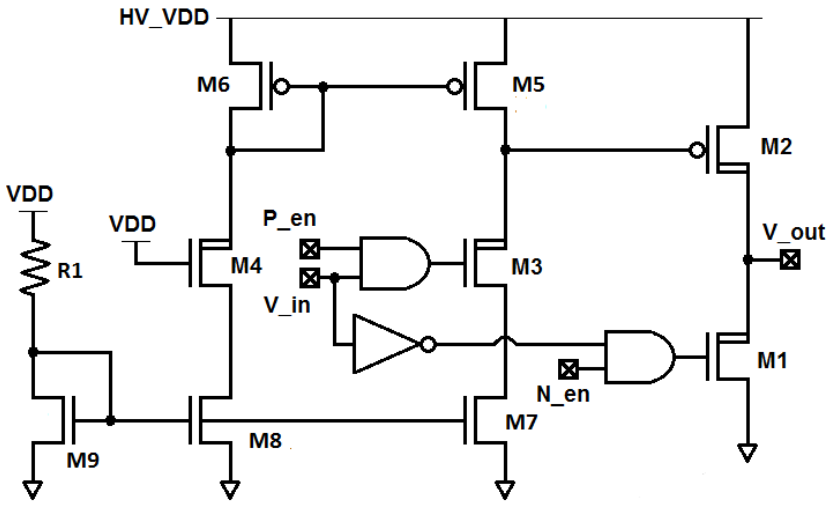

Figure 5.7: Schematic of the transmit pulser.

5.3.2 Transmit pulser

The schematic of the transmit pulser is shown in Figure 5.7. The topology chosen is similar to the one in Figure 5.4(b), where two transistors are used in the output stage, in a push-pull fashion similar to an inverter. Both transistors M1 and M2 are high-voltage transistors. The main difference between this circuit and Figure 5.4(b) is the way the gate voltage of the output PMOS (M2) is generated. Instead of using a resistor to generate the gate voltage, the drain-to-source voltage of M5 is used. Transistors M4, M6, and M8 are replica of M3, M5, and M7. The replica biasing provides the correct gate voltage to M5 and ensures that the drain voltage of M6 is close to its gate voltage. Because the gate voltage of M6 is within 5 V of the high-voltage power supply (HV_VDD), the gate of M2 is not in danger of breakdown. M3 and M4 are also high-voltage transistors because their drain-to-source voltages are a lot greater than $5V$. Ideally, M5 and M6 should also be high-voltage transistors to provide a better match to M2, but regular transistors were used instead to minimize chip area.

There are three logic gates in Figure 5.7. Their functions are to get the control signals

Component name	Type	Width/Length or Resistance
M1	NLDMOS	$168\mu m/3\mu m$
M2	PLDMOS	$815\mu m/3\mu m$
M3	NLDMOS	$48\mu m/3\mu m$
M4	NLDMOS	$48\mu m/3\mu m$
M5	PMOS	$20\mu m/1\mu m$
M6	PMOS	$10\mu m/1\mu m$
M7	NMOS	$40\mu m/2\mu m$
M8	NMOS	$20\mu m/2\mu m$
M9	NMOS	$5\mu m/2\mu m$
R1	resistor	$7.3k\Omega$

Table 5.2: List of components in the transmit pulser schematic.

to the correct polarity and provide the option to turn either M1 or M2, or both, off. NMOS transistor M1 is enabled by the N_en signal; similarly, PMOS transistor M2 can be disabled by setting the P_en signal to 0. Turning both transistors off creates a high impedance output, which is required during receive mode if the pulser output and the receive amplifier input are connected. Turning one of the two output transistors off does not seem to be too useful, but this option was added mainly for debugging and characterization purpose.

The most important components in the pulser are the two transistors in the output stage, M1 and M2. The pulser output currents, and as a result the slew rates, can be adjusted by changing the size of those two transistors. A wider transistor channel translates to a higher output current and a higher slew rate. Therefore, the sizes of both M1 and M2 need to be increased if one wants to drive a larger capacitive load. And if M2 gets larger, its gate capacitance will also go up, and the rest of the circuit, especially M3, M5, and M7, will need to be sized accordingly. The downsides for having larger transistors in the output stage are higher current consumption and a larger circuit area.

Among all the CMUTs in our lab, the low frequency 1-D array contains the largest element. Each element in that array has an estimated capacitance of $12pF$. Taking into account the parasitic capacitance and design margin, the loading specification for the pulser

was chosen to be $15pF$. As for the pulse amplitude, it was found through experiments that a pulse of $30V$ will provide sufficient pressure [13]. Furthermore, with a resonant frequency of around $6MHz$, the optimum pulse width is $83ns$, thus it was determined that each of the rise and fall times cannot be larger than $40ns$, or $30ns$ to be on the safe side. With all this information, one can calculate the slew rate and determine the required current to drive the CMUT. Using the equation

$$I = C\frac{dV}{dt} \tag{5.2}$$

where C is the load capacitance and $\frac{dV}{dt}$ is the rate of change of voltage or the slew rate, the required charging and discharging current was found to be $15mA$. The parameters of components in the pulser schematic are listed in Table 5.2.

5.4 Experimental results

Both the pulser and the amplifier are fabricated on a $3mm$ by $3mm$ test chip. The micrograph of the test chip is shown in Figure 5.8. The pulser occupies an area of $550\mu m$ by $370\mu m$. However, about 20% of the area (M4, M6, M8, M9, and R1) can be shared among pulsers when a group of pulsers are required to drive an array of CMUT elements. In addition, over half of the pulser area was occupied by the output transistors. If the circuit drives a smaller CMUT element, the chip area can be reduced. In order to provide an idea of the size of high-voltage LDMOS transistors compared to the rest of the pulser circuit, the physical design, or layout, of the pulser is shown in Figure 5.9. All the LDMOS transistors are labelled (from M1 to M4). They occupy about three quarters of the total area, while the block on the lower left corner contains all the remaining circuit elements. The receive amplifier is much smaller because it does not employ any high-voltage transistors. Its size on the test chip is $170\mu m$ by $110\mu m$.

5.4.1 Receive amplifier

The functionality of the receive amplifier was verified with a pitch-catch experiment in an oil tank using a CMUT element and an off-the-shelf ultrasonic transducer (Olympus

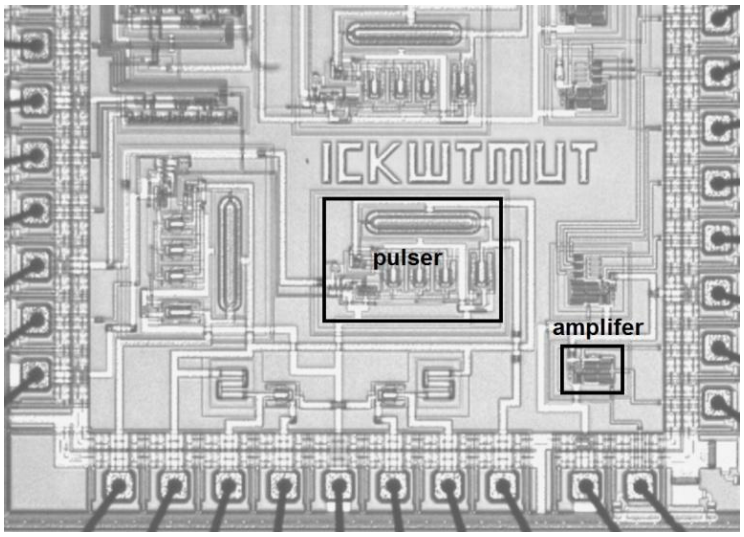

Figure 5.8: Image of the ASIC test chip.

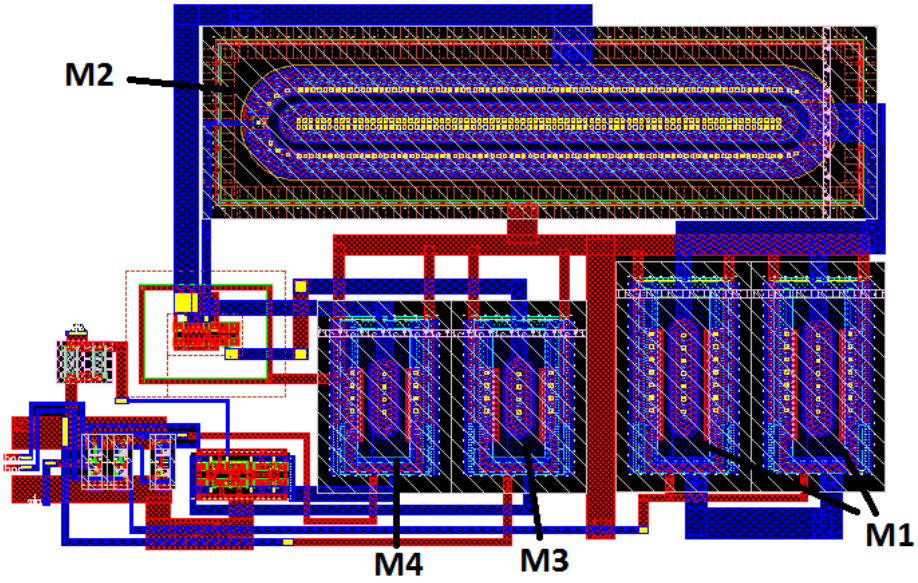

Figure 5.9: Physical design (layout) of the pulser circuit.

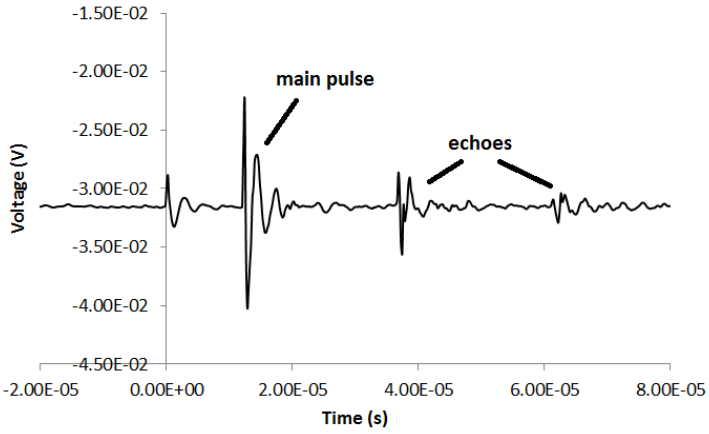

Figure 5.10: Measured receive transimpedance amplifier output of pitch-catch experiment.

Corp.). An element from a $6MHz$ 1-D CMUT array [70] was used to detect ultrasonic waves. The CMUTs were biased at $60V$. The transimpedance amplifier output is shown in Figure 5.10.

The pulse was fired at $t = 0$ and it reached the CMUTs after roughly $13\mu s$, indicating that the source was located about $2cm$ from the CMUT array. Echoes created by reflections between the CMUT and the off-the-shelf transducer can be observed at about one round trip time ($26\mu s$) and two round trip times ($52\mu s$) after the first pulse was received. The received pulse had a peak-to-peak amplitude of about $50mV$, which is quite low. Part of the reason is the mismatch between the transducer ultrasonic frequency and the resonant frequency of the CMUTs.

The performance of the receive amplifier was not characterized because the amplifier was not designed for a specific CMUT. Nevertheless, it was reported in [66] that the noise figure of the amplifier is dominated by the feedback resistor, and a well designed amplifier contributes less noise than the thermal-mechanical noise of the CMUT element, which dominates the total noise of the system. In addition, parasitic capacitance at the amplifier input, or CMUT output, can significantly increase the noise output of the system. This is why monolithic integration of CMUTs with the ASIC is preferred. And because the current experimental setup connects the CMUTs and the ASIC using wire bonding, the

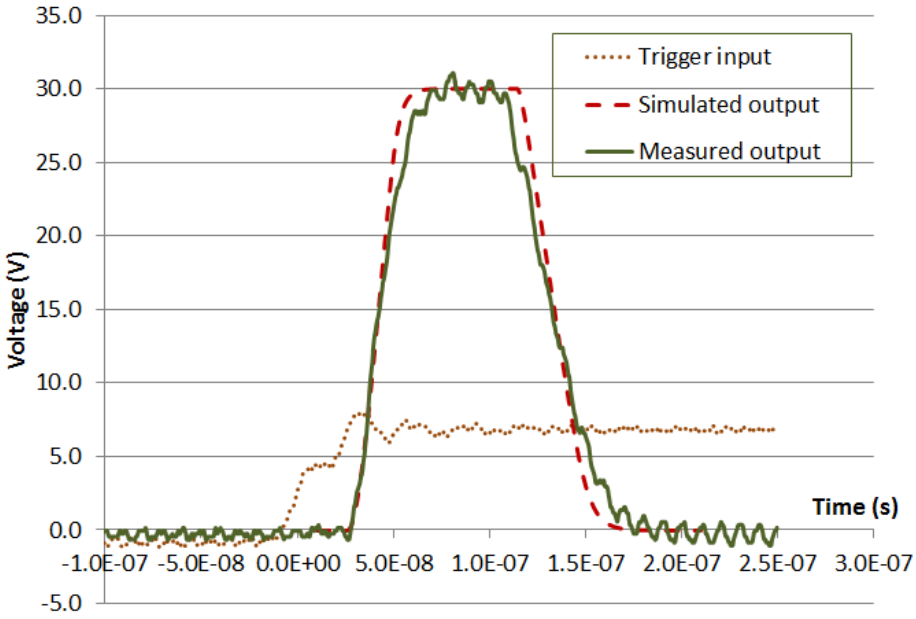

Figure 5.11: Measured and simulated pulser output when it was driving a 11pF load.

measured noise output will not be the true indicator of the amplifier noise performance.

5.4.2 Transmit pulser

Before connecting the pulser output to the CMUT, the output signal is measured using an oscilloscope. The load capacitance of the oscilloscope is $11pF$, which is comparable with the CMUT device capacitance. The waveforms captured by the oscilloscope are shown in Figure 5.11. The solid line is the measured pulser output and the dotted line is the trigger input going into the digital control circuit. The oscilloscope was triggered by the input signal at $t = 0$. The dashed line is the simulated output. It is overlaid on top of the measured output to show the accuracy of the simulation. The simulation slightly overestimates the fall time. But overall, it predicted the circuit behaviour quite accurately.

Next, another pitch-catch experiment was performed to measure the pulser. One ele-

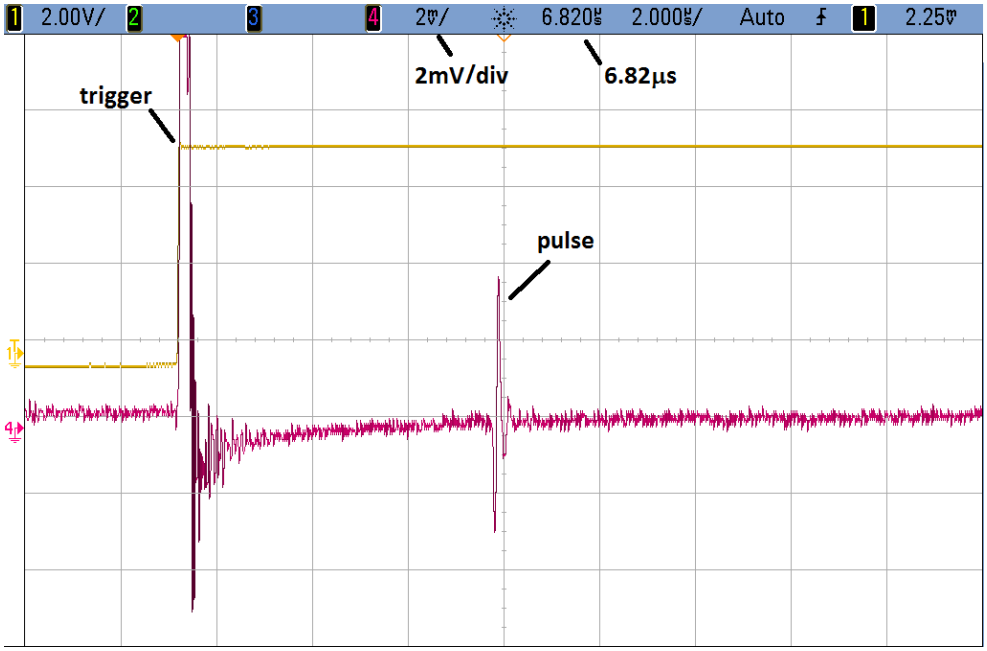

Figure 5.12: Triggering signal and hydrophone output of pulser pitch-catch experiment.

ment of a CMUT ring array was used for this measurement. The element consists of 56 CMUT cells, and has a dimension of approximately $200\mu m$ by $200\mu m$. This is the same element that was used in the modelling chapter. The optical image of the CMUT element is shown in Figure 3.6. Similar to the experiment for the reiceive amplifier, the CMUTs were immersed in vegetable oil, and a hydrophone (Onda Corp., Sunnyvale, CA) was positioned $10mm$ away.

The CMUTs were biased at $60V$, and a $30V$ unipolar pulse was applied to the CMUTs using the pulser. Using a field programmable gate array (FPGA), a Spartan-3 (Xilinx Inc., San Jose, CA), the pulse width was programmed to $80ns$. The hydrophone output on an oscilloscope screen is shown in Figure 5.12. The oscilloscope was triggered at $t = 0$, but the time axis was shifted by $6.82\mu s$ to move the received pulse to the centre of the screen. Therefore, the time of travel of the ultrasonic pulse was $6.82\mu s$, corresponding to a distance of $10mm$ using $1500m/s$ as the speed of sound.

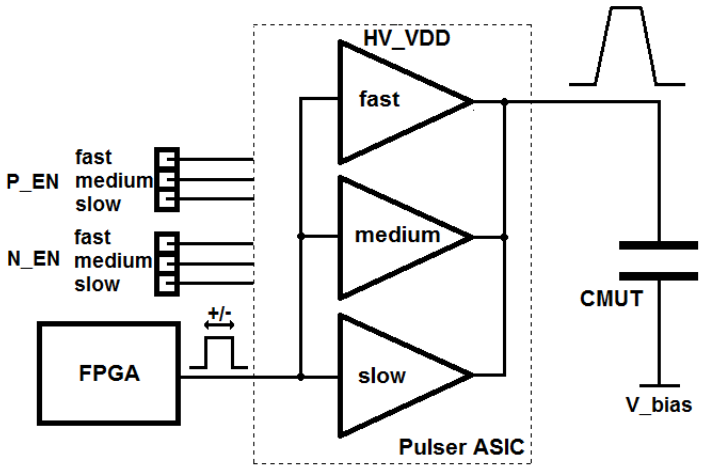

Figure 5.13: Schematic of the experimental setup for pulser characterization.

As mentioned in the previous section, the output currents (up and down currents) of the pulser is critical to the pulser performance. Therefore, for future generations of pulsers designed using the same Teledyne-DALSA process, it is important to verify the accuracy of the high-voltage LDMOS transistor models. In order to achieve that, three versions (fast, medium, and slow slew rates) of the pulser were fabricated on the same die and were connected in parallel to make the output slew rates programmable. Two three-bit digital signals were used to control the slew rates of the rising (P_EN) and falling (N_EN) edges, and this is why the option was implemented to turn off either PMOS or NMOS in the output stage, as mentioned in the previous section. The experimental setup for the pulser characterization is illustrated in Figure 5.13.

The pulser outputs with only one of the three pulsers activated are plotted in Figure 5.14. Because each slew rate was controlled by a 3-bit signal, the three cases (fast, medium, and slow) correspond to control signals of 100, 010, and 001 respectively. The pulse amplitude was set to $25V$, and the input pulse was made longer (close to $60\mu s$) so that all three rising edges can get to the maximum voltage before the falling edges were triggered. The pulsers were connected to the CMUT element (Figure 3.6), which along with parasitic capacitance of the PCB and cable connections, provided an estimated capacitive load of

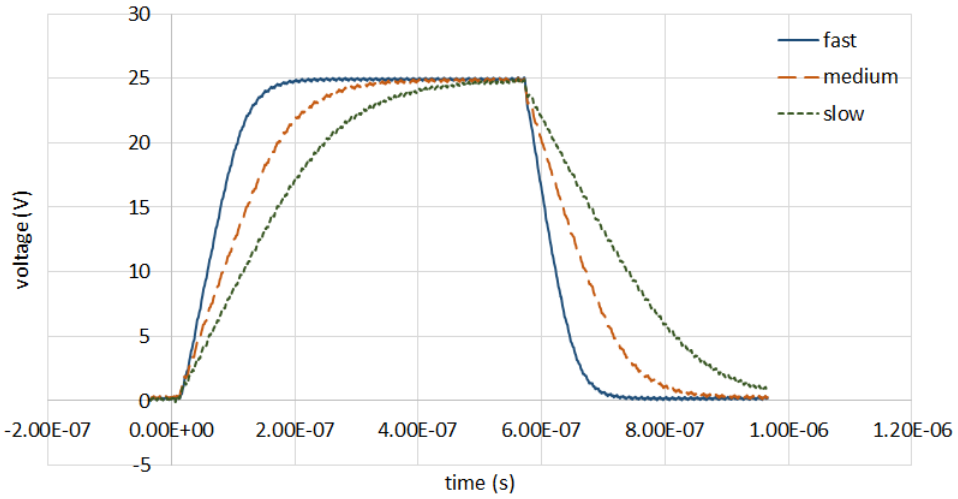

Figure 5.14: Measured pulser output for different speed settings.

$40pF$.

From Figure 5.14, it can be observed that the slope of the edges decreases as the pulser outputs get closer to the final voltage. This is because the MOS transistors in the pulser output stage got out of saturation as the drain-source voltage decreased, resulting in a small output current. Nevertheless, since the goal of this experiment is to characterize the maximum current that a transistor can provide, the slew rates are calculated from the initial segments of the rising and falling edges.

The characterization results, as well as the predicted transistor output currents from the model, are summarized in Tables 5.3 and 5.4, for the rising edges and falling edges respectively. Because the PMOS transistors supply current to the output load, the PMOS output current can be characterized from the rising edge data. Similarly, the falling edge data will be used to characterize the NMOS transistors. The falling edge results presented in Table 5.4 show an excellent match between the measured and modelled current. That means that the NMOS transistors worked exactly as the model predicted. The PMOS results look a bit problematic because the model seemed to overestimate the current in most cases. However, when one looks at the pulser schematic (Figure 5.7), it is not entirely

	Rising edge		
Setting	Measured slew rate($V/\mu s$)	Corresponding current(mA)	Modelled current(mA)
001	232	9.3	5.5
010	345	13.8	16.5
011	577	23.1	22.0
100	650	26.0	31.0
101	882	35.3	36.5
110	995	39.8	53
111	1227	49.1	58.5

Table 5.3: Comparing the measured and modelled PMOS output current that corresponds to the rising edge of pulser output.

unexpected because the PMOS gate voltage was provided from the replica biasing circuit, while the NMOS gate voltage was fixed at $5V$ when it was turned on. The dependence of PMOS gate voltage on the biasing circuit means that any variation on the biasing, especially the current that was set by R1, could affect the output current. In the future, a specially designed circuit will be needed to accurately characterize the PMOS transistors. Nevertheless, the NMOS results prove that the model from the foundry is quite accurate.

Lastly, because the pulser characterization setup was already available, it would be helpful to use the pulse width control function to measure the effect of pulse width on CMUT output pressure. The pulse width was adjusted through the FPGA, in steps of $10ns$, and the hydrophone output amplitudes under different pulse width were recorded and shown in Figure 5.15. It was found that there was indeed an optimum pulse width for maximum output pressure, and it was $60ns$. The measured value was slightly less than the theoretical value, which is half of a period of the resonant frequency ($83ns$), given that the resonant frequency is close to $6MHz$. This discrepancy is mainly due to the finite output slew rates of the pulser, which essentially increased the pulse width because of the non-zero rise and fall times.

	Falling edge		
Setting	Measured slew rate($V/\mu s$)	Corresponding current(mA)	Modelled current(mA)
001	212	8.5	8.3
010	375	15.0	14.4
011	587	23.5	22.7
100	725	29.0	28.8
101	937	37.5	37.1
110	1100	44.0	43.2
111	1312	52.5	51.5

Table 5.4: Comparing the measured and modelled NMOS output current that corresponds to the falling edge of pulser output.

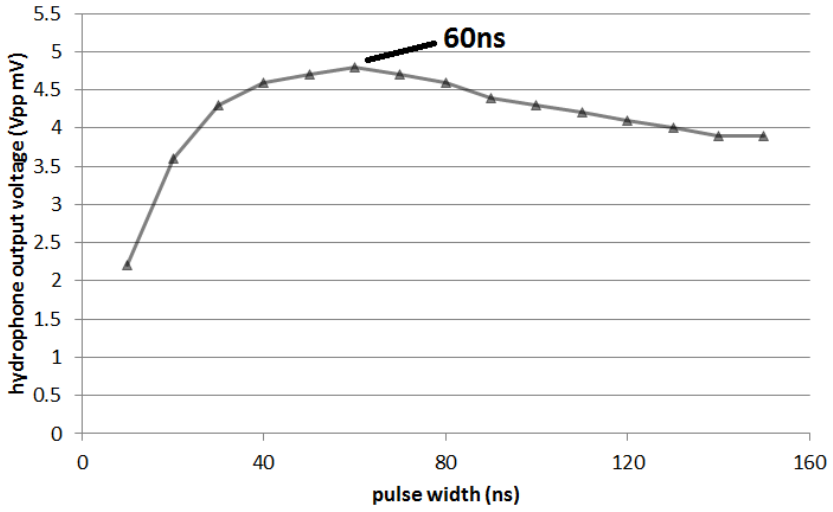

Figure 5.15: Variation of measured output pressure (hydrophone output) amplitude against the width of the input pulse.

5.5 Discussion

An ASIC for CMUTs, including a transmit pulser and a receive amplifier, was demonstrated in this chapter. Even though the actual integration has not been done (the ASIC and the CMUTs were connected through a PCB in the presented system), the ground work for CMUTs ASIC integration in the future has been laid.

To go one step further, it might be beneficial to integrate part of the back-end circuit, for example the analog-to-digital converters and the beam-formers, with the CMUTs and the ASIC to form a system-in-a-package. Such an highly integrated system may not be necessary for medical ultrasound, but it would certainly be helpful in structural health monitoring (SHM) applications, where the ultrasonic transducer systems are attached to structures permanently. The processed digital signals from the transducer system can be transmitted wirelessly, thus forming a SHM wireless sensor network. In fact, we have demonstrated the implementation of transmit and receive beam-forming and some basic signal processing in an FPGA [71]. The simplicity of the digital circuit in that system [71] means that it will be entirely possible to integrate the digital function with the ASIC.

The circuits presented in this chapter were not optimized for any specific CMUT design, because the original intent was to design an ASIC that would work for CMUTs of different resonant frequencies and sizes. In the future, if an ASIC is designed for a specific CMUT array, the ASIC can be optimized and the circuit area can be reduced. The performance of both the receive amplifier and the transmit pulser should be characterized. Noise equivalent pressure (NEP) should be found for the receiver system, and the pressure output per volts of driving signal could be a good indicator of the transmit system performance. Another point related to the circuit area is that the Teledyna-DALSA $0.8\mu m$ process was chosen because it was available to us, with a discounted price, through CMC Microsystems. Fabricating the ASIC in another technology such as a $0.18\mu m$ CMOS process (offered by both ams and TSMC) will significantly reduce the size of the circuit.

Chapter 6

Air-coupled CMUTs

Ultrasonic NDT is typically done with a transducer making direct contact with the test object or through a liquid coupling medium. However, in some applications where test objects cannot make contact with transducers or coupling agents for fear of contamination or breakage, coupling ultrasound through air is required [72]. Because of the large mismatch in acoustic impedance between air and solids, air-coupled ultrasound can only be used a limited number of applications. One of the main applications of air-coupled ultrasound in NDT is the determination of material thickness using the through transmission technique [15]. In addition, material characterization and inspection of paper and wood using air-coupled ultrasound were also reported. Another example of air-coupled ultrasound application is the evaluation of food materials, such as cheese and chocolate, as reported by [73].

Generating ultrasound in air using piezoelectric transducers is difficult because the acoustic impedance of air ($400 kg/m^2 s$ at $0°C$) is much smaller than that of piezoelectric materials (about $30 \times 10^6 kg/m^2 s$) [42]. Just like electrical impedance, maximum transfer of power occurs when the acoustic impedance of the source matches that of the load. A large impedance mismatch results in a big loss, thus inefficient coupling. An impedance matching layer can be used to improve the energy transfer, but because of the large impedance mismatch, implementing a matching layer that can provide a wide enough bandwidth and is thin enough for high frequency operation has been difficult [42].

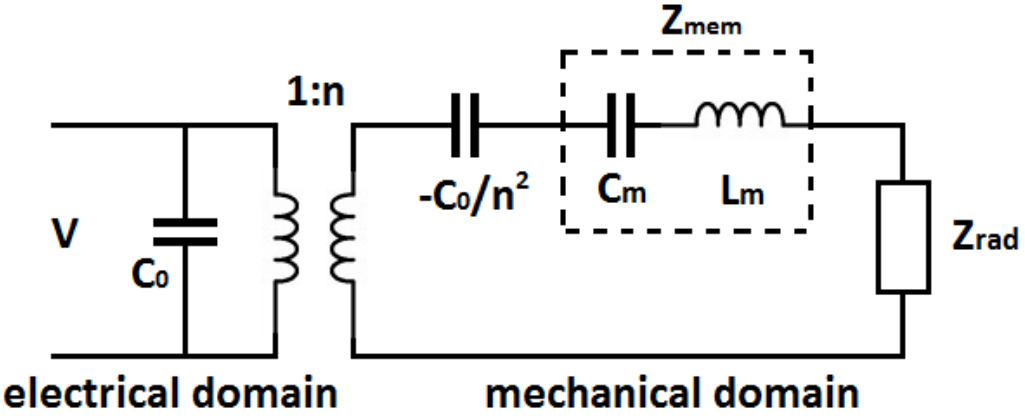

Figure 6.1: Equivalent circuit model of an electroacoustic transducer, showing only the mechanical domain.

CMUTs, on the other hand, are better at generating sound in air. For CMUTs, because ultrasound is generated by the vibrating of thin membranes, the coupling mechanism of sound into the medium is different. Considering Mason's model for an electroacoustic transducer [74] as shown in Figure 6.1, with a negative capacitive to model the spring softening effect as proposed by Hunt [75], the output pressure can be seen as the voltage drop across the radiation impedance of the medium, Z_{rad}. Z_{mem} is the mechanical impedance of the membrane. At the resonant frequency, the equivalent impedance of the inductor and the two capacitors on the mechanical domain becomes zero, thus all the voltage from the transformer gets to Z_{rad}, resulting in maximum output power. Because the acoustic impedance for air is so low ($Z_{rad} = 400kg/m^2s\times$area of membrane), a slight change in frequency will cause the membrane mechanical impedance to increase above Z_{rad}, reducing the output pressure. This is why CMUTs have a small bandwidth in air. On the other hand, if the acoustic impedance of the medium is high (for example, $1.5\times10^6kg/m^2s$ for water), the membrane mechanical impedance can be kept below Z_{rad} for a wide range of frequency, resulting in a larger bandwidth.

6.1 Background

Coupling ultrasound through air was the reason that motivated researchers to invent CMUTs, when researchers at Stanford University wanted to detect cracks in the wings of fighter jets [16]. In 1997, the same group from Stanford University demonstrated air-coupled transmission of ultrasonic waves through an aluminum plate [15]. Ultrasonic waves usually cannot get through a piece of metal, but if the thickness of the metal plate is a multiple of half of the wavelength of the ultrasonic waves, standing waves can develop inside the metal and sound waves can indeed get through.

CMUT research took off shortly after researchers realized that CMUTs, when immersed, have exceptionally large (greater than 100% of centre frequency) bandwidths. From that point on, air-coupled CMUTs have not been the focus of many research groups. However, several papers on air-coupled CMUTs can still be found in the literature. For example, the radiated fields of air-coupled CMUTs were modelled, and the CMUTs were used to scan the surface of a coin, with the help of a translation stage, in [76]. Researchers from General Electric also reported a CMUT-based air-coupled transducer for NDT [77]. Their CMUTs were shown to have a higher transduction efficiency than commercial piezoelectric transducers. They observed a transmission loop gain, which is the ratio of receiver output and transmitter input, of $-51dB$ in their setup when the transmitter and receiver are positioned $25mm$ apart. A low frequency CMUT that generated sound at $50kHz$ was demonstrated in [78]. More recently, air-coupled CMUTs that were designed for chemical and pressure sensing in harsh environments were reported in [79][80]. Their CMUTs have resonant frequencies in the range of $100kHz$ to $400kHz$ depending on the air pressure, which can vary from 1 to 20 atm. Other implementations of air-coupled CMUTs include an air-coupled CMUT based on a tethered front-plate electrode [81], and a CMUT array designed for vehicle collision avoidance applications [82]. Another technology that is worth mentioning is MEMS ultrasonic microphones [83]. Despite being able to only receive ultrasound, some of them operate using the same theory as CMUTs.

Based on the number of publications on air-coupled CMUTs, there is no question that CMUTs are capable of generating ultrasound in air. However, since the fabrication of CMUTs generally requires fully custom processes, fabricating CMUTs using a standard

multi-user MEMS process, which is not optimized for CMUTs, would provide further proof on efficiency of CMUTs in generating ultrasound in air. Using standard processes to fabricate CMUTs also provide other advantages such as low cost and more reliable devices because standard processes are well established.

All standard MEMS processes that are capable of implementing CMUTs are based on surface micromachining, which requires a sacrificial release step to free up the membrane. Because there must be holes to allow etchant to reach the sacrificial layer, an extra processing step to seal the etch holes is needed if the CMUTs are to be used in immersion. Therefore, the simplest CMUTs that can be made using standard MEMS processes are air-coupled CMUTs.

There have been several attempts in using a standard process to fabricate CMUTs. The design and characterization of air-coupled CMUTs based on PolyMUMPs, a multi-user MEMS process that uses polysilicon as the structural layer material, was reported in [23], but no acoustic measurement results were presented in the work. CMUTs fabricated with PolyMUMPs were also reported in [84]. The devices were bonded to a test object and were used as detector for acoustic emissions, which occur when flaws are presented in structures that are under stress. In [85], immersion testing with PolyMUMPs CMUTs was successfully demonstrated when ultrasound gel was used to couple acoustic waves into a water tank.

6.2 Modelling of the basic structure (a fixed-fixed beam)

For CMUTs that are designed to work in immersion, the membranes need to be fixed on all sides to prevent the coupling medium from getting into the cavity. However, for air-coupled CMUTs, that requirement can be lifted. In order to generate maximum pressure, the volume displaced by the membrane during vibration should be as large as possible. For a rectangular membrane, that condition is achieved when only two opposite sides of the membrane are fixed, and the other two sides are free. A comparison between having two sides and all four sides fixed was presented in [23], and it was proved by simulations that more ultrasonic energy would be emitted when only two opposite sides were fixed.

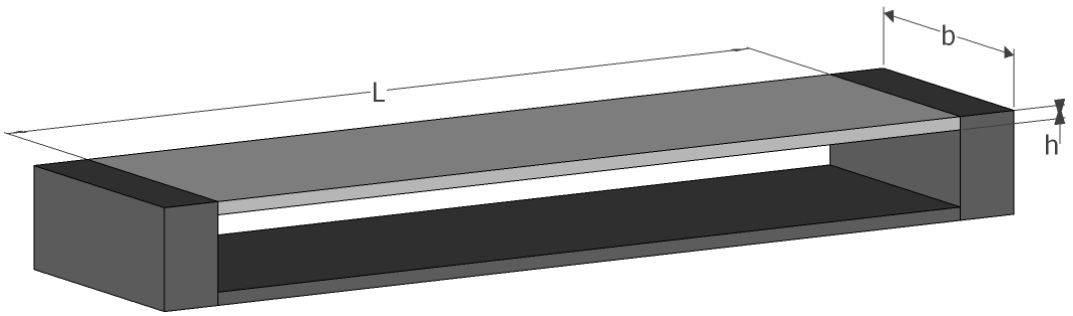

Figure 6.2: A fixed-fixed beam that is used to model an air-coupled CMUT.

This structure essentially becomes a fixed-fixed beam, as illustrated in Figure 6.2, and the length, width, and thickness of the beam are denoted by L, b, and h respectively.

The static deflection of an electrically actuated fixed-fixed beam can be described using the following equation found in [86]:

$$\hat{E}I\frac{d^4w}{dx^4} - N\frac{d^2w}{dx^2} - \frac{\hat{E}A}{2L}\frac{d^2w}{dx^2}\int_0^L \left(\frac{dw}{dx}\right)^2 dx = q(x) \tag{6.1}$$

where $w(x)$ is the beam displacement in the transverse direction, $q(x)$ is the distributed load per unit length, L, N, and I are the length, the axial load and the second moment of area of the beam respectively. The axial load arises from the residual stress and is proportional to the cross-sectional area of the beam. If the width of the beam is large compared to its length ($L \leq W$), the effective Youngs modulus is $\hat{E} = E/(1-v^2)$ where E is the Youngs modulus and v is the Poisson's ratio of the material [87]. For a narrow beam ($L \geq 10W$), the effective Young's modulus is equal to the material's Young's modulus. If the beam width falls in between the two extremes, a linear interpolation can be done to estimate the effective Young's modulus[1].

The non-linear term in equation (6.1) is the contribution from mid-plane stretching, which is caused by the lengthening of the beam when it deflects. Mid-plane stretching

[1]Email communication with Prof. Eihab Abdel-Rahman.

increases the resonant frequency of the beam because of the increase in axial tension [86]. However, in most multi-user MEMS processes, the gap height, defined by the sacrificial layer thickness, is not much larger than the beam thickness. For example, in PolyMUMPs, the first sacrificial layer thickness is $2\mu m$ and the polysilicon layer is also $2\mu m$ thick. Therefore, the mid-plane stretching term can be removed as suggested by Lee [88], who reasoned that the non-linear term can be neglected when the gap to beam thickness ratio is much less than five. Equation (6.1) can be rewritten as

$$\hat{E}I\frac{d^4w}{dx^4} - N\frac{d^2w}{dx^2} = q(x) \tag{6.2}$$

with the following boundary conditions

$$w(0) = 0 \quad w(L) = (0) \qquad \frac{dw}{dx}\,|_{x=0} = 0 \quad \frac{dw}{dx}\,|_{x=L} = 0 \tag{6.3}$$

If equation (6.2) is integrated to get the form $kw = F$, the spring constant, k, can be found using the mode shape of the beam, as presented in [88].

$$k = \frac{1024}{5}\frac{\hat{E}I}{L^3} + \frac{512}{105}\frac{N}{L} \tag{6.4}$$

The fundamental resonant frequency of the beam is $f_0 = \frac{1}{2\pi}\sqrt{\frac{k}{m}}$, where the effective mass, m, of the beam can be estimated as $m = 128\rho bhL/315$ [89], and ρ is the density of the beam material. Therefore, the resonant frequency is

$$f_0 = \frac{1}{2\pi}\sqrt{\frac{315}{128\rho bhL}\left[\frac{1024}{5}\frac{\hat{E}I}{L^3} + \frac{512}{105}\frac{N}{L}\right]} \tag{6.5}$$

Two observations can be made from equation (6.5). First, a tensile axial stress ($N > 0$) increases the resonant frequency by making the beam stiffer. Secondly, the resonant frequency, to the first order, is independent of the width of the beam because the second moment of area (I) and the axial load (N) are directly proportional to the width.

The derivation of the resonant frequency so far did not take into account the bias voltage, which reduces the resonant frequency because of the spring softening effect. Consider

the pull-in voltage of a fixed-fixed beam given by [88]:

$$V_{pi} \cong 0.6036\sqrt{\frac{k{h_0}^3}{\varepsilon A}} \tag{6.6}$$

where h_0 and A are the unactuated height and the area of the beam, respectively. Recall the softened spring constant given in (3.14):

$$k_{soft} = k - \frac{\varepsilon S V^2}{d^3} \tag{6.7}$$

If the bias voltage is set at 80% of the pull-in voltage, which is a typical bias voltage choice for CMUTs, then by substituting $0.8V_{pi}$ into (6.7) and assuming that the beam area A is equivalent to the piston area S, k_{soft} can be calculated to be $0.767k$, and the resonant frequency is decreased by 12.4%.

The beam thickness, h, is determined by the process and there is nothing that a user of a standard process can do except choosing a different structural layer, if available. The length, L, is chosen according to the desired resonant frequency. The only dimensional parameter left, then, is the width, b. As it turns out, the beam width affects mainly the torsional vibration frequency. Torsional vibration of a fixed-fixed beam means that one free side of the beam goes up while the other free side goes down, as opposed to lateral vibration where both free sides go up and down together. For a well designed beam, the fundamental vibrational mode is lateral because the impulse response of the beam should mainly consist of lateral vibration. Figure 6.3 shows the two vibrational mode shapes of a fixed-fixed beam.

The torsional equation of motion of a fixed-fixed beam with axial load is given in [90]:

$$\rho J \frac{d^2\tau}{dt^2} - (Gk_t + N\zeta)\frac{d^2\tau}{dx^2} = 0 \tag{6.8}$$

Where τ is torsional displacement; $J = hb(h2+b2)/12$ is the polar second moment of area; $G = E/2(1+v)$ is the shear modulus of the beam, $\zeta = (h^2+b^2)/8$, and k_t is the torsional stiffness coefficient [91], which can be estimated as

$$k_t = bh^3\left[\frac{1}{3} - 0.21\frac{h}{b}\left(1 - \frac{h^4}{12b^4}\right)\right] \tag{6.9}$$

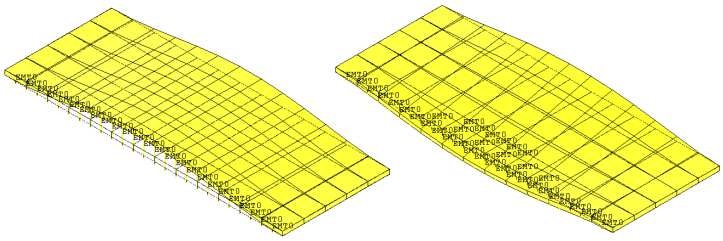

Figure 6.3: Lateral (left) and torsional (right) vibration mode shapes of a fixed-fixed beam.

Solving equation (6.8) with the boundary conditions of a fixed-fixed beam will lead to the torsional resonant frequency f_t [90]:

$$f_t = \frac{1}{2L}\sqrt{\frac{Gk_t}{\rho J}\left(1 + \frac{N\zeta}{Gk_t}\right)} \tag{6.10}$$

The width of the beam should be picked such that the torsional resonant frequency is not an integer multiple of the fundamental lateral resonant frequency, in order to avoid any coupling of energy to the second mode. However, spring softening is not taken into account in (6.10). An analytical expression for such a case is not available, thus numerical modelling will be used to find the torsional vibration frequency when a bias voltage is applied. Nevertheless, for initial design purpose, the torsional vibration frequency can be compared with the unactuated lateral vibration frequency, assuming that spring softening will cause both to decease by a similar percentage.

6.3 Fabrication process

The first step of the design procedure is to pick a suitable fabrication process. As mentioned above, several designs used the PolyMUMPs (MEMSCAP Inc., Durham, North Carolina) process [23][84][85]. However, the residual stress on the structural polysilicon layers makes PolyMUMPs a poor choice for air-coupled CMUTs. Because of temperature difference in the processing steps, the structural layers in PolyMUMPs tend to expand after release, creating a compressive residual stress, which has a published value of $10MPa$. This stress

is not a problem when the beam is short, but it could be problematic for longer beams. For air-coupled CMUTs, the target operating frequency is less than $1MHz$ because of the increased attenuation of high frequency sound waves in air. As a result, the corresponding fixed-fixed beams will be long ($> 100\mu m$). Buckling could occur if beams with compressive stress are too long. And even if the beam does not buckle, the compressive stress will affect the CMUT output power and sensitivity (just imagine a guitar string without tension). Therefore, another process that provides a structural layer with tensile stress is required.

The process that was chosen for air-coupled CMUTs fabrication is UW-MEMS. It was developed by the Center of Integrated RF Engineering (CIRFE) at the University of Waterloo, and it is the same process as the one used in [92] and [93]. The target application of this MEMS process is RF switches. This surface micromachining process started with an alumina substrate and used chromium as a high resistance routing layer. A first dielectric layer (silicon oxide) was deposited on top of the chromium layer. Both the chromium layer and the silicon oxide layer were not used in the air-coupled CMUTs design. Gold was used as the structural layer material. Each gold layer consisted of a sputtered gold seed layer and an electroplated gold layer. Only two gold layers were present, and the thicknesses of the top and bottom layers were $1.25\mu m$ and $1\mu m$ respectively. The two gold layers were separated by a $0.5\mu m$ dielectric layer (silicon oxide), which was deposited on top of the bottom gold layer, and a $2.5\mu m$ sacrificial layer (polyimide), which was spin coated on top of the dielectric layer. The structure was released by removing the sacrificial layer using an oxygen plasma dry etch process. Table 6.1 summaries the material and thickness of different layers in the process. A detailed description of the process can be found in [93].

The functions of different layers are also listed in Table 6.1. The two gold layers form the top and bottom electrodes of the CMUT. The movable top layer also serves as the CMUT membrane. The dielectric layer prevents the two electrodes from shorting in the event that the membrane collapses. The chromium layer is not used because high resistance routing is not required for CMUTs. Figure 6.4 shows the top view and cross-sectional view of a CMUT cell that was designed with this process. Etch holes on the top layer are visible from the top view. They are required if the width of the beam is greater than $30\mu m$. The anchor layer is not a material layer; it serves as the mask of a processing step that etches away the sacrificial layer, thereby allowing the top gold layer to make contact with

Layer number	Material	Thickness (μm)	Remark
1	Chromium	0.04	Not used
2	Silicon oxide	0.3	Not used
3	Gold	1	Bottom electrode
4	Silicon oxide	0.5	Insulating layer
5	Polyimide	2.5	Sacrificial layer
6	Gold	1.25	Top electrode

Table 6.1: Material, thickness, and function of different layers in the UW-MEMS proces.

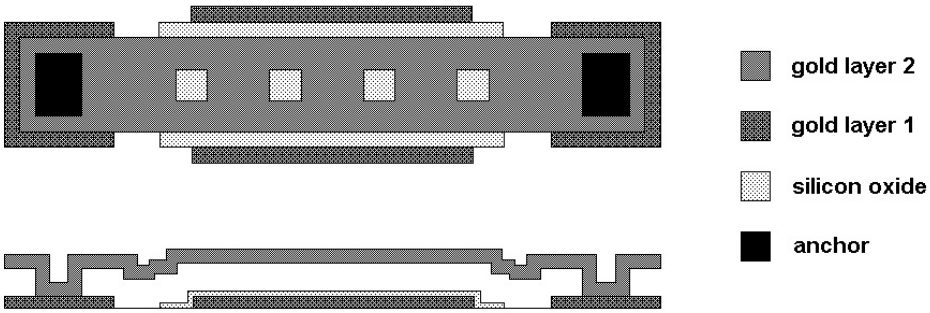

Figure 6.4: Top view and cross-sectional view of a CMUT cell design based on the UW-MEMS process.

the bottom layer. Only one CMUT cell is shown in figure 6.4; however, in a transducer element, tens or hundreds of CMUT cells are connected in parallel to generate sufficient pressure.

6.4 CMUTs Design

The CMUT design process begins with the selection of a suitable ultrasound frequency. Typically, the ultrasound frequency is chosen based on the application. Sound with higher frequency travels for a shorter distance but provides a better resolution. For air-coupled CMUTs, because the acoustic attenuation constant of air increases with the square of the

frequency [94], the CMUT output frequency should be kept low (below $1MHz$, which is the limit of most air-coupled ultrasonic systems [95]). In addition, the resonant frequency of the beam is limited by the fabrication process and the required bias voltage. A shorter beam has a higher resonant frequency but it also requires a higher voltage to get it to deflect by the same amount. Because the existing power supplies in our lab can only provide a voltage of up to $200V$, the bias voltage of this design is limited to below $200V$.

Table 6.2 lists the mechanical properties of the membrane material (gold) that were used for the chosen process. Using equation (6.5) along with the mechanical properties of gold and a default thickness of $1.25\mu m$, we can find the unactuated fundamental resonant frequencies for beams of different lengths. It is tempting to use the residual stress value in Table 6.2 for the calculation of the axial load. Residual stress arises when a material was deposited at a higher temperature, cooling it down to room temperature will cause the material to shrink or expand. In this case, the gold layer shrinks by the ratio of $E\sigma_r$, creating a tensile stress. For a fixed-fixed beam, however, not only does the beam material develop strain, so does the substrate. In fact, the alumina substrate also shrinks when it is cooled down from a higher temperature, effectively reducing the stress of the gold layer. The material properties of the substrate is not provided in the process user guide; however, they can be found from the literature [96][97]. A thermal expansion coefficient of $8\times10^{-6}/K$ is assumed for alumina. Using a thermal expansion coefficient of $14\times10^{-6}/K$ for gold, the strain, as well as the stress, on the beam is effectively reduced by 8/14. Therefore, an axial load of $81MPa\times b\times h$ was used for calculation.

The resonant frequencies calculated from the analytical model (equation (6.5)) are plotted in Figure 6.5. From the plot, one can pick the beam length based on the ultrasound frequency requirement. For example, if a resonant frequency between $200kHz$ and $250kHz$ is required, one can pick a length of $160\mu m$, which results in an unactuated resonant frequency of $248kHz$, and $217kHz$ with a voltage bias at 80% of the pull-in voltage. With a width of $45\mu m$, the calculated torsional vibration frequency is $322kHz$, or 1.3 times the unactuated fundamental resonant frequency and 1.5 times the fundamental resonant frequency with a bias voltage. However, to achieve more accurate results, one needs to turn to another modelling method.

Besides analytical modelling, the design was simulated in ANSYS (ANSYS Inc, Canons-

Property	Symbol	Value	Unit
Young's modulus	E	79	GPa
Poisson's ratio	v	0.44	
Density	ρ	19300	kg/m^3
Residual stress	σ_r	190±30%	MPa

Table 6.2: Mechanical properties of the air-coupled CMUT membrane material.

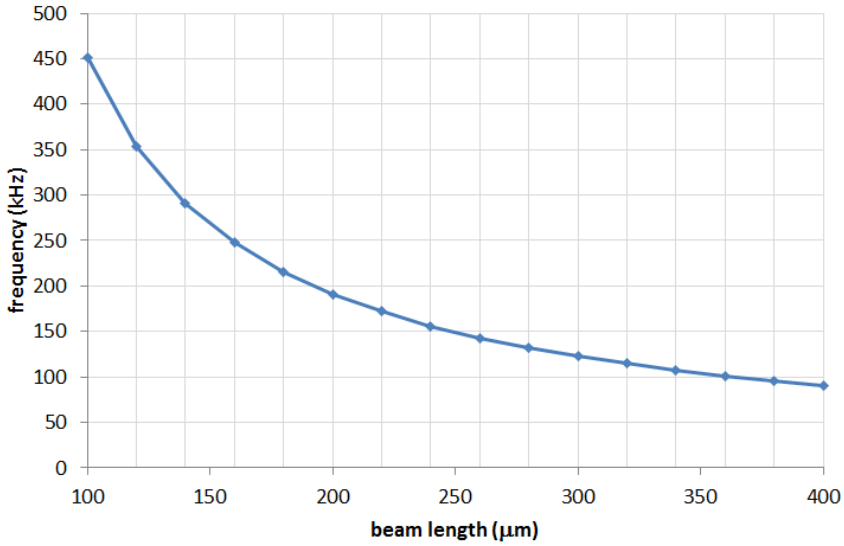

Figure 6.5: Calculated fundamental resonant frequency versus the length of the beam.

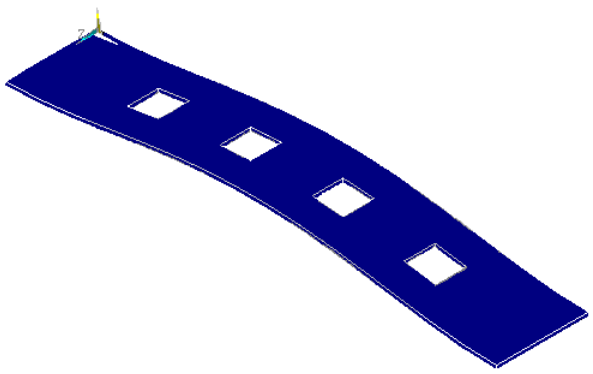

Figure 6.6: ANSYS 3-D plot showing the fundamental mode shape of a fixed-fixed beam with etch holes.

burg, PA), a finite element method (FEM) based software. The structure that was used for simulations was primarily a fixed-fixed beam, except that etch holes were added to the model to more closely match the actual device. A 3-D model was constructed using SOLID186 elements to model the gold membrane. The effect of the electrostatic force on the beam was modelled by TRANS126 elements. The tensile residual stress is applied to the membrane using a thermal expansion coefficient and a negative temperature change. Both static and modal analyses were run. Figure 6.6 is a 3-D plot showing the modelled structure in its fundamental mode shape.

Static analyses for the CMUT under different bias voltages were run, and the resulting fundamental frequency and deflection at the centre of the beam were plotted against the voltage, as shown in Figures 6.7(a) and (b), respectively. The pull-in voltage was found to be around $170V$. Therefore, $136V$ (80% of the pull-in voltage) is chosen as the bias voltage of the CMUT in subsequent simulations. The comparison of analytical and numerical modelling results is summarized in Table 6.3. The analytical modelling results are all within 5% of the FEM results; this is expected because the analytical results are basically simple approximations of the FEM results. However, the comparison highlights the fact that the actual geometry that includes etch holes can be approximated by a uniform or prismatic beam.

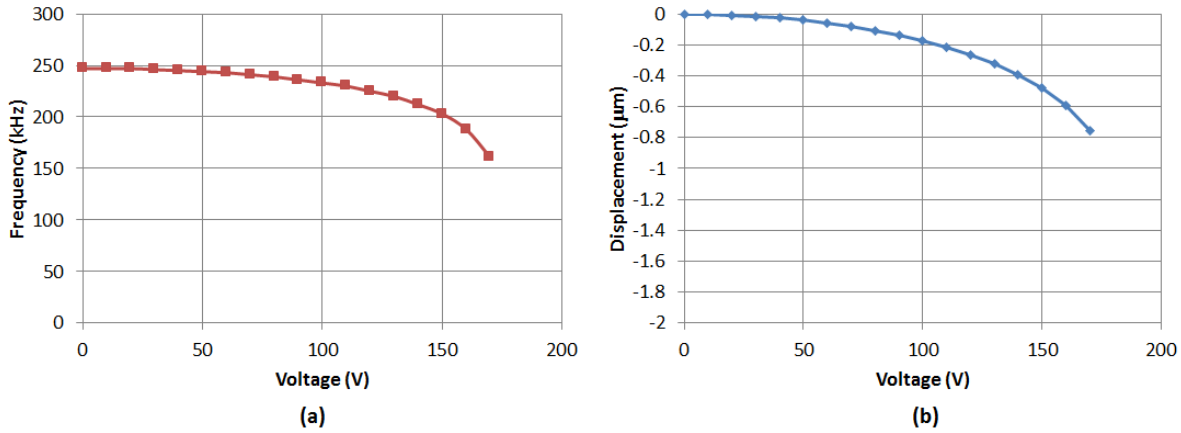

Figure 6.7: Simulated (a) fundamental resonant frequency and (b) maximum deflection of a $160\mu m \times 45\mu m$ fixed-fixed beam vs bias voltage.

Resonant	Analytical		FEM	
frequency	V = 0	V = 80% pull-in	V = 0	V = 136
Lateral	$248kHz$	$217kHz$	$247kHz$	$216kHz$
Torsional	$322kHz$	N/A	$332kHz$	$309kHz$

Table 6.3: Analytical modelling and FEM results of a $160\mu m \times 45\mu m$ fixed-fixed beam.

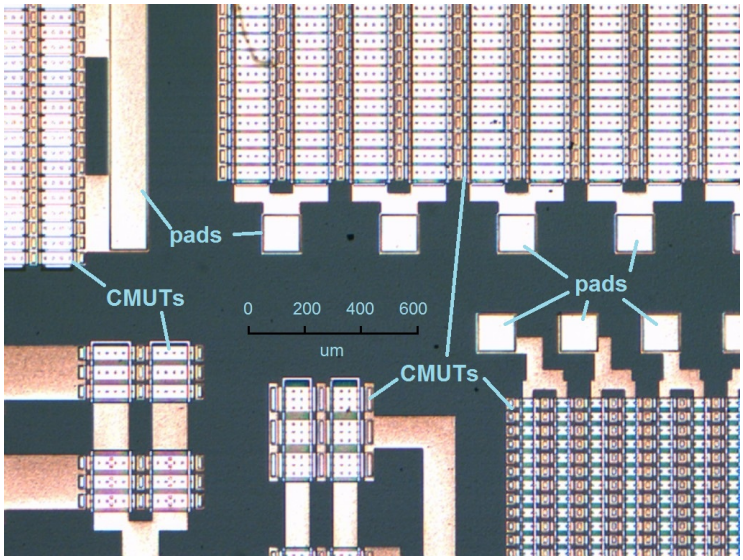

Figure 6.8: A micrograph of part of the first generation air-coupled CMUTs test chip.

6.5 First generation devices

CMUTs designed using the steps outlined in the previous section were fabricated on a test chip. The test chip contains test structures and arrays of parallelly connected CMUTs. A micrograph of the test chip is shown in Figure 6.8.

6.5.1 Characterization

The $160\mu m \times 45\mu m$ CMUTs were first tested using a laser vibrometer. A vibrometer works by shining a laser beam onto the vibrating surface, and the vibration frequency and amplitude are measured based on the Doppler shift of the reflected laser. The vibrometer used is a Polytec OFV-5000 with a VD-02 velocity decoder that has a $1.5MHz$ bandwidth.

The first step was to determine the device pull-in voltage so that a correct bias voltage can be applied. A small ($1V_{pp}$) sinusoid signal was applied to one terminal of the CMUT, while DC voltage supply was connected to the other terminal, providing a bias voltage.

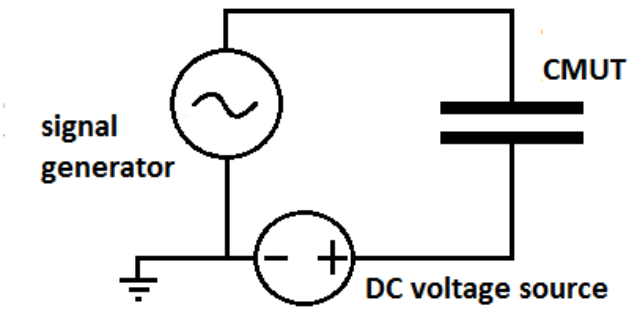

Figure 6.9: Experimental setup for vibrometer measurement.

The experimental setup is illustrated in Figure 6.9. The sinusoid signal causes the CMUT to vibrate at the signal frequency, and the vibration can be monitored by the vibrometer as a velocity. As one increases the bias voltage, the velocity at the centre of the beam goes up and the vibrational frequency goes down because of the spring softening effect. But when pull-in occurs, the resonant frequency changes, and the vibration at the signal frequency becomes very small or disappears. A pull-in voltage of $90V$ was found for a $160\mu m \times 45\mu m$ CMUT using this method.

Next, the CMUT was biased at $70V$, about 80% of the pull-in voltage. The velocity was then measured under different frequencies of excitation. The frequency sweep was done from $150kHz$ to $230kHz$, as shown in Figure 6.10, and the resonant frequency of the device was found to be $185kHz$, where the peak is located. The full width at half maximum (FWHM) bandwidth in this case is about $30kHz$, thus the fractional bandwidth is 16%. The FEM simulation results are compared with the measurement results in Table 6.4. FEM predicted a higher pull-in voltage and a higher resonant frequency than the experimental results. Assuming that the device dimensions and the material properties are accurate, this discrepancy indicates that the residual stress was over-estimated in the FEM. This over-estimation is understandable because the residual stress as quoted by the foundry has a tolerance of $\pm 30\%$, as indicated in Table 6.2. In addition, the thermal expansion

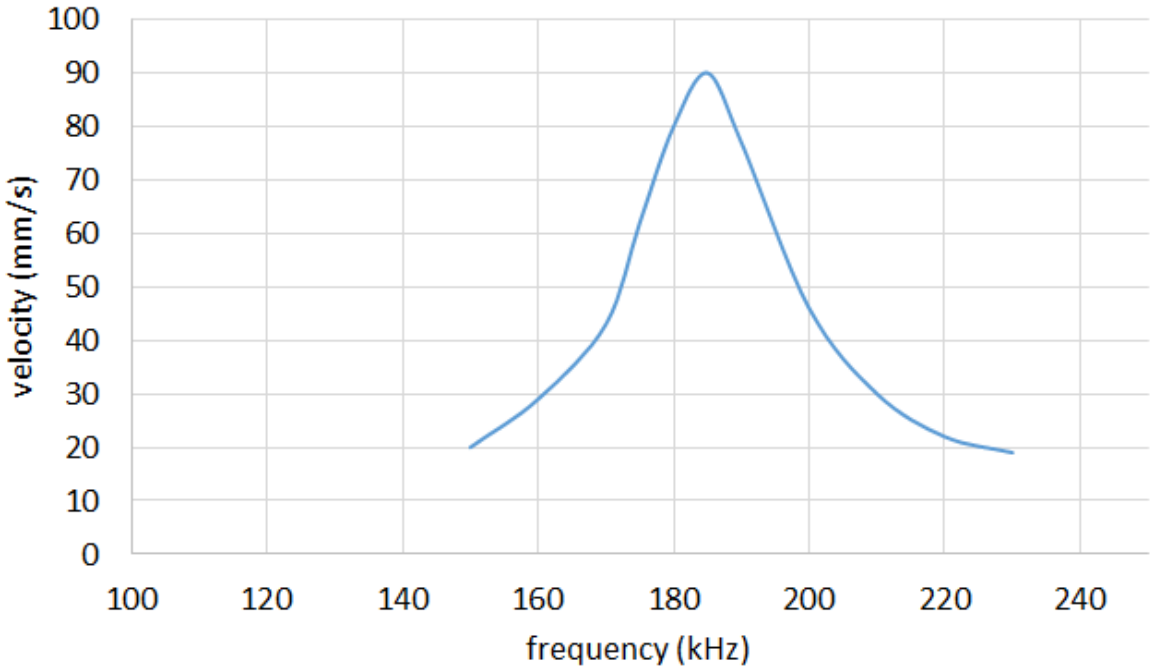

Figure 6.10: Vibrometer measurement of $160\mu m \times 45\mu m$ CMUT test structure, showing velocity vs frequency when bias voltage is $70V$.

coefficient of alumina was not provided. In fact, if the residual stress was reduced by 30% in the FEM simulation, the CMUT resonant frequency became $190kHz$, much closer to the measurement result, and the pull-in voltage was reduced to $140V$. The remaining error in the pull-in voltage can be attributed to a smaller gap height due to process tolerance and gravity, and the fringing electric field (as the bottom electrode extended beyond the width of the membrane as shown in Figure 6.4) that was not modelled in the FEM simulation.

6.5.2 Ultrasound testing

A pitch-catch experiment was performed to prove that the beams can function as ultrasonic transducers. An array of $160\mu m \times 45\mu m$ CMUTs was used to generate ultrasonic waves

	FEM	Measurement
Pull-in voltage	$170V$	$90V$
Resonant frequency at 80% pull-in	$216kHz$	$185kHz$

Table 6.4: FEM and experimental results of the $160\mu m \times 45\mu m$ CMUT.

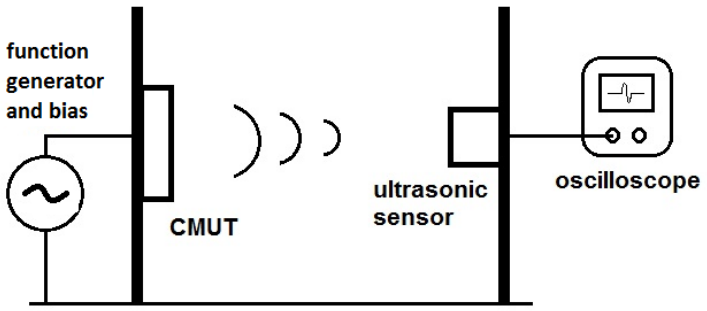

Figure 6.11: Experimental setup of pitch-catch experiment for air-coupled CMUTs.

through the air. The array contains 600 CMUTs (10 by 60) and has an area of $1.7mm$ by $2.4mm$. The pitch-catch experimental setup is illustrated in Figure 6.11. The CMUT array and an ultrasonic sensor (Knowles, SPM0404UD5) were situated on two printed circuit boards (PCBs), facing each other. The CMUT array was driven by a voltage signal and the output of the sensor was amplified by $6dB$ by a pre-amplifier (not shown here) and was displayed on an oscilloscope. With the CMUTs biased at $70V$, a tone burst consisted of 8 cycles of $180kHz$, $16V_{pp}$, sine waves was used to excite the CMUTs. The burst was provided by a BK Precision 4084 function generator.

Figure 6.12 is the pitch-catch experimental results when the ultrasonic sensor was located $3cm$ from the $160\mu m \times 45\mu m$ CMUT array. The signal was averaged 256 times to reduce the white noise. Time $t = 0$ in the plot denotes the start of the transmission. Because the two PCBs were in close proximity, electromagnetic radiation actually caused a significant signal, or crosstalk, to appear in the sensor output, as indicated by "EM radiation" in the figure. Electromagnetic radiation travels at the speed of light, so there

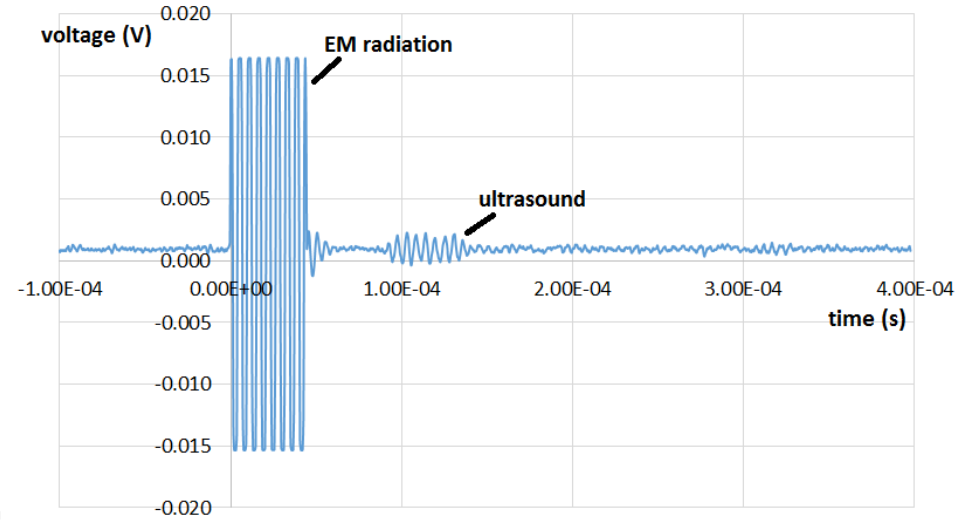

Figure 6.12: Pitch-catch experimental results for $160\mu m \times 45\mu m$ CMUTs.

is almost no delay between the start of transmission and crosstalk. On the other hand, sound only travels at approximately $340m/s$ in air, thus it takes about $88\mu s$ to reach the sensor, as illustrated by the delay of the ultrasonic signal.

The received signal has a peak-to-peak amplitude of $2mV$, or an RMS amplitude of $0.7mV$. To estimate the pressure that it represents, one needs to consider the sensitivity of the ultrasonic sensor. The Knowles sensor is specified to detect ultrasound in the range of $10kHz$ to $65kHz$, which is too low for the current experiment. As a result, the output pressure cannot be characterized. Nevertheless, the pitch-catch experiment shows that the air-coupled CMUTs are capable of generating ultrasound in air.

While the short distance ($3cm$) that separates the ultrasonic transmitter and sensor is not atypical, for example, that separation was $1cm$ in [42], it would be beneficial to transmit ultrasound further by employing a lower frequency and a larger aperture. Moreover, an ultrasonic frequency that matches the sensor frequency response will allow more accurate characterization. Therefore, a second generation of air-coupled CMUTs was designed.

6.6 Second generation devices

The main objective of the second generation devices was to improve the output acoustic power by (1) using lower ultrasound frequencies, thus reducing the attenuation in air, and (2) connecting more CMUTs in parallel, thus increasing the area, or aperture, of an element. The new CMUT array consisted of $350\mu m \times 50\mu m$ fixed-fixed beams. The modelled resonant frequency, with $0.8V_{pi}$ bias, was $77kHz$, assuming again a 30% reduction in the residual stress.

6.6.1 Characterization

The first step of the characterization process was to measure the resonant frequency of the CMUTs using a vibrometer. Again, continuous-wave sinusoid signals were used, forcing the CMUT membrane to vibrate at the frequency of the sinusoid signal. By sweeping the signal frequency and observing the membrane vibration amplitude, one can find out the resonant frequency because the vibration amplitude, as well as the maximum velocity of the membrane, is largest at resonance.

Figure 6.13 shows the vibrometer measurement results of a $350\mu m \times 50\mu m$ CMUT, with a $50V$ and a $60V$ bias, driven by a $10Vpp$ sinusoid signal. The resonant frequency was $72kHz$ for a $50V$ bias and $69.5kHz$ for a $60V$ bias (in fact, the resonant frequency varies among CMUT cells, more on that later). The FWHM bandwidths for both cases are $3kHz$, so the fractional bandwidth of the second generation devices is 4%. Due to the spring softening effect, increasing the bias voltage causes the resonant frequency to go down and the velocity at resonance to go up. At $70V$, the vibration disappeared, and that was when pull-in occurred and the CMUT collapsed. Due to an unknown reason, the second generation CMUTs would be damaged, and create a short circuit, every time they collapse. As a result, the pull-in voltage measurement cannot be repeated for the same device. Therefore, the pull-in voltage was estimated to be between $65V$ and $70V$. In order to avoid further device failure, the bias voltage for the pitch-catch experiment was chosen to be $50V$.

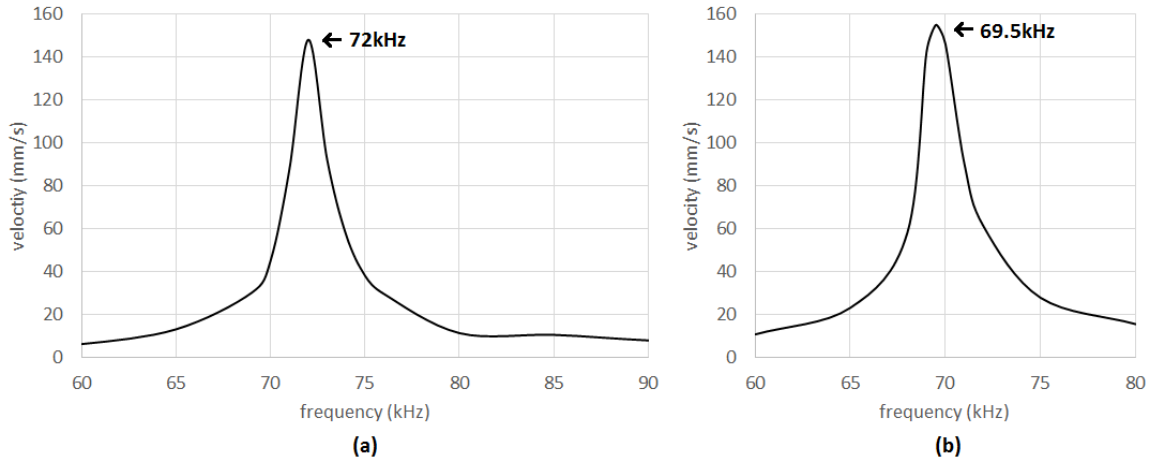

Figure 6.13: Vibrometer measurement of $350\mu m \times 50\mu m$ CMUT test structure, showing velocity vs frequency when bias voltage is (a) $50V$ and (b) $65V$.

Next, electrical characterization was performed to further confirm the resonant frequency of the CMUTs. Instead of just one CMUT cell, an array of 864 (12×72) $350\mu m \times 50\mu m$ CMUTs was connected to an Agilent E5061B ENA Series Network Analyzer as shown in Figure 6.14. The network analyzer port was connected to one of the CMUT terminal and ground, while a DC bias voltage was applied between the other CMUT terminal and ground. The network analyzer calculates impedance by sending out signals and then observing the magnitude and phase of the reflected signals. The measurement was repeated for three different bias voltages ($20V$, $40V$, and $60V$) and the magnitude of the impedance for different bias voltages are plotted in Figure 6.15.

Several observations can be made from Figure 6.15. First, the spring softening effect can again be observed. As the bias voltage increases, the resonant frequency (labelled) decreases. Secondly, the resonant frequency at $60V$ is at $74kHz$, larger than what was measured from the vibrometer experiment. Thirdly, compared to the impedance of a resonator, the peaks at the resonant frequencies do not appear to be very sharp, indicating a low quality factor. The second and third points are related, and they are caused by inconsistent resonant frequencies among the group of CMUTs. Any variations introduced

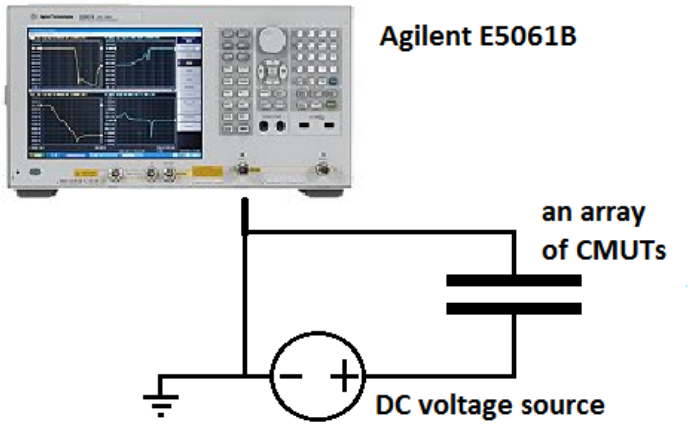

Figure 6.14: Experimental setup for electrical characterization using a network analyzer.

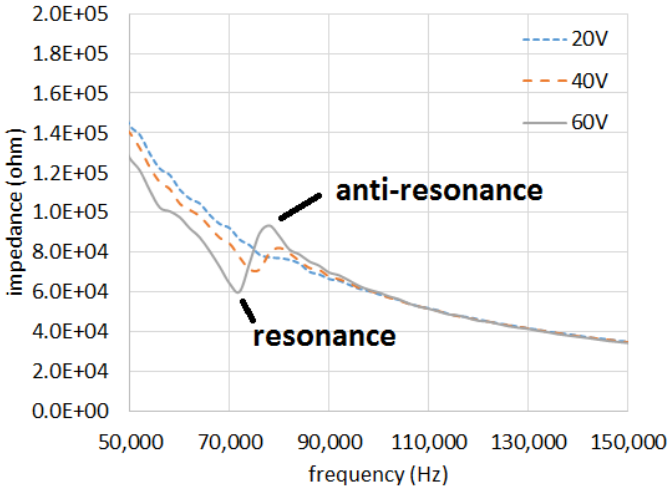

Figure 6.15: Measured impedance magnitude of a CMUT array under different bias voltages.

by the processing steps - such as residual stress, membrane thickness, and gap height - could change the resonant frequency of a CMUT. The vibrometer result is the resonant frequency of one CMUT cell, or one fixed-fixed beam, while the network analyzer result is the average resonant frequency of an array of CMUTs. This is why the two measurements do not give the same resonant frequency, and that the quality factor indicated by the network analyzer is low.

In order to find out the resonant frequency variation among CMUTs, vibrometer measurement was repeated, with the bias voltage at $50V$, for a number of cells in another $350\mu m \times 50\mu m$ CMUT array, which is shown in Figure 6.16. The results are shown in Figure 6.17. Eight random elements were picked from the 2-D array. As each element consists of 12 CMUT cells, each line in the plot represents one element. Figure 6.17 shows a significant variation (from $75kHz$ to $85kHz$) in resonant frequency among cells. Note that this array is on a different die than the array that was used for impedance measurement; as a result, the resonant frequencies of the two arrays are different. Because of the inconsistency, the output power and the sensitivity of an array are affected, as will be explained in the next section.

6.6.2 Ultrasound testing

The second generation CMUTs were used in a pitch-catch experiment. The experimental setup was mostly the same as that of the first generation devices. The excitation signal this time, however, was a tone burst with 2 cycles of $10V_{pp}$, $65kHz$ sine waves. $65kHz$ was chosen because it falls in the specified range of the Knowles ultrasonic sensor. The CMUT array (Figure 6.16), consists of 3256 (144×24) $350\mu m \times 50\mu m$ CMUTs, has an aperture size of $9mm \times 9mm$. Even though the array could be divided into 12 rows and 12 columns, all the rows were connected together, as well as all the columns, to form a single element transducer. The CMUT bias voltage was $50V$.

The ultrasonic sensor was placed $5cm$ from the CMUT array. The oscilloscope output is shown in Figure 6.18. The waveform was averaged 256 times to reduce noise. Similar to Figure 6.12, Figure 6.18 also shows crosstalk due to electromagnetic radiation at the start of transmission. Sound took $147\mu s$ to travel $5cm$ and reach the sensor. There appears to be

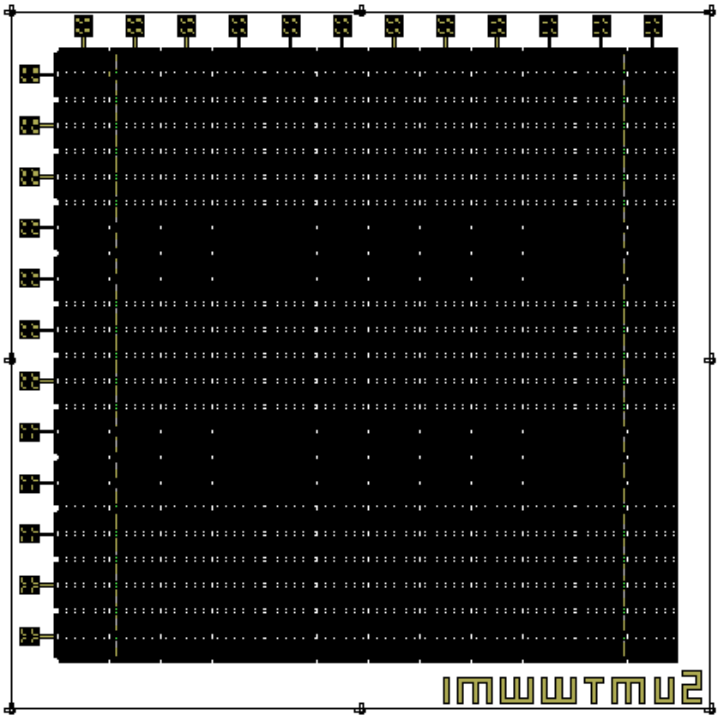

Figure 6.16: Layout of a 2-D CMUT array consisting of $350\mu m \times 50\mu m$ cells.

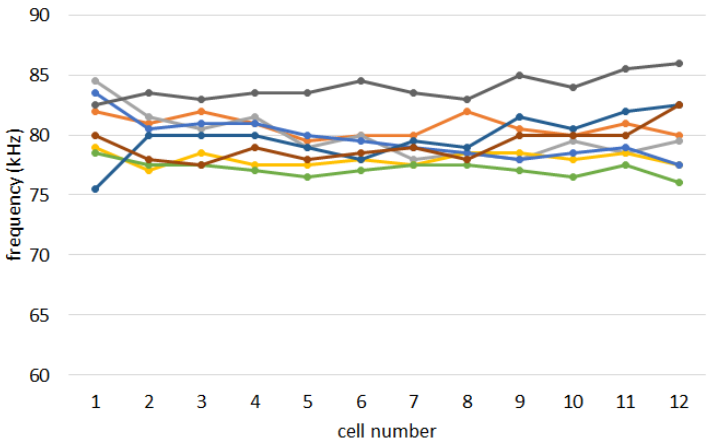

Figure 6.17: Resonant frequency of random CMUT cells in an array.

some additional pulses, between $200\mu s$ and $300\mu s$, trailing the first two cycles of received signal. The reason for that is unknown. However, they are likely due to additional vibration cycles in the transmitting CMUTs after the initial pulses.

The ultrasonic signal has maximum amplitude of $3mV_{pp}$, or $1.06mV_{rms}$. According to the Knowles sensor datasheet, the sensor has a sensitivity of $-42dBV/Pa$, or $8mV/Pa$ at $65kHz$. After taking into account the $6dB$ gain provided by the pre-amplifier, the air pressure at the sensor surface was found to be $0.066Pa$ or $70.4dBSPL$, with $20\mu Pa$ as the reference pressure. Therefore, the efficiency of the air-coupled CMUT array as a transmitter is $7dBSPL/Vpp$.

The pitch-catch experiment was repeated with the ultrasound frequency changed to $75kHz$, which is closer to the resonant frequency of the CMUTs but is out of the range for the sensor. The received signal, as shown in Figure 6.19, is comparable to the one in Figure 6.18, implying that the output pressure at $75kHz$ is larger because the sensor is less sensitive at this frequency.

Finally, a receive-only ultrasound test was performed for the second generation device. An off-the-shelf air-coupled ultrasonic transmitter (Steminc, SMATR10H60X80) was used to an ultrasonic tone burst. The tone burst consisted of 4 cycles of $100Vpp$ $60kHz$ sine wave. $60kHz$ was used because it is the resonant frequency of the ultrasonic transmitter. The CMUT output was connected to a transimpedance amplifier with a feedback resistor of $1M$ ohm. The amplifier outputs for the two cases, when the distance that sound travelled was (a)$3cm$ and (b)$5cm$, are shown in Figure 6.20. Again, the received signal started with electromagnetic radiation, followed by the ultrasonic signal a short time later. When the distance was $3cm$, the maximum signal output was about $7mVpp$; and the maximum signal output was reduced to $5mVpp$ when the distance was increased to $5cm$. The output sound pressure level of the transmitter was not provided by the manufacturer. Nevertheless, this experiment showed that the air-coupled CMUTs can indeed be used to receive ultrasound.

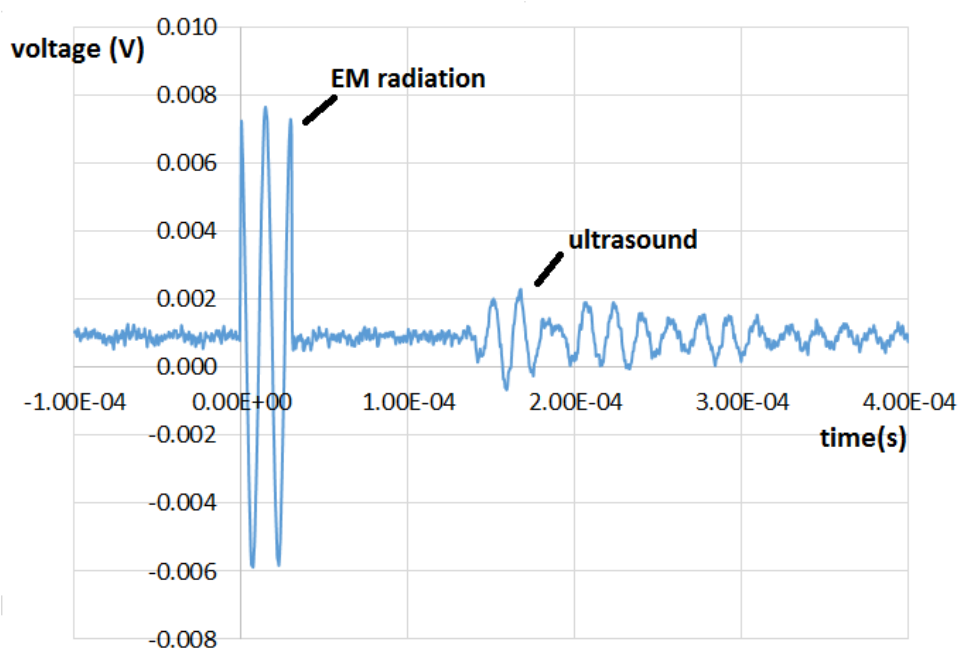

Figure 6.18: Pitch-catch experimental results for $350\mu m \times 50\mu m$ CMUTs with signal frequency $= 65kHz$.

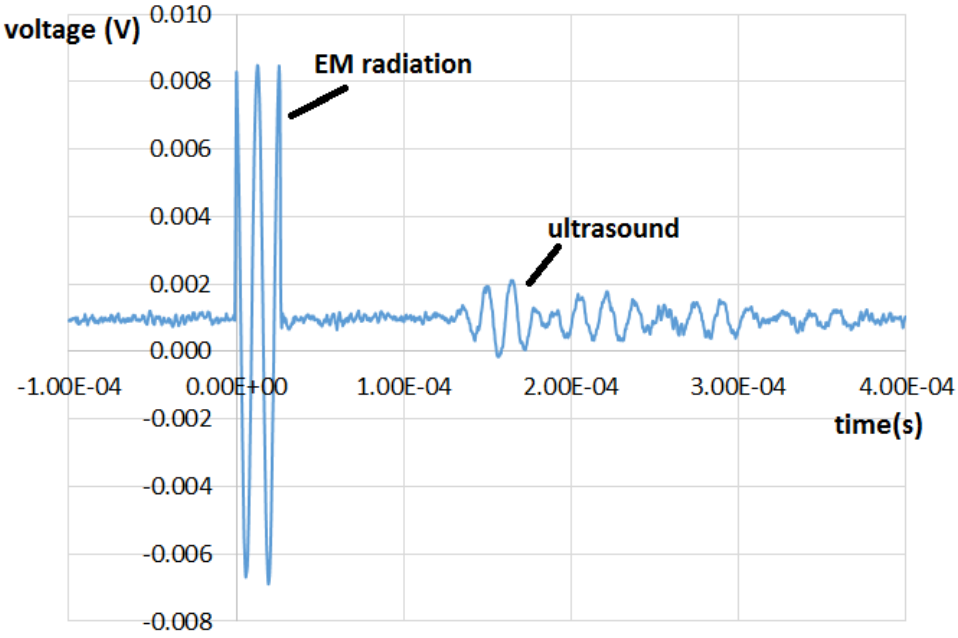

Figure 6.19: Pitch-catch experimental results for $350\mu m \times 50\mu m$ CMUTs with signal frequency $= 75kHz$.

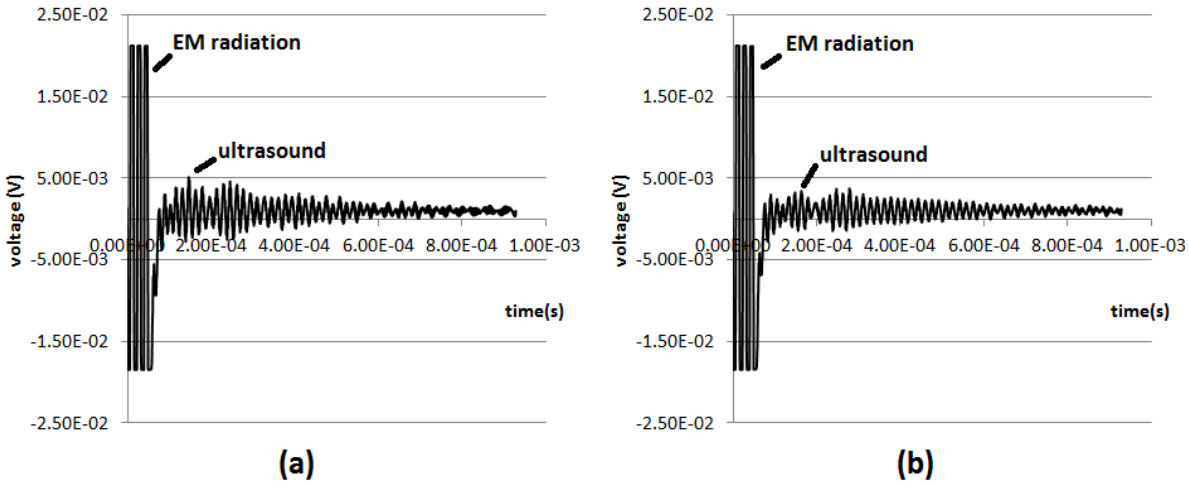

Figure 6.20: Receive-only experimental results for $350\mu m \times 50\mu m$ CMUTs with signal frequency = $60kHz$. The distance between the transmitter and the CMUT was roughly (a)$3cm$ and (b)$5cm$.

6.7 Discussion

Implementing CMUTs that can generate and detect ultrasound in air, using a standard MEMS process, has been demonstrated in this chapter. However, it is limited to an one-way operation as either an off-the-shelf ultrasonic sensor was used for the ultrasonic signal detection, or a commercial ultrasonic transmitter was used to generate ultrasound in the receive test. While it would be interesting to use the fabricated CMUTs for both transmission and reception, simple calculations can show that it is ideally possible but practically limited by the fabrication process.

The sound attenuation in air is assumed to be negligible because of the short distance ($5cm$). Further assuming that the entire CMUT array is a piston vibrating at the ultrasound frequency, the pressure generated by the piston in the far field is given in [36]:

$$P = \frac{ZAU}{2\lambda r} \tag{6.11}$$

Where Z is the acoustic impedance of the medium, which is $413Rayls$ for air in room

temperature, U is the velocity of the vibration surface, λ is the wavelength of the signal, and r is the distance between the two CMUT arrays. The equation is similar to Equation (3.15) except that a more general area variable (A) is used instead of assuming that the aperture is circular in shape. The maximum velocity of the CMUT membrane can be found from the plot in Figure 6.13(a). Even though the velocity can be increased by a larger driving voltage ($10V_{pp}$ was used for the vibrometer measurement), the peak value shown in Figure 6.13(a), $150mm/s$, is used for this example. As an aside, $150mm/s$ corresponds to a vibration amplitude of $318nm$ for a $75kHz$ signal. Using an area of $9mm \times 9mm$, the pressure generated by the CMUT array, measured at $5cm$ away, is $11.15Pa$.

Now, consider each CMUT individually, the acoustic pressure on a CMUT causes the membrane to move, by an amount determined by the effective spring constant:

$$PA_{beam} = k_{soft}x \tag{6.12}$$

where A_{beam} is the area of the beam, or $350\mu m \times 50\mu m$ in this case, x is the beam displacement, and k_{soft} is the spring constant with spring softening effect, as provided in Equation 6.7. Using the provided material properties and assuming that the residual stress is 30% smaller than the specified value, k_{soft} is found to be $46N/m$. Therefore, the membrane displacement caused by a $9mm \times 9mm$, $350\mu m \times 50\mu m$ CMUT array $5cm$ array can be found to be $4.24nm$.

The membrane displacement results in a change of capacitance between the two electrodes, which can be converted to current if the voltage between the two electrodes is held constant:

$$\begin{aligned} Q &= CV \\ I &= \frac{dC}{dt}V \end{aligned} \tag{6.13}$$

For a parallel plate capacitor, the capacitance is given by

$$C = \frac{\varepsilon A}{d} \tag{6.14}$$

where d, again, is the gap height. Assuming the static gap height is $2.5um$, which is an overestimation because of the bias voltage, the change in capacitance for a displacement of

$4.24nm$ is found to be $0.102fF$. Because the array contains 3256 CMUTs, the total change in capacitance is $0.332pF$. If the capacitance only varies with the ultrasound frequency, the capacitance and the first derivative of the capacitance with respect to time can be written as

$$\begin{aligned} C &= A_C \sin(2\pi f t + \phi) \\ \frac{dC}{dt} &= 2\pi f A_C \sin(2\pi f t + \phi) \end{aligned} \tag{6.15}$$

With that, the output current can be found to have an amplitude of $7.8\mu A$, which can be easily converted into a voltage amplitude of $0.78V$ with a transimpedance amplifier that has a gain of $100k\Omega$.

In practice, however, several of the assumptions made above are not valid. Firstly, the total area of the vibrating surface is less than the aperture size because the vibration amplitude only reaches maximum at the centre of the beam, and as the beam is fixed on both sides, the equivalent vibration surface area is likely less than $350\mu m \times 50\mu m$. Secondly, the etch holes on the top electrode can reduce the CMUT sensitivity as a receiver. This is because the membrane vibration during receive is caused by a pressure difference between the top and bottom of the membrane, and etch holes can shunt the pressure difference and reduce the vibration magnitude, thus the receive sensitivity. Thirdly, because of the variation in resonant frequencies among cells, as pointed out in the characterization section, not all the cells are vibrating with maximum velocity. As a result, output acoustic power, as well as the sensitivity in receive mode, is affected. Last but not least, squeeze film damping, which was not modelled here, reduces the membrane vibration amplitude and can negatively affect the sensitivity of the CMUTs.

Several modifications can be made to improve the CMUT efficiency if a custom process is used instead. A larger gap height and thus a larger bias voltage should be used to increase the membrane vibration amplitude and reduce the effective spring constant. A large voltage will also increase the output current for the same capacitance change. The membrane structural layer should be made thinner to improve the spring constant. Adding a layer to seal the etch holes will also be beneficial. Finally, the residual stress of the membrane layer should be better controlled so all CMUTs in the same array will have a similar resonant frequency, preferably within 1% as the membrane velocity reduced to less

than half of its maximum when the excitation frequency was off by 2%, as shown in Figure 6.13.

The exercise presented in this chapter shows that CMUT is a suitable technology for air-coupled ultrasonic transducers. Even though the fabrication process, which was designed for RF MEMS switches, was not optimized for CMUT design, we were still able to generate and detect ultrasound in air with the assistance of off-the-shelf components.

Chapter 7

Summary, Discussion, and Future Work

7.1 Summary

Ultrasonic NDT was first proposed in the early nineteenth century. Since then, different inspection techniques - for example, pulse echo and through transmission, immersion and air-coupled - has been developed, and the technology has been used in different applications such as inspection of weld joints, material characterization, and structural health monitoring. Ultrasonic is one of the more popular NDT methods because it is portable, low cost, and it does not emit harmful radiation.

And then there is CMUT, a two-decade old transducer technology that has the potential to replace piezoelectric in a lot of medical imaging applications. CMUTs also make new imaging methods such as IVUS possible because of their large bandwidths and small sizes. Despite the fact that CMUTs were originally designed for air-coupled ultrasonic NDT applications, most ongoing CMUT research is related to medical applications. This is understandable because all the advantages provided by CMUTs match well with the requirements of the more challenging medical applications. However, it does not mean that CMUTs are not suitable for ultrasonic NDT. This thesis looked into the possibility

of using CMUTs for NDT by presenting, with examples, three characteristics of CMUTs that are beneficial to NDT applications.

7.1.1 High-density arrays

Ultrasonic transducer arrays employ phased array techniques to focus and steer sound beams such that mechanical movement can be eliminated when scanning an area or a volume. In order to improve the scanning resolution of an array, one can use a higher ultrasound frequency. With a higher ultrasound frequency, the element pitch of the array needs to be increased accordingly to avoid grating lobes. However, manufacturing of piezoelectric crystal-based transducers requires manual dicing of the crystal to create an array, limiting the minimum element pitch that one can achieve. All these mean that as technologies advance and the requirement of ultrasonic NDT become more demanding, piezoelectric crystal-based transducer arrays will not be able to catch up. On the other hand, CMUTs, which are fabricated using micromachining techniques, will be able to scale with the ever-demanding element pitch requirement.

In order to demonstrate surface scanning with a 2-D CMUT array, the row-column addressed array was employed. Because the row-column addressed array requires fewer connections ($2N$ versus N^2) to and from the transducer array, it can be an attractive option for NDT. The row-column addressing scheme was used to control the array. Acoustic simulations were first performed to evaluate the row-column addressing scheme using Field-II. PSF and scanning resolution of the array were presented, and they were compared with that of a regular 2-D array. It was found that while the row-column addressing scheme suffers a little in resolution when compared with a regular array, it was the limited field of view that is of major concern. Basically, the field of view is limited to the size of the aperture.

Next, experimental results of surface scanning was presented. The CMUT row-column addressed array was successfully demonstrated to detect flaws of size down to $0.5mm$ on a piece of PMMA. The potential of using CMUT arrays for immersion based ultrasonic NDT applications was shown.

7.1.2 Integration with Microelectronics

Another advantages of CMUTs is their ease of integration with microelectronic circuits. An ASIC with transmit pulsers and receive amplifiers was designed and fabricated with the $0.8\mu m$ Teledyne DALSA high-voltage CMOS process. The receive amplifier used a basic transimpedance configuration that employed a single-stage opamp and an on-chip resistor. The amplifier had a $10k\Omega$ gain and was shown to work well with a CMUT element in a pitch-catch experiment. The transmit pulser topology was a push-pull output stage, just like a digital inverter, with replica biasing for the gate voltage of the PMOS output transistor. The pulser was able to deliver a $30V$ pulse, with a pulse width of $80ns$, to a $15pF$ load.

The pusler output current was then characterized to determine the accuracy of the LDMOS models. It was found that the N-channel LDMOS transistors were modelled accurately, but the P-channel results were masked by the variation introduced by the biasing circuit. Finally, the optimum pulse width of the pulser input was measured. It generally agreed well with the predicted value of half the period of the CMUT resonant frequency.

7.1.3 Air-coupled CMUTs

The final reason that makes CMUTs suitable for NDT is the implementation of air-coupled ultrasonic transducers. The mechanical impedance of a CMUT membrane at resonance is smaller than the acoustic impedance of air, thus CMUTs are more efficient in coupling sound to air compared to the piezoelectric counterpart. Air-coupled CMUTs were fabricated with a standard multi-user process that was designed for RF-MEMS switches. As a result, the process was by no means optimized for CMUTs design.

The first generation CMUTs have membranes of size $160\mu m \times 45\mu m$ and the second generation device is $350\mu m \times 50\mu m$. The resonant frequency of the CMUT main structure (a fixed-fixed beam) could be clearly observed from the vibrometer experiment. The resonant frequency was lower than that predicted by the analytical model, but that is likely due to the loose tolerance of the membrane residual stress. Electrical characterization us-

ing a network analyzer was done for the second generation devices to verify the measured resonant frequency. Resonant frequencies from random elements were measured and presented. It was concluded that the variation in resonant frequencies ($75kHz$ to $85kHz$) is large enough to affect the output power and sensitivity of the transducer element.

Acoustic testing of the CMUTs including pitch-catch experiments using an off-the-shelf ultrasonic sensor as the receiver and receive experiments using an off-the-shelf ultrasonic transmitter was performed. The sound from the first generation air-coupled CMUT was strong enough to travel $3cm$, and the second generation devices had a range of $5cm$. There are different reasons that prevent the air-coupled CMUTs from detecting ultrasonic waves that were generated by another CMUT element. However, the main reason appears to be the non-uniformity of resonant frequencies among CMUTs, as a slight shift of resonant frequency will cause a significant loss in vibration velocity. Nevertheless, it was demonstrated that CMUTs that generated sound in air can be fabricated using an non-optimized process, thus proving the efficiency of CMUTs for air-coupled applications.

7.2 Discussion

This thesis points out and demonstrates several attributes of CMUTs that make them attractive for NDT applications. However, the question of why CMUTs are not popular in NDT still remains. This section attempts to answer that question.

Firstly, CMUTs generate ultrasound with the vibration of thin membranes. It means that CMUTs cannot generate ultrasound in solids through direct contact. This limitation puts CMUTs in a huge disadvantage because there are many NDT applications that require direct contact coupling of ultrasound.

Secondly, while CMUTs can provide a better scan resolution because of a larger bandwidth and the realization of high density arrays, technology still has not caught up to the point that the resolution provided by the piezoelectric transducers has become inadequate. Moreover, using ultrasonic arrays for NDT requires back-end components such as array controllers and data processing software. Since the industry is already slow in adopting

2-D piezoelectric arrays [11], operators will not go out of their way to replace piezoelectric arrays with CMUT arrays if it means they have to replace the back-end systems.

Thirdly, unlike IVUS where all known advantages of CMUTs (bandwidth, size, cost) contribute to the effectiveness of CMUTs, NDT applications do not get to utilize the three benefits that were discussed in this thesis. For example, air-coupled CMUTs typically do not require high-density phased array because air-coupled applications require lower ultrasound frequencies that correspond to a larger wavelength. An application that requires high density arrays might not need ASICs or a high degree of integration. The benefits of CMUTs cannot be taken advantage of together, making them less attractive.

In summary, given all the advantages, CMUTs can be useful in certain NDT applications. However, one needs to find applications that will highlight the CMUT specialities. Some examples of those applications are air-coupled ultrasound, immersion based 2-D arrays, and structural health monitoring.

7.3 Future Work

The secondary motivation of this thesis is to continue and enhance the CMUT research in our lab. Through the three projects that are described in this thesis, a lot of groundwork has been laid. There are, however, a few things that can be done to build on this foundation.

7.3.1 Row-column addressed arrays

The row-column addressing scheme is an intriguing idea because it greatly reduces the number of interconnections and for medical imaging, the scan time. Its main limitation is the resulting field of view, which is roughly the same as the array aperture size. One way to increase the field of view is to use a larger array. However, the image quality will suffer if the aperture size is too large compared to the depth. The logical solution, then, is to use a larger array but only activate one section of the array at a time for imaging. The final image would then be a combination of all the images generated from different sections. To

make this idea work, some kind of signal and image processing needs to be done so that there is a smooth transition between different sections in the final image.

7.3.2 ASICs

The ASIC described in this thesis was not optimized for any specific CMUT design. Because the goal was to design an ASIC that can work with a variety of CMUTs, the worst case scenario for the capacitive load was assumed. Thus, the circuit draws more current and occupies more space than is necessary. Therefore, if the size of the CMUT array element was known in advance, one should be able to design a version that consumes less current and occupies less space while maintaining the circuit performance.

Another item that was not verified was the crosstalk within the ASIC. The current ASIC was designed as a test chip. Therefore, only a few amplifiers and pulsers were implemented and they were separated by a relatively large distance. But in an ASIC that is designed for integration with an CMUT array, there will be many circuit components (one for each element) and they will be tightly packed. As a result, signal may leak from one amplifier to another. Therefore, characterization should be done on the next generation ASIC for any crosstalk issue.

Characterization of the ASIC is also required, but it should only be done after the ASIC is monolithically integrated with the CMUTs. Performance parameters such as Noise Equivalent Pressure, pressure output per volts of driving signal, and insertion loss will provide important characterization metrics that can be used to benchmark the CMUT-ASIC system against past and future work.

Finally, in order to minimize the total circuit area, one should look into implementing the ASIC with a process of a smaller feature size. The current $0.8\mu m$ process was used because it was available, but changing to a $0.18\mu m$ will result in a four times reduction in device area, although the area used for signal and power supply routing might not scale with the process.

7.3.3 Air-coupled CMUTs

While it was proved that a standard process could be used to generate ultrasound in air, the output acoustic power delivered was too small for a lot of applications. Using a custom process that has the dimensions and structural parameters optimized for air-coupled CMUTs will improve the output acoustic power significantly. In addition, one should look into ways to control residual stress resulted from the fabrication. Output acoustic power is greatly reduced if CMUT cells are not resonating at the same time.

The final suggestion is not just for air-coupled CMUTs but for NDT CMUTs in general. One should actively look for NDT applications that can benefit from using CMUTs. Engage with the industry and try to solve their problems. This may be the best thing that a researcher from academia can do to give back to society.

7.4 Concluding Remarks

In this thesis, three different projects were attempted to (1) demonstrate the CMUT characteristics that are beneficial for NDT applications, and (2) enhance CMUT research in our lab in general. Overall, the projects were successful. The row-column addressing scheme was demonstrated for NDT surface scanning. At the same time, the limitations of the addressing scheme were identified, providing motivations for future research. An ASIC was developed for CMUTs. Acoustic testing with the CMUTs and the ASIC showed that the circuits were completely functional. Characterization of the pulser was done, and several key design parameters were presented, to help the design of future ASICs for both NDT and medical imaging CMUTs. Air-coupled CMUTs were designed and successfully demonstrated for ultrasound transmission. Several limitations of the current fabrication process were identified to assist any future effort in air-coupled CMUTs design. The thesis concludes with a discussion of the current state of CMUTs in NDT. While the CMUT technology may not be the best solution for a lot of NDT applications, especially given that coupling of ultrasound through direct contact is not possible, there are still some applications that can benefit from the unique characteristic of CMUTs. The key, then, is to

understand both the strength and limitations of CMUTs and only use them in applications that can utilize their advantages.

APPENDICES

Appendix A

ANSYS code for fixed-fixed beam simulation

FEM simulations were performed during the design of air-coupled CMUTs. The simulations were done in ANSYS, mainly because the entire simulation can be set up and configured using a script, thus iteration of design parameters can be done quite easily.

The following is a script example that was used to simulate a $160\mu m \times 45\mu m$ fixed-fixed beam with a bias voltage of $70V$:

```
fini
/clear, all
/title, CMUT Modelling
/nopr

! Define the dimensions
L = 160
b = 45
h = 1.25
hg = 2.5
```

```
v = 70 ! set bias voltage to 70V

/prep7
TREF,170  !set reference temperature

!Material properties of gold
mp,ex,1,79e3
mp,nuxy,1,0.44
mp,dens,1,19.3e-15
MP,ALPX,1,6e-6 !thermal expansion coefficient

et,1,186 !3-D solid element

!define geometries
block,0,L,0,h,0,b   !main beam
block,30,40,0,h,b/2-5,b/2+5   !etch holes
block,60,70,0,h,b/2-5,b/2+5
block,90,100,0,h,b/2-5,b/2+5
block,120,130,0,h,b/2-5,b/2+5
vsel,all
vsbv,1,all,,,DELETE

BFUNIF,TEMP,0 !set temperature, introduce tensile stress

!Meshing
MSHAPE,1,3D !Perform segmentation
VMESH,ALL

nummrg,all

!set boundary conditions
```

```
nsel,all
nsel,s,loc,x,0

d,all,ux,0
d,all,uy,0
d,all,uz,0

nsel,all
nsel,s,loc,x,L

d,all,ux,0
d,all,uy,0
d,all,uz,0

nsel,all
nsel,s,loc,y,0
nsel,r,loc,x,5,L-5
cm,bottom,node
emtgen,'bottom',,,'uy',-hg

!apply voltage difference to top and bottom electrodes
nsel,s,loc,y,-hg
d,all,volt,0
d,all,uy,0
cmsel,s,bottom
d,all,volt,V

alls
fini

/solu
```

```
!static analysis
antype,0
nlgeom,on
pstres,on
solve

fini

/solu
!modal analysis
ANTYPE,modal
modopt,unsym,4
eqslv,front
mxpand,4,,,yes

NLGEOM,on
pstres,on
psolve,eigunsym
fini

/SOLU
!Solve for eigen frequencies
expass,on
psolve,eigexp
fini
```

Appendix B

Field-II code for acoustic modelling of row-column addressing scheme

Field-II was used to model the acoustic performance of the row-column addressing scheme with the row-column addressed CMUT array. Below is the code for the generation of Figure 4.10. The Field-II code was modified from a version provided to the author by Albert Chen, who modified the code from online resources.

```
clear
clc
tic
f0=5.9e6; % Transducer center frequency [Hz]
fs=100e6; % Sampling frequency [Hz]
c=1430; % Speed of sound [m/s]
lambda=c/f0; % Wavelength
set_sampling(fs);% Set the sampling frequency

height=4.8/1000; % Height of element [m]
width=.13/1000; % Width of element [m]
kerf_x=.02/1000; % Distance between transducer elements [m]
```

```
kerf_y=.02/1000; % Distance between transducer elements [m]
no_ele_x=32; % Number of elements in x-direction
no_ele_y=1; % Number of elements in y-direction
focus=[0 0 20]/1000; % Initial electronic focus [m]
dRange = 60; %dynamic range

disp([strcat('lambda =', num2str(lambda*1000), 'mm')])
disp([strcat('pitch =', num2str((width+kerf_x)*1000), 'mm or ', ...
num2str((width+kerf_x)/lambda), 'wavelengths')])
numLoop = 0; %init loop counter for subplot arrangements
numLoop = numLoop + 1; %loop counter

% Section 1: Generate aperture
% Transmit
enabled=ones(no_ele_x, no_ele_y); % Find which elements to use
ThT = xdc_2d_array (no_ele_x, no_ele_y, width, height, ...
kerf_x, kerf_y, enabled, 3, 3, focus);
% Receive
enabled=ones(no_ele_y, no_ele_x); % Find which elements to use
ThR = xdc_2d_array (no_ele_y, no_ele_x, height, width, ...
kerf_x, kerf_y, enabled, 3, 3, focus);

% Set the impulse response and excitation of the emit aperture
impulse_response=sin(2*pi*f0*(0:1/fs:1/f0));
impulse_response=impulse_response.*hanning(max(size(impulse_response)))';
xdc_impulse (ThT, impulse_response);
excitation=sin(2*pi*f0*(0:1/fs:1/f0));
xdc_excitation (ThT, excitation);
% Set the impulse response for the receive aperture
xdc_impulse (ThR, impulse_response);
```

```
D=10; %represents focus depth
D_scat = 10;
focus_x = 0;
focus_y = 0;
% Create scatterer
pointScat = [0 0 D_scat]/1000;
pointAmp = 100;
% Set the focus for this direction
xdc_focus (ThT, 0, [focus_x 0 D]/1000);
xdc_focus (ThR, 0, [0 focus_y D]/1000);
% Do phased array imaging to obtain C-scan
no_lines=101; % Number of A-lines per direction
sector=10; % Size of image sector
d_x=sector/(no_lines-1); % Increment in angle for image
d_y=sector/(no_lines-1);
% Pre-allocate some storage
image_data=zeros(140,no_lines*no_lines);
x_count= -sector/2;
y_count= -sector/2;
for i = 1:no_lines % per azimuth
y_count= -sector/2;
for j = 1:no_lines % per elevation
% Move the point scatterer
pointScat = [x_count y_count D_scat]/1000;
% Calculate the received response
[v, t1]=calc_scat(ThT, ThR, pointScat, pointAmp);
% Store the result
image_data(1:max(size(v)),(i-1)*no_lines+j)=v';
times((i-1)*no_lines+j) = t1;
% Steer in another angle
y_count = y_count + d_y;
```

```
end
x_count = x_count + d_x;
disp(strcat(int2str(i), 'azimuth'));
end
disp('calc_scat done');
% Adjust the data in time
min_sample=min(times)*fs;
for i=1:no_lines
for j=1:no_lines
rf_env=abs(hilbert([zeros(round(times((i-1)*no_lines+j)*fs-min_sample),1);
image_data(:,(i-1)*no_lines+j)]));
env(1:size(rf_env,1),(i-1)*no_lines+j)=rf_env;
end
disp(strcat(int2str(i), 'envelope')); %tracker
end
disp('envelope done');
% make logarithmic compression to a dB dynamic range specified by dRange
env_db=20*log10(env/max(max(env)));
env_dR=(env_db+dRange).*(env_db>-dRange) - dRange;
% find the maximum of each line and reshape for mesh fitting
J = zeros(no_lines*no_lines,1);
for k = 1:no_lines*no_lines
J(k) = max(env_dR(:,k));
end
J = reshape(J, no_lines, no_lines);

set(0,'DefaultFigureColormap',feval('gray'));
h=figure(4);
set(h,'Position', [0, 0, 1200, 600]);
set(h,'color',[1,1,1]);
k=subplot(1,2,1);
```

```
set(k, 'Position', [0.05, 0.17, 0.4, 0.8]);
set(k, 'fontsize', 14)
[X Y] = meshgrid(-sector/2:d_x:sector/2,-sector/2:d_y:sector/2);
contour_levels = 6:6:60;
contour(X, Y, -J, contour_levels)
set(k, 'YTick', get(k,'XTick'));
set(k, 'YTickLabel', get(k,'XTickLabel'));
ylabel('Elevation (mm)')
xlabel('Azimuth (mm)')
l=text(-0.2, -6.3, '(a)', 'clipping', 'off');
set(l, 'fontsize', 14)
k=subplot(1,2,2);
set(k, 'Position', [0.55, 0.17, 0.4, 0.8]);
set(k, 'fontsize', 14)
surf(X, Y, J);
ylabel('Elevation (mm)')
xlabel('Azimuth (mm)')
zlabel('Amplitude (dB)')
l=text(-1, 0, -96, '(b)', 'clipping', 'off');
set(l, 'fontsize', 14)

% Free space for apertures
xdc_free (ThT)
xdc_free (ThR)

toc
```

Appendix C

Row-column addressed CMUT arrays fabrication

The CMUT arrays were fabricated by Dr. Andrew Logan at Cornell NanoScale Facility in Ithaca, NY. The fabrication process was explained in detail in his PhD dissertation [13]. A brief summary of the fabrication procedure is included here for completeness.

The fabrication process is illustrated in Figure C.1. It started with two silicon wafers. Silicon nitride was deposited through low-pressure chemical vapour deposition (LPCVD) to the wafer on the right, and silicon dioxide was grown on the left wafer (Figure C.1(a)). Next, polysilicon was deposited on the left wafer, and the bottom electrodes were formed after trenches were created using deep reactive ion etching (DRIE) (Figure C.1(b)). Silicon nitride was then deposited on the left wafer. After that, CMUT cavities were etched into the silicon nitride layer (Figure C.1(c)). After some polishing, the two wafers were fusion bonded, and the silicon from the top wafer was removed, exposing the silicon nitride (Figure C.1(d)). Finally, access to the bottom electrodes was created using a RIE process (Figure C.1(e)), and the top layer electrodes and contact pads were deposited (Figure C.1(f)). For the top electrodes, a layer of titanium was deposited first for adhesion purpose, it was followed by $100nm$ of aluminum.

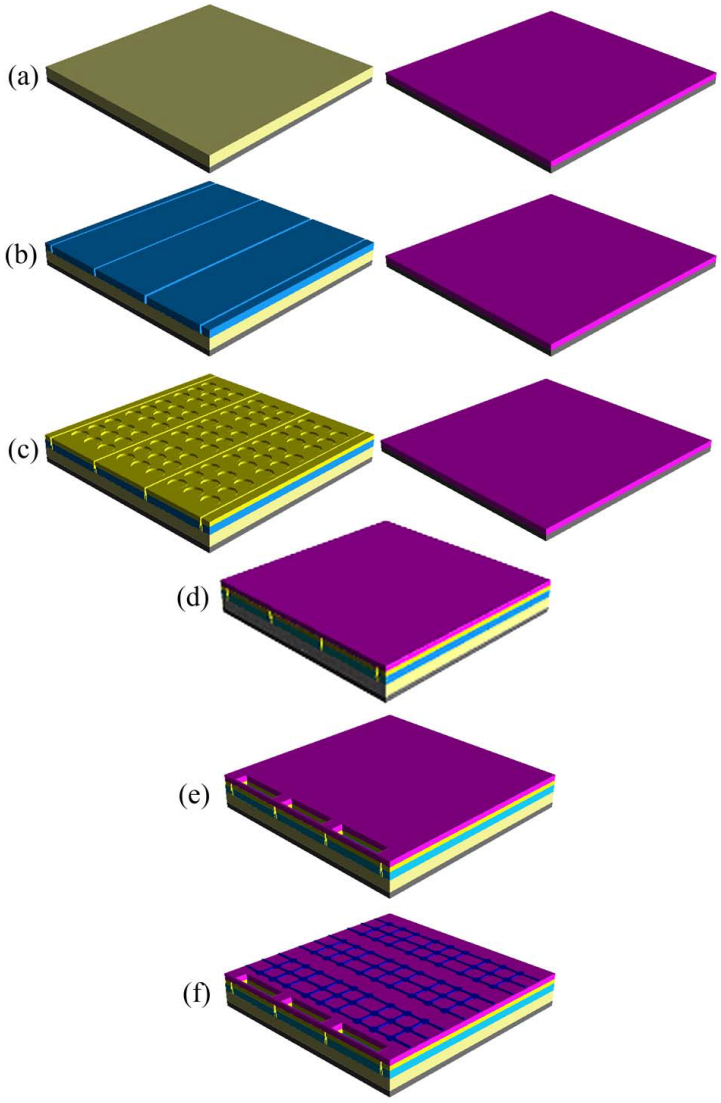

Figure C.1: Fabrication process of the row-column addressed CMUT array.©IEEE[53]

References

[1] M. I. Haller and B. T. Khuri-Yakub, "A surface micromachined electrostatic ultrasonic air transducer," *1994 IEEE Ultrasonics Symposium*, pp. 1241–1244, 1994.

[2] X. Jin, I. Ladabanm, F. L. Degertekin, S. Calmes, , and B. T. Khuri-Yakub, "Fabrication and characterization of surface micromachined capacitive ultrasonic immersion transducers," *IEEE J. Microelectromech. Syst.*, vol. 8, pp. 100–114, Mar 1999.

[3] G. G. Yaralioglu, M. H. Badi, A. S. Ergun, and B. T. Khuri-Yakub, "Improved equivalent circuit and finite element method modeling of capacitive micromachined ultrasonic transducers," *2003 IEEE Ultrasonics Symposium*, pp. 469–472, 2003.

[4] A. Lohfink, P. C. Eccardt, W. Benecke, and H. Meixner, "Derivation of a id cmut model from fem results for linear and nonlinear equivalent circuit simulation," *2003 IEEE Ultrasonics Symposium*, pp. 465–468, 2003.

[5] I. O. Wygant, X. Zhuang, D. T. Yeh, O. Oralkan, A. S. Ergun, M. Karaman, and B. T. Khuri-Yakub, "Integration of 2d cmut arrays with front-end electronics for volumetric ultrasound imaging," *IEEE Transactions on Ultrasonics, Ferroelectrics, and Frequency Control*, vol. 55, pp. 327–342, Feb. 2008.

[6] B. T. Khuri-Yakub and O. Oralkan, "Capacitive micromachined ultrasonic transducers for medical imaging and therapy," *J. Micromech. Microeng.*, p. 054040, 2011.

[7] O. Oralkan, A. S. Ergun, J. A. Johnson, M. Karaman, U. Demirci, K. Kaviani, T. H. Lee, and B. T. Khuri-Yakub, "Capacitive micromachined ultrasonic transduc-

ers: Next-generation arrays for acoustic imaging?," *IEEE Transactions on Ultrasonics, Ferroelectrics, and Frequency Control*, vol. 49, pp. 1596–1610, 2002.

[8] D. M. Mills, "Medical imaging with capacitive micromachined ultrasound transducer (cmut)," *2004 IEEE Ultrasonics Symposium*, pp. 384–390, 2004.

[9] O. Oralken, S. T. Hansen, B. Bayram, G. G. Yaralioglu, A. S. Ergun, and B. T. Khuri-Yakub, "High-frequency cmut arrays for high-resolution medical imaging," *2004 IEEE Ultrasonics Symposium*, pp. 399–402, 2004.

[10] A. Nikoozadeh, O. Oralkan, M. Gencel, J. W. Choe, D. N. Stephens, A. de la Rama, P. Chen, K. Thomenius, A. Dentinger, D. Wildes, K. Shivkumar, A. Mahajan, M. O'Donnell, D. Sahn, and B. T. Khuri-Yakub, "Forward-looking volumetric intracardiac imaging using a fully integrated cmut ring array," *2009 IEEE Ultrasonics Symposium*, pp. 511–514, 2009.

[11] B. W. Drinkwater and P. D. Wilcox, "Ultrasonic arrays for non-destructive evaluation: A review," *NDT&E International*, vol. 39, pp. 525–541, 2006.

[12] X. Cao, M. Jahazi, J. Immarigeon, and W. Wallace, "A review of laser welding techniques for magnesium alloys," *J. Mater. Process. Technol.*, vol. 171, pp. 118–204, 2006.

[13] A. Logan, *The Design, Fabrication and Characterization of Capacitive Micromachined Ultrasonic Transducers for Imaging Applications.* PhD thesis, University of Waterloo, 2010.

[14] K. Graff, "Histoical overview of ultrasonic test development," in *Non-destructive Testing Handbook, volume 7: Ultrasonic Testing* (R. E. G. A. S. Birks and P. McIntire, eds.), Columbus, OH: American Society for Non-destructive Testing, 1991.

[15] I. Ladabaum, X. C. Jin, and B. T. Khuri-Yakub, "Air coupled through transmission of aluminum and other recent results using muts," *1997 IEEE Ultrasonics Symposium*, pp. 983–986, 1997.

[16] P. T. Khuri-Yakub, "Next-gen ultrasound," *IEEE Spectrum*, May 2009.

[17] X. Jin, I. Ladabaum, and B. T. Khuri-Yakub, "The microfabrication of capacitive ultrasonic transducers," *IEEE J. Microelectromech. Syst.*, vol. 7, pp. 295–302, Sept. 1998.

[18] Y. Huang, A. S. Ergun, E. Haggstrom, M. H. Badi, and B. T. Khuri-Yakub, "Fabricating capacitive micromachined ultrasonic transducers with wafer-bonding technology," *IEEE J. Microelectromech. Syst.*, vol. 12, pp. 128–137, April 2003.

[19] G. Li and H. Hughes, "Review of viscous damping in micro-machined structures," *Proc. SPIE*, vol. 4176, pp. 30–46, 2000.

[20] A. Logan and J. T. W. Yeow, "Fabricating capacitive micromachined ultrasonic transducers with a novel silicon-nitride-based wafer bonding process," *IEEE Transactions on Ultrasonics, Ferroelectrics, and Frequency Control*, vol. 56, pp. 1074–1084, May 2009.

[21] P. Eccardt, K. Niederer, T. Scheiter, and C. Hierold, "Surface micromachined ultrasound transducers in cmos technology," *1996 IEEE Ultrasonics Symposium*, pp. 959–962, 1996.

[22] J. Knight, J. McLean, and F. L. Degertekin, "Low temperature fabrication of immersion capacitive micromachined ultrasonic transducers on silicon and dielectric substrates," *IEEE Transactions on Ultrasonics, Ferroelectrics, and Frequency Control*, vol. 51, pp. 1324–1333, Oct. 2004.

[23] A. Octavio, C. J. Martin, Y. Gomez-Ullate, O. Martinez, L. Gomez-ullate, F. M. de Espinosa, P. Gatta, and M. Dominguez, "Design and characterization of air coupled ultrasonic transducers based on mumps," *2006 IEEE Ultrasonics Symposium*, pp. 2373–2376, 2006.

[24] J. Liu, C. Oakley, and R. Shandas, "Capacitive micromachined ultrasonic transducers using commercial multi-user mumps process: Capability and limitations," *Ultrasonics*, vol. 49, pp. 765–773, 2009.

[25] S. Machida, S. Migitaka, H. Tanaka, K. Hashiba, H. Enomoto, Y. Tadaki, and T. Kobayashi, "Analysis of the charging problem in capacitive micro-machined ultrasonic transducers," *2008 IEEE Ultrasonics Symposium*, pp. 383–385, 2008.

[26] B. Bayram, M. Kupnik, G. Yaralioglu, . Oralkan, D. Lin, X. Zhuang, A. Ergun, A. Sarioglu, S. Wong, and B. T. Khuri-Yakub, "Characterization of cross-coupling in capacitive micromachined ultrasonic transducers," *2005 IEEE Ultrasonics Symposium*, pp. 601–604, 2005.

[27] Y. Huang, E. Haggstrom, X. Zhuang, A. S. Ergun, and B. T. Khuri-Yakub, "A solution to the charging problems in capacitive micromachined ultrasonic transducers," *IEEE Transactions on Ultrasonics, Ferroelectrics, and Frequency Control*, vol. 52, pp. 578–580, April 2005.

[28] O. Oralkan, B. Bayram, G. G. Yaralioglu, A. S. Ergun, M. Kupnik, D. T. Yeh, I. O. Wygant, and B. T. Khuri-Yakub, "Experimental characterization of collapse-mode cmut operation," *IEEE Transactions on Ultrasonics, Ferroelectrics, and Frequency Control*, vol. 53, pp. 1513–1523, Aug. 2006.

[29] G. Gurun, P. Hasler, and F. L. Degertekin, "A 1.5-mm diameter single-chip cmos front-end system with transmit-receive capability for cmut-on-cmos forward-looking ivus," *2011 IEEE Ultrasonics Symposium*, pp. 478–481, 2011.

[30] M. Wang, J. Chen, J.-C. Cheng, and P.-C. Li, "Design and test of a monolithic ultrasound-image-guided hifu device using annular cmut rings," *2008 IEEE Ultrasonics Symposium*, pp. 459–462, 2008.

[31] S. Wong, M. Kupnik, R. D. Watkins, K. Butts-Pauly, and B. T. Khuri-Yakub, "Capacitive micromachined ultrasonic transducers for therapeutic ultrasound applications," *IEEE Trans. Biomedical Eng.*, vol. 57, pp. 114–123, 2010.

[32] H. Jagannathan, G. G. Yaralioglu, A. S. Ergun, F. L. Degertekin, and B. T. Khuri-Yakub, "Micro-fluidic channels with integrated ultrasonic transducers," *2001 IEEE Ultrasonics Symposium*, pp. 859–862, 2001.

[33] M. Thranhardt, P.-C. Eccardt, H. Mooshofer, P. Hauptmann, and F. L. Degertekin, "A resonant cmut sensor for fluid applications," *2009 IEEE Ultrasonics Symposium*, pp. 878–883, 2009.

[34] B. T. Khuri-Yakub, K. K. Park, H. J. Lee, G. G. Yaralioglu, S. Ergun, O. Oralkan, M. Kupnik, C. F. Quate, T. Braun, H. P. Lang, M. Hegner, J.-P. Ramseyer, C. Gerber, , and J. Gimzeqski, "The capacitive micromachined ultrasonic transducer (cmut) as a chem/bio sensor," *2007 IEEE Ultrasonics Symposium*, pp. 472–475, 2007.

[35] Hitachi Medical Corp., "Development of ultrasonic transducer "mappie" with cmut technology." `http://www.hitachi-medical.co.jp/tech/medix/pdf/vol51/P31-34.pdf`, Jan. 2010.

[36] L. E. Kinsler, A. R. Frey, A. B. Coppens, and J. V. Sanders, "Fundamentals of acoustics," 2000.

[37] I. O. Wygant, M. Kupnik, and B. T. Khuri-Yakub, "Analytically calculating membrane displacement and the equivalent circuit model of a circular cmut cell," *2008 IEEE Ultrasonics Symposium*, pp. 2111–2114, 2008.

[38] H. A. C. Tilmans, "Equivalent circuit representation of electromechanical transducers-part i: lumped-parameter systems," *J. Micromech. Microeng.*, vol. 6, pp. 157–176, 1996.

[39] S. Satir, , and F. L. Degertekin, "Harmonic reduction in capacitive micromachined ultrasonic transducers by gap feedback linearization," *IEEE Transactions on Ultrasonics, Ferroelectrics, and Frequency Control*, vol. 59, pp. 50–59, Jan. 2012.

[40] M. N. Senlik, S. Olcum, H. Koymen, and A. Atalar, "Radiation impedance of an array of circular capacitive micromachined ultrasonic transducers," *IEEE Transactions on Ultrasonics, Ferroelectrics, and Frequency Control*, vol. 57, pp. 969–976, Apr. 2010.

[41] K. K. Park, M. Kupnik, H. J. Lee, B. T. Khuri-Yakub, and I. O. Wygant, "Modeling and measuring the effects of mutual impedance on multi-cell cmut configurations," *2010 IEEE Ultrasonics Symposium*, pp. 431–434, 2010.

[42] I. Ladabaum, X. C. Jin, H. T. Soh, A. Atalar, and B. T. Khuri-Yakub, "Surface micromachined capacitive ultrasonic transducers," *IEEE Transactions on Ultrasonics, Ferroelectrics, and Frequency Control*, vol. 45, pp. 678–689, May 1998.

[43] A. Sampaleanu, P. Zhang, A. Kshirsagar, W. Moussa, and R. J. Zemp, "Top orthogonal to bottom electrode (tobe) cmut arrays for 3d ultrasound imaging," *IEEE Transactions on Ultrasonics, Ferroelectrics, and Frequency Control*, vol. 61, pp. 266–276, Feb. 2014.

[44] T. L. Szabo, "Diagnostic ultrasound imaging: Inside out," 2004.

[45] G. S. Kino, "Acoustic waves: devices, imaging, and analog signal processing," 1987.

[46] A. McNab and I. Stumpt, "Monolithic phased array for the transmission of ultrasound in ndt ultrasonics," *Ultrasonics*, vol. 35, pp. 148–155, 1986.

[47] R. A. Smith, J. M. Bending, L. D. Jones, T. R. C. Jarman, and D. I. A. Lines, "Rapid ultrasonic inspection of ageing aircraft," *Insight*, vol. 45, pp. 174–177, Feb. 2003.

[48] S. C. Mondal, P. D. Wilcox, and B. W. Drinkwater, "Design of two-dimensional ultrasonic phased array transducers," *Journal of Pressure Vessel Technology*, vol. 127, pp. 363–344, 2005.

[49] S. N. Ramadas, J. C. Jackson, A. Tweedie, R. L. O'Leary, and A. Gachagan, "Conformally mapped 2d ultrasonic array structure for ndt imaging application," *2010 IEEE Ultrasonics Symposium*, pp. 33–36, 2010.

[50] C. E. Morton and G. R. Lockwood, "Theoretical assessment of a crossed electrode 2-d array for 3-d imaging," *2003 IEEE Ultrasonics Symposium*, pp. 968–971, 2003.

[51] C. H. Seo and J. T. Yen, "A 256x256 2-d array transducer with row-column addressing for 3-d rectilinear imaging," *IEEE Transactions on Ultrasonics, Ferroelectrics, and Frequency Control*, vol. 56, pp. 837–847, 2009.

[52] A. Savoia, V. Bavaro, G. Caliano, A. Caronti, R. Carotenuto, P. Gatta, C. Longo, and M. Pappalardo, "Crisscross 2d cmut array: Beamforming strategy and synthetic 3d imaging results," *2007 IEEE Ultrasonics Symposium*, pp. 1514–1517, 2007.

[53] A. Logan, L. Wong, and J. T. W. Yeow, "2-d cmut wafer bonded imaging arrays with a row-column addressing scheme," *2009 IEEE Ultrasonics Symposium*, pp. 984–987, 2009.

[54] R. K. W. Chee, A. Sampaleanu, D. Rishi, and R. J. Zemp, "Top orthogonal to bottom electrode (tobe) 2-d cmut arrays for 3-d photoacoustic imaging," *IEEE Transactions on Ultrasonics, Ferroelectrics, and Frequency Control*, vol. 61, no. 8, pp. 1393–1395, 2014.

[55] R. J. Zemp, R. Chee, A. Sampaleanu, D. Rishi, and A. Forbrich, "S-sequence bias-encoded photoacoustic imaging with top orthogonal to bottom electrode (tobe) cmut arrays," *2013 IEEE Ultrasonics Symposium*, pp. 1197–1200, 2013.

[56] A. Sampaleanu and R. J. Zemp, "Synthetic aperture 3d ultrasound imaging schemes with s-sequence bias-encoded top-orthogonal-to-bottom-electrode 2d cmut arrays," *2013 IEEE Ultrasonics Symposium*, pp. 1994–1997, 2013.

[57] R. K. W. Chee and R. J. Zemp, "Feasiblilty of modulation-encoded tobe cmuts for single-shot 3d photoacoustic imaging," *SPIE Photonics West*, 2014.

[58] T. L. Christiansen, C. Dahl-Petersen, J. A. Jensen, and E. V. Thomsen, "2-d row-column cmut arrays with an open-grid support structure," *2013 IEEE Ultrasonics Symposium*, pp. 1712–1715, 2013.

[59] A. S. Logan, L. L. P. Wong, A. I. H. Chen, and J. T. W. Yeow, "A 32x32 element row-column addressed capacitive micromachined ultrasonic transducer," *IEEE Transactions on Ultrasonics, Ferroelectrics, and Frequency Control*, vol. 58, no. 6, pp. 1266–1271, 2011.

[60] J. A. Jensen and N. B. Svendsen, "Calculation of pressure fields from arbitrarily shaped, apodized, and excited ultrasound transducers," *IEEE Transactions on Ultrasonics, Ferroelectrics, and Frequency Control*, vol. 36, no. 6, pp. 262–267, 1992.

[61] J. A. Jensen, "Field: A program for simulating ultrasound systems," *Med. Biol. Eng. Comp., 10th Nordic-Baltic Conference on Biomedical Imaging*, vol. 34, pp. 351–353, 1996.

[62] C. E. M. Demore, A. Joyce, K. Wall, and G. R. Lockwood, "Real-time volume imaging using a crossed-electrode array," *IEEE Transactions on Ultrasonics, Ferroelectrics, and Frequency Control*, vol. 56, pp. 1252–1261, Jun. 2009.

[63] R. A. Noble, R. R. Davies, D. O. King, M. M. Day, A. R. D. Jones, J. S. McIntosh, D. A. Hutchins, , and P. Saul, "Low-temperature micromachined cmuts with fully-integrated analogue front-end electronics," *2002 IEEE Ultrasonics Symposium*, pp. 1045–1050, 2002.

[64] C. Daft, S. Calmes, D. da Graca, K. Patel, P. Wagner, and I. Ladabaum, "Microfabricated ultrasonic transducers monolithically integrated with high voltage electronics," *2004 IEEE Ultrasonics Symposium*, pp. 493–496, 2004.

[65] G. Gurun, M. S. Qureshi, M. Balantekin, R. Guldiken, J. Zahorian, P. Sheng-Yu, A. Basu, M. Karaman, P. Hasler, and L. Degertekin, "Frontend cmos electronics for monolithic integration with cmut arrays: Circuit design and initial experimental results," *2008 IEEE Ultrasonics Symposium*, pp. 390–393, 2008.

[66] G. Gurun, P. Hasler, and F. L. Degertekin, "Front-end receiver electronics for high-frequency monolithic cmut-on-cmos imaging arrays," *IEEE Transactions on Ultrasonics, Ferroelectrics, and Frequency Control*, vol. 58, pp. 1658–1668, Aug. 2011.

[67] S. Peng, M. Qureshi, A. Basu, R. Guldiken, F. Degertekin, and P. Hasler, "Floating-gate based cmut sensing circuit using capacitive feedback charge amplifier," *2006 IEEE Ultrasonics Symposium*, pp. 2425–2428, 2006.

[68] K. Chen, H. Lee, A. P. Chandrakasan, and C. G. Sodini, "Ultrasonic imaging transceiver design for cmut: A three-level 30-vpp pulse-shaping pulser with improved efficiency and a noise-optimized receiver," *IEEE J. Solid-State Circuits*, vol. 48, no. 11, pp. 2734–2745, 2013.

[69] U. Guler and A. Bozkurt, "A low-noise front-end circuit for 2d cmut arrays," *2006 IEEE Ultrasonics Symposium*, pp. 689–692, 2006.

[70] A. S. Logan, L. L. P. Wong, and J. T. W. Yeow, "A 1-d capacitive micromachined ultrasonic transducer imaging array fabricated with a silicon nitride based fusion bonding process," *IEEE/ASME Transactions on Mechatronics*, vol. 16, no. 5, pp. 861–865, 2011.

[71] L. L. P. Wong, A. I. Chen, A. S. Logan, and J. T. W. Yeow, "An fpga-based ultrasound imaging system using capacitive micromachined ultrasonic transducers," *IEEE Transactions on Ultrasonics, Ferroelectrics, and Frequency Control*, vol. 59, pp. 1513–1520, July 2012.

[72] B. T. Khuri-Yakub, "Other ultrasonic techniques: air coupled transducers," in *Nondestructive Testing Handbook, volume 7: Ultrasonic Testing* (R. E. G. A. S. Birks and P. McIntire, eds.), Columbus, OH: American Society for Non-destructive Testing, 1991.

[73] P. Pallav, D. A. Hutchins, and T. H. Gan, "Air-coupled ultrasonic evaluation of food materials," *Ultrasonics*, vol. 49, pp. 244–253, 2009.

[74] W. P. Mason, "Electromechanical transducers and wave filter," 1948.

[75] F. V. Hunt, "Electroacoustics: The analysis of transduction, and its historical background," 1954.

[76] D. A. Hutchins, J. S. McIntosh, A. Neild, D. R. Billson, and R. A. Noble, "Radiated fields of capacitive micromachined ultrasonic transducers in air," *J. Acoust. Soc. Am.*, vol. 114, pp. 1435–1449, 2003.

[77] X. Wang, Y. Fan, W. Tian, H. Kwon, S. Kennerly, G. Claydon, and A. May, "Development of air-coupled ultrasound transducers for nondestructive evaluation," *MEMS 2008*, pp. 932–935, 2008.

[78] I. O. Wygant, M. Kupnik, J. C. Windsor, W. M. Wright, M. S. Wochner, G. G. Yaralioglu, M. F. Hamilton, and B. T. Khuri-Yakub, "50 khz capacitive micromachined ultrasonic transducers for generation of highly directional sound with parametric arrays," *IEEE Transactions on Ultrasonics, Ferroelectrics, and Frequency Control*, vol. 56, no. 1, pp. 193–203, 2009.

[79] M. Ho, M. Kupnik, K. K. Park, K. Eckhoff, and B. T. Khuri-Yakub, "Wide pressure range operation of air-coupled cmuts," *2012 IEEE Ultrasonics Symposium*, pp. 93–96, 2012.

[80] M. Ho, K. K. Park, K. Eckhoff, M. Kupnik, and B. T. Khuri-Yakub, "Air-coupled cmuts operating at ambient pressures ranging from 1 to 20 atm," *2013 IEEE Ultrasonics Symposium*, pp. 1412–1415, 2013.

[81] W. M. D. Wright and S. G. McSweeney, "A tethered front-plate electrode cmut for broadband air-coupled ultrasound," *2013 IEEE Ultrasonics Symposium*, pp. 1716–1719, 2013.

[82] M. Meloche and S. Chowdhury, "Design of a mems discretized hyperbolic paraboloid geometry ultrasonic sensor microarray," *IEEE Transactions on Ultrasonics, Ferroelectrics, and Frequency Control*, vol. 55, no. 6, pp. 1363–1372, 2008.

[83] Y. Maeda, M. Sugimoto, and H. Hashizume, "A robust doppler ultrasonic 3d imaging system with mems microphone array and configurable processor," *2011 IEEE Ultrasonics Symposium*, pp. 1968–1971, 2011.

[84] I. J. Oppenheim, A. Jain, and D. W. Greve, "Mems ultrasonic transducers for the testing of solids," *IEEE Transactions on Ultrasonics, Ferroelectrics, and Frequency Control*, vol. 50, pp. 305–311, Mar. 2003.

[85] J. Liu, *Design and Experimental Characterization of Broad-Bandwidth Capacitive Micromachined Ultrasonic Transducers Using Multi-user MUMPs for Vascular Flow Measurement*. PhD thesis, University of Colorado, 2009.

[86] E. M. Abdel-Rahman, M. I. Younis, and A. H. Nayfeh, "Characterization of the mechanical behavior of an electrically actuated microbeam," *J. Micromech. Microeng.*, vol. 12, pp. 759–766, 2002.

[87] S. Timoshenko, "Theory of plates and shells," 1987.

[88] K. B. Lee, "The theoretical static response of electrostatic fixed-fixed beam microactuators," *Smart materials and Structures*, vol. 17, 2008.

[89] K. B. Lee, "Principles of microelectromechanical systems," 2011.

[90] H. Kawashima, K. Sunaga, and S. Yamagata, "Torsional vibration of quartz crystal beams with static axial loads and its application to sensors," *Proc. IEEE International Freq. Control Symp.*, pp. 183–188, 1997.

[91] W. C. Young, R. J. Roark, and R. G. Budynas, "Roark's formulas for stress and strain," 2002.

[92] M. Daneshmand and R. R. Mansour, "C-type and r-type rf mems switches for redundancy switch matrix applications," *Proc. IEEE MTT-S*, pp. 144–147, 2006.

[93] M. Daneshmand and R. R. Mansour, "Redundancy rf mems multiport switches and switch matrices," *IEEE J. Microelectromech. Syst.*, vol. 16, pp. 296–303, 2007.

[94] D. W. Schindel, D. A. Hutchins, L. Zou, and M. Sayer, "The design and characterization of micromachined air-coupled capacitance transducers," *IEEE Transactions on Ultrasonics, Ferroelectrics, and Frequency Control*, pp. 42–50, 1995.

[95] R. Hickling and S. P. Marin, "The use of ultrasonics for gauging and proximity sensing in air," *J. Acoust. Soc. Am.*, vol. 79, pp. 1151–1160, Apr. 1986.

[96] T. H. Nielsen and M. H. Leipold, "Thermal expansion in air of ceramic oxides to $2200_{\circ}$c," *Journal of the American Ceramic Society*, vol. 46, no. 8, pp. 381–387, 2006.

[97] Goodfellow Cambridge Ltd., "Metals, alloys, compounds, ceramics, polymers, composites," 1993/94.